

THESIS

MEASURING AND MODELING THE ISOTOPIC COMPOSITION OF FOREST AIR

Submitted by

Theresa A. Krebs

Department of Atmospheric Science

In partial fulfillment of the requirements

for the Degree of Master of Science

Colorado State University

Fort Collins, CO

Spring, 2002

ABSTRACT

MEASURING AND MODELING THE ISOTOPIC COMPOSITION OF FOREST AIR

The oxygen isotope of atmospheric CO₂ holds great promise in the resolution of global gross photosynthetic and respiratory fluxes of carbon, while the carbon isotope in practice resolves continental and oceanic fluxes. In particular, the ecological forcing of meridional gradients in oxygen composition against rapid atmospheric mixing implies tremendous gross fluxes of the C¹⁸O¹⁶O molecule (~ 200 Gt C yr⁻¹). The mechanisms by which such large gross fluxes are communicated to larger scales are investigated using measurements and models of coupled physiological and transport mechanisms in the canopy. The correlation of strong canopy mixing with strong photosynthesis suggests that temporally averaged global inversions are sampling bulk canopy properties.

The component influences of soil, vegetation and the planetary boundary layer (PBL) on the isotopic composition of canopy air are investigated using a second-order Eulerian closure model of canopy turbulence. The statistically stationary flow field is bounded by scaled source distributions of three passive tracers: ¹²C¹⁶O¹⁶O, ¹²C¹⁸O¹⁶O, and ¹³C¹⁶O¹⁶O. Bulk fluxes are scaled in the vertical domain by assuming a Beer's law extinction of photosynthetically active radiation with cumulative leaf area depth in the canopy. The isotopic composition of the respiratory source is constrained by nighttime Keeling plots, while that of the photosynthetic source is constrained by measurements of soil, leaf and stem water. At a mixed deciduous site near Willow Creek, Wisconsin, USA, modeled profiles of ¹³C and ¹⁸O composition reproduce measured profiles very well. The stationary model provides the appearance of perfect vertical coupling, while the measurements provide evidence of decoupling between at least two canopy layers. A conceptual model consisting of two reservoirs, one a shallow layer of resistive air near the soil surface, and the other a deeper layer of well-mixed air aloft in the canopy, represent the measurements well.

Spatial and temporal comparisons of ecological contexts reveal that the ecosystem respiratory source grew heavier in ¹³C between August and October. In fall, respired carbon was older and less labile, due to a combination of higher soil temperatures and partial disaggregation of ecosystem respiration to the soil source. Differences in the ¹⁸O composition of soil, leaf and stem water challenge our assumptions about the equilibration of source water.

Theresa A. Krebs
Department of Atmospheric Science
Colorado State University
Fort Collins, CO 80523
Spring 2002

ACKNOWLEDGEMENTS

I wish to thank my adviser, Professor Scott Denning for his reservoirs of patience and for frequent enlightening conversations. Scott boosted my career at every opportunity. He tolerated my obsession with rigor at small scales even as he succeeded in winning me over to the “big picture.” Professor Joseph Berry at the Carnegie Institute of Washington fully deserves joint billing as an adviser. He opened his lab to me, engaged in individual mentoring, and made things possible that modelers only dream about. Professor James Ehleringer at the University of Utah also contributed laboratory and field resources to these efforts. All of these people placed votes of confidence, expressing their faith in my ability to overcome personal challenges.

I would like to thank Bruce Cook and the Davis Group at the Pennsylvania State University for their help in the field and the use of Willow Creek flux tower data. Dr. Neil Suits at Colorado State University contributed the isotopic model used in this study and answered my questions about isotopes. In the lab and in the field, Shenggong Li, Ben Starr, and Shannon Kincaid of the Ehleringer Group devoted their time to data collection. Jon Martin at the University of Minnesota contributed soil respiration data. John Kleist of the Denning Group processed driver data with patience, ingenuity, and good humor. Kevin Schaeffer of the Denning Group co-authored a technical note on the aerodynamics of SiB2. Dr. Miquel Ribas, Dr. Brent Helliker, and Larry Giles at the Carnegie Institute of Washington devoted their time in the field and in the lab.

I wish to thank Professor Vincent Larson at the University of Wisconsin for his objectivity and sound advice. Lastly, my parents Conrad and Katharine Krebs contributed years of patience, unwavering moral support, sound advice, and unconditional love. They came farther to meet me over three years than I did to meet them. Without their support, I would not have completed this degree.

TABLE OF CONTENTS

I.	Introduction.....	1
II.	Background.....	
2.1	The History of K-Theory in Canopies.....	
2.2	The Mechanics of Canopy Turbulence.....	
	The Plane Mixing Layer Analogy.....	
	Pathways of Energy Transformation.....	
2.3	Vegetation Effects on the Isotopic Composition of Canopy Air.....	
	Carbon Isotope Effects.....	
	Oxygen Isotope Effects.....	
2.4	Soil Effects on the Isotopic Composition of Canopy Air.....	
2.5	Recent Advances in Modeling Isotopic Exchange.....	
2.6	The Canopy and the Planetary Boundary Layer.....	
	Bottom-up and Top-down Diffusion.....	
	Tree Canopies and Diffusion.....	
III.	Methods.....	
3.1	Experimental Design.....	
3.2	The Selection of Methods and the Fulfillment of Goals.....	
3.3	Modeling Methods.....	
	The Momentum Equations.....	
	The Momentum Parameterizations.....	
	Passive and Active Scalar Transport.....	
	Numerical Methods.....	
	Local Free Convection, Similarity, and Boundary Conditions.....	
	Physiological Scaling.....	
	Isotope Calculations.....	
3.4	The Willow Creek Site.....	
3.5	Measurement Methods.....	
	Micrometeorological Measurements.....	
	Field Methods for Daytime Isotopic Air Measurements.....	
	Nighttime and Daytime Keeling Plots.....	
	Isotopic Measurements of Soil, Water, Water Vapor, and Vegetation.....	
3.6	Methods of Model-Data Synthesis.....	
IV.	The Walker Branch Case.....	
4.1	The Neutral Shadow Model.....	

4.2 The Walker Branch Case.....	
V. The Willow Creek Case.....	
5.1 Meteorological Contexts.....	
5.2 Daytime Measured Profiles.....	
5.3 Model-Data Comparisons.....	
5.4 Spatial and Temporal Ecosystem Comparisons.....	
5.5 Source Water Composition.....	
VI. Conclusion.....	

1

Introduction

The oxygen isotope of atmospheric CO₂ holds great promise in the resolution of gross photosynthetic and respiratory fluxes in a global, annual sense. Unlike the ¹³CO₂ tracer, in which the effects of photosynthesis and respiration are locally equal and opposite, the C¹⁸O¹⁶O tracer is driven asymmetrically by photosynthesis and respiration, so that the tracer is not ecologically fungible. These gross fluxes are so great that meridional gradients of ¹⁸O composition are maintained by ecological forcing against rapid atmospheric stirring. To illustrate this, consider a meridional gradient in which the northern hemisphere is lighter, or more depleted in ¹⁸O, to the tune of 1.2 parts per thousand (per mille) in a standardized ratio of ¹⁸O abundance vs. a laboratory standard (Francey and Tans, 1987). Then consider a world divided into northern and southern hemisphere boxes, each containing 175 Gt C (1 GtC = 10¹⁵ g of carbon) of CO₂. Assume an exchange time scale of one-quarter year, and a source that is 10 parts per mille lighter in the northern hemisphere than in the southern hemisphere. The turnover of C¹⁸O¹⁶O in the northern hemisphere is then $4 \times 1.2 / (10 - 1.2)$ or 55%, which is nearly 200 Gt C year⁻¹. This is roughly four times the net primary production of the planet (the amount converted to standing plant biomass). It's over twice the annual exchange of CO₂ between the atmosphere and the ocean.

A better understanding of the mechanisms behind such strong ecological forcing motivates this thesis. As physiological models become increasing mechanistic, a need

arises to test the “castle” of individual components as a system. Do the individual pieces fit together? To that end, an Eulerian model of canopy transport was developed and tested against a fully physiological model of isotopic exchange. The combination of global motivations and local intentions in both space and time, leads us ultimately to the mesoscale in search of interpretations in space and time.

The mechanism of such large gross fluxes is thought to be the exchange of CO₂ with soil and leaf water. Both soil and leaf water reflect the isotopic composition of groundwater, which is depleted in the northern hemisphere. Francey and Tans (1987) calculated a global gross flux of CO₂ that equilibrates with water of about 200-400 Gt C yr⁻¹. This thesis asks to what extent these mechanisms are reflected in canopy-scale signals of atmospheric signals, and to what extent these signals are meteorological in nature. While Francey and Tans (1987) found more sensitivity to physiology than meteorology at the global scale, this thesis invokes meteorological contexts in interpreting signals at the local scale.

Between these global motivations and local intentions, at the mesoscale, lies the context of this study in time (seasons) and space (kilometers). Each canopy isotope profile is imbedded in the large-amplitude, large-scale diurnal cycle of the PBL. The diurnal “rectifier effect” (Denning 1995, 1996) refers to the co-beating of diurnal rhythms in photosynthesis and atmospheric mixing. During the day, enhanced transport in a deep and well-mixed PBL carries air that is depleted in CO₂ by photosynthesis aloft; at night, air that is enriched in CO₂ by respiration remains stably stratified near the surface. In the annual mean, residual vertical gradients of CO₂ are amplified at temperate latitudes. Diurnal signals of CO₂ in the PBL have a rectified appearance, in that gradient reversals are not symmetric, so that daytime conditions appear relatively well-mixed. This rectified signal provides the boundary condition which canopy signals are imbedded.

This study asks whether the rectified is manifest in canopy signals as well. What are the implications for sampling ecosystems?

Dynamic ecological processes in the canopy, most notably the recycling of respired CO_2 , influence the net propagation of carbon and oxygen isotopes through physiological pathways. Canopy processes literally inform regional signals of ecosystem exchange and have the potential to bias the information contained in large-scale fluxes if vertical coupling in transport is not efficient. In fact, compelling empirical evidence in this thesis suggests that a three-component mixing model should capture the daytime evolution of a well-mixed canopy air space without any decoupling in transport.

Community interest in up-scaling CO_2 signals from leaves, to canopies, to the planetary boundary layer (PBL) motivates a reappraisal of canopy aerodynamics. Here, I present a newly developed canopy turbulence model with a rigorous set of endmember dynamical cases: a dimensionless adiabatic case; a forced convection case; a free convection case; and a pseudo-tropical case from a field study which operates differently than the regime-like familial behavior of the canopies that one knows and loves.

Next, I present the model with a simple test of tracer dynamics, using CO_2 and isotope profiles from a Wisconsin field site. As I will demonstrate, canopy-scale isotope signals are fragile. These cases demonstrate how the robust physiological scaling assumptions used in bulk land-surface models can be tested using vertically resolved models such as this. The isotope cases fundamentally validate the concept of three

component mixing: this is the idea that a well-mixed canopy efficiently samples the three “reservoirs” of soil, vegetation, and the overlying atmosphere.

The objectives of this thesis are fourfold:

- Gain insight into the Simple Biosphere Model’s treatment of canopy aerodynamics.
- Test our bulk scaling assumptions of eco-physiology in a vertically resolved model. In particular, the use of leaf area index as a vertical coordinate in the absorption of photosynthetically active radiation, and the scaling of assimilation from leaves to canopies.
- Use isotopes to test the transport model and discern the component influences of soil and vegetation on the isotopic composition of canopy air.
- Test a bulk photosynthetic fractionation model and the assumption that discrimination is constant with height. Should isotopic fluxes be vertically distributed with assimilation? Or, could the flux of $C^{18}O^{16}O$ be distributed by some weighted combination of assimilation, leaf area density, and evaporative demand? How would we invert for these distributions?

In addition to these concrete objectives, several topical issues broadly motivate the development of models such as this. One is recycling. The recycling of respired CO_2 during early morning transitions from stable to unstable conditions underneath a growing PBL is an old debate that has been revisited in light of the new importance of isotopes to the global carbon budget. Recycling is thought to make the $\delta^{13}C$ of plant matter lighter (or more depleted in ^{13}C). This is true simply because the soil respiratory source is isotopically light. This is particularly an issue in tropical ecosystems with high rates of soil respiration and statically stable atmospheric conditions in the canopy. At high latitudes, the effects of respiration are thought to be countered by Rayleigh fractionation of canopy CO_2 during photosynthetic assimilation, which enriches the $\delta^{13}C$ of plant carbon above that of the PBL (Suits, personal communication).

Another topical motivation is the length scales of mixing in the canopy. The length scales that we prescribe depend upon whether we believe the canopy to be a perturbed surface layer or a wholly different regime. The analogy of a plane mixing layer discussed

in the Background section brings to light a whole array of length scales, such as the vorticity thickness $U/(dU/dz)$ taken at the canopy height. One remaining challenge in canopy micrometeorology is to relate the length scales that arise as a consequence of the plane mixing layer analogy to the parameters used to close the equations of motion under turbulent conditions.

A third topical motivation is the presence of counter-gradient tracer transport in tree canopies. Downgradient diffusion is considered adequate for forward model simulations of land surface fluxes, while counter-gradient transport must be accounted for in inverse applications of canopy transport (Finnigan, personal communication). Better representations of canopy transport are necessary if inversions at all scales are to “drill down” into canopy processes (Gurney, personal communication). An essential motivation for this thesis is the desire to move beyond the paradigm of “resistance” and the awkward aerodynamic assumptions that become necessary to support this view of canopy transport. The possibility of testing our bulk physiological assumptions using inverse methods ties together these eclectic motivations and demonstrates the potential for vertically resolved canopy turbulence models to speak directly to our physiological assumptions. This single area of future work unifies every motivation presented here.

This thesis is divided into six parts. In the Background section, I describe the theoretical basis of both canopy transport and bulk isotopic fractionation. Each major topical motivation described above is fully developed there. Next, the formalization of the Simple Biosphere Model’s (SiB’s) aerodynamics stands as a useful contrast to the vertically resolved model. SiB’s shortcomings served as a major motivation for the development of this model and the lessons learned here will drive the future development of aerodynamics in SiB. The Methods section describes the numerical, field and laboratory methods used to create endmember cases for testing. The experimental design of physiologically coupled test is described in the Methods section. Model-data synthesis is also described in the Methods section. Endmember cases – dimensionless adiabatics, forced convection, free convection, and the pseudo-tropical field study – are described next in the chapter on The Walker Branch Case. This section contains the novel

dynamical results of this thesis. In The Willow Creek Case, the testing of a three-component mixing hypothesis is described and the isotopic signals in leaves, soil, water, and air are interpreted. Lastly, the Conclusion will present a synthesis of novel results and areas for future work that integrate the eclectic motivations of this thesis.

2

Background

2.1 The History of K-Theory in Canopies

The two-way street of phyto-atmospheric interactions comes across in microclimate models as the relationship between the mean concentration profile $C(z)$ and the source (or sink) density profile $S(z)$ for a scalar such as temperature, water vapor or CO_2 . As recently as the 1990's (Sellers et al. 1996), this bridge rested on the assumption that fluxes within a plant canopy are governed by the local diffusion equation:

$$Q_c = -\rho K_c \frac{\partial C}{\partial z} \quad (1)$$

where Q_s is the vertical flux density of the scalar and K_s is a turbulent diffusivity. For steady, horizontally uniform conditions, the scalar conservation equation reduces to

$$\frac{dQ_c}{dz} = S(z) \quad (2)$$

Combining the two equations leads to a diffusion equation

$$\frac{d}{dz} \left[\rho K_c \frac{dC}{dz} \right] + S(z) = 0 \quad (3)$$

which relates $C(z)$ to $S(z)$ given the diffusivity K_c . This system can be integrated from $S(z)$ or inverted analytically to find $C(z)$. The aerodynamic resistance is defined as

$$r_c = \int \frac{1}{K_c} dz \quad (4)$$

while the classic assumption of a constant mixing length leads to the closure assumption $K = \text{length} \times \text{velocity}$. While the resistance approach is known to be reliable above the canopy, it fails within the canopy, where counter-gradient or no-gradient fluxes are found. First-order closure is thought to be adequate in predicting forward fluxes in bulk models such as the Simple Biosphere Model (SiB2) (Finnigan, pers. comm.). However, in the inversion of concentration profiles to infer fluxes, first-order closure is hopelessly inadequate.

In 1975 and 1981, in a Ponderosa Pine forest near Canberra, A.C.T., Australia, eddy correlation measurements of sensible and latent heat fluxes and CO_2 fluxes were made above and within the forest canopy by Denmead and Bradley (1985). Within the canopy, these authors directly observed counter-gradient fluxes (Figure 1). Although Denmead and Bradley (1985) were the first to synthesize the implications of counter-gradient fluxes, earlier work revealed negative mean velocity gradients in the trunk space, where there should be a downward flux of momentum (Allen, 1968; Oliver, 1971; Jarvis et al., 1976; Legg and Long, 1975) or a local maximum in humidity at midday which implied a negative diffusivity (Droppo and Hamilton, 1973; Jarvis et al., 1976). The presence of gradient reversals alone should not imply counter-gradient flux: we still must distinguish between gradient sign reversals caused by counter-gradient fluxes and those caused by local sources. Direct measurements by Droppo and Hamilton (1973) began to address the question. For the entire canopy, these authors took the energy balance

$$R_n = H + \lambda E + G + J + \varepsilon A \quad (5)$$

where R_n is the net radiation, G is the change in ground heat storage, and εA represents the energy fixed by photosynthesis (ε is $\sim 1.15 \times 10^7$ J/kg). The storage term J includes changes in mean air temperature and humidity and in the heat stored in vegetation. While

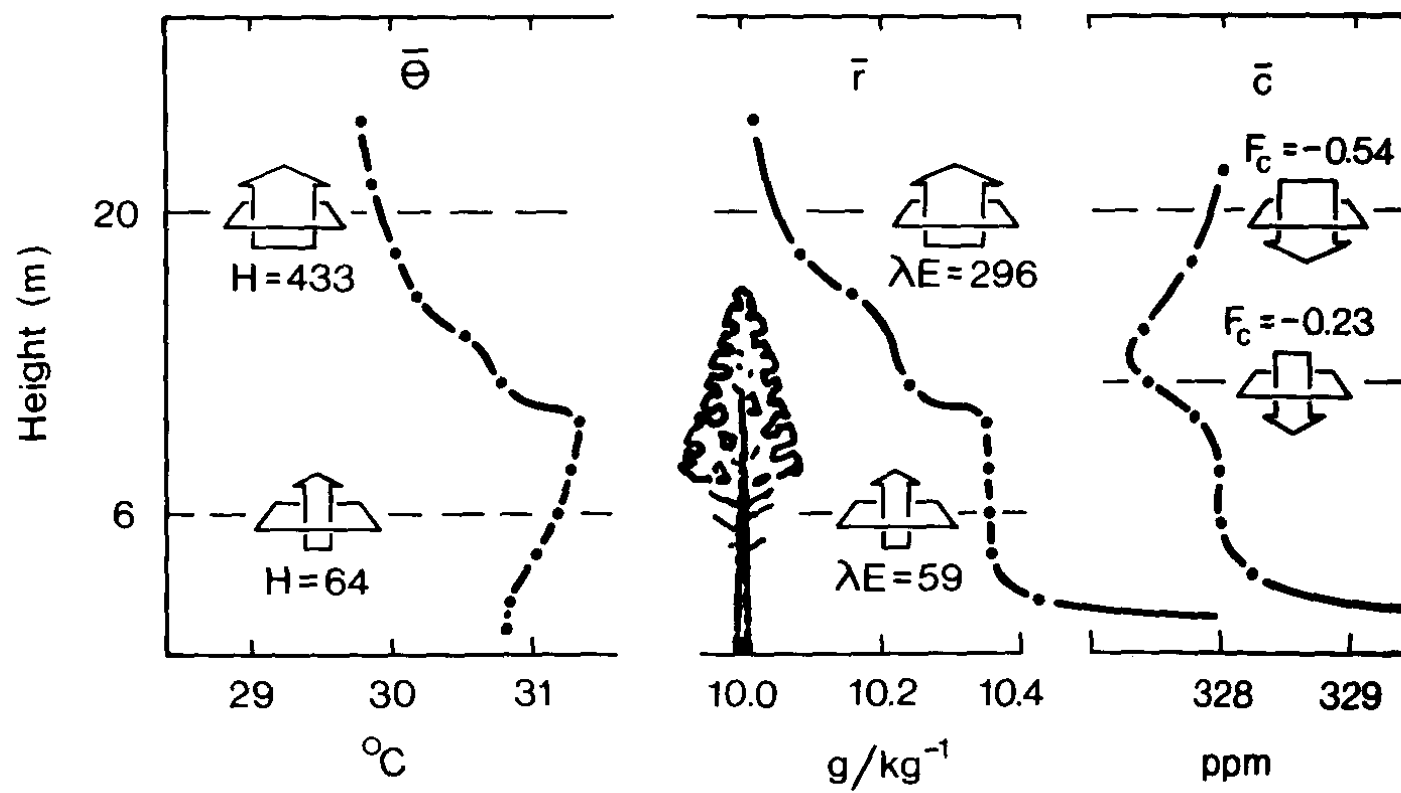


Figure 1. Observed gradients and fluxes of sensible heat, latent heat, and CO₂. From Denmead and Bradley (1985).

the available energy (the sum of latent and sensible heat fluxes) was positive everywhere in the canopy, gradients of mean temperature and humidity reversed sign.

In Figure 2, our present model is used to compare modeled fluxes of CO_2 with fluxes inferred from simple downgradient diffusion using modeled CO_2 concentration profiles. The simulation includes both a soil respiratory source and a photosynthetic sink, and the dynamics of the second-order closure model are neutral and statistically stationary. The effective eddy diffusivity for momentum was calculated from modeled Reynolds stress and mean velocity, and the scalar diffusivity K_c was $1.35 K_m$ (Stull, 1988). In the lower canopy, the inferred flux is an order of magnitude greater than the modeled flux. The eddy diffusivity calculated from modeled CO_2 flux and concentration reverses sign in above canopy crown. Surprisingly, the modeled CO_2 gradients in the presence of this reversal are quite small.

The history of K-theory was traced by Raupach (1988). One reason for K-theory's fall from favor was ambiguity in measured profiles of momentum diffusivity. In real canopies, vertical structure in the profile of the momentum sink *should* lead to a unique relationship between mean velocity and shear stress. A recent flux-gradient modeling exercise by Wilson, Finnegan and Raupach (1998) noted that "Profiles of U , τ resulting from imposition of the 'true' profile $c_d(z)a(z)h_c$ are superior to those using the constant, bulk drag coefficient C_d ; and of course, since both derive from observations of U , τ our modeled profiles of U and τ are not independent. With the height-dependent $c_d(z)a(z)h_c$, if modeled U is 'correct' then so must be modeled τ ." Thus, the profile of modeled $U(z)$ provides unique information regarding the profiles of eddy diffusivity K and the Reynolds stress τ .

In contrast, classical treatments of the surface layer with log-linear profiles of mean velocity are insensitive to the vertical profile of K . The insensitivity of $U(z)$ to $K(z)$ is implicit in the differential equations, as long as the governing mixing length is assumed to be constant with height. Looking for a unique eddy diffusivity in the canopy, workers in the '70's found they could not reproduce quasi-empirical forms of K .

Another hint came from calculations of the Lagrangian length scale. As will be shown below, the length scale of vertical motions L_w is of order h , the height of the canopy. This is significantly larger than the scale of variations in dC/dz , suggesting that vertical transfer is essentially non-local. Raupach (1988) outlined a Lagrangian argument for the implications to counter-gradient flux. The Lagrangian argument went like this: for vertical dispersion in a steady horizontal wind, $\langle w'c' \rangle$ over dC/dz increases with distance downwind from the source, for distances less than L_w/i_w , where i_w is the vertical turbulence intensity. In the presence of a source that is distributed in time or space, there is no unique value of eddy diffusivity. This “illogical conception” (Taylor, 1959) explains the ambiguity of measured K in the canopy, where the scaling of L_w/i_w is of order h .

Today, many workers emphasize canopy-scale coherent motions as a mechanism of counter-gradient flux. Raupach (1988) pointed out that in the absence of coherent motions, Lagrangian arguments alone can account for counter-gradient flux. Here Raupach considered statistically stationary, homogeneous turbulence in one dimension, in which the temporal and spatial origins of transport are arbitrary. This discussion closely follows Raupach’s arguments. For an emitted scalar such as water vapor, the source distribution is bimodal, with one maximum emittance near the soil surface and another in the tree crown. The observed scalar field is a superposition of plumes from individual leaf sources, each of which experiences near-field and far-field behavior.

In any concentration distribution that is dispersing through diffusion, the diffusivity is statistically known:

$$K = \frac{1}{2} \frac{d\sigma^2}{dt} \quad (6)$$

This can be found by integrating the diffusion equation $\frac{\partial C}{\partial t} = K \frac{\partial^2 C}{\partial z^2}$ over the second moment of z and integrating by parts. The mean square vertical displacement about the center of mass of particles in a single cloud is

$$\sigma_z^2 = \frac{1}{M} \int_{-\infty}^{\infty} (z - \bar{Z})^2 c(z, t) dz \quad (7)$$

where M is the total mass of the cloud, Z is its vertical center of mass, and $c(z, t)$ is the tracer concentration field. In the homogeneous case, the Eulerian variance above is equal to Lagrangian variance Z^2 . Then Taylor's (1921) theorem relates the ensemble averaged depth of the cloud to the velocity field. The ensemble mean square particle displacement is

$$\langle \sigma_z^2 \rangle = \langle Z^2 \rangle = \int_0^t \int_0^t \langle W(\tau_1) W(\tau_2) \rangle d\tau_1 d\tau_2 \quad (8)$$

Since the turbulence is stationary, $\langle W(\tau_1) W(\tau_2) \rangle$ is a function only of the difference between τ_1 and τ_2 . Raupach defined a Lagrangian autocorrelation function

$$R_z(\tau_2 - \tau_1) = \langle W(\tau_1) W(\tau_2) \rangle / \langle W^2 \rangle \quad (9)$$

where $\langle W^2 \rangle = \langle W(0) W(0) \rangle$. Substituting Equation 9 into the expression for cloud depth yields

$$\langle Z^2(t) \rangle = \langle W^2 \rangle \int_0^t \int_0^t R_z(\tau_2 - \tau_1) d\tau_2 d\tau_1 \quad (10)$$

Substituting the variables in the above equation yields

$$\begin{aligned} s &= \tau_2 - \tau_1 \\ \tau &= (\tau_1 + \tau_2) / 2 \end{aligned} \quad (11)$$

$$\langle Z^2(t) \rangle = 2\langle W^2 \rangle \int_0^t (t-s) R_z(s) ds$$

Two cases emerge. For very short times, a particle's initial velocity $W(t_0)$ is unchanged, turbulence is persistent and motion is approximately linear. Then R_z is nearly unity and

$$\langle Z^2 \rangle = \langle W^2 \rangle t^2 \quad (12)$$

For very long times, motion is diffusive and R_z approaches zero. If one assumes that the integrals $\int_0^t R_z(s) ds$ and $\int_0^t s R_z(s) ds$ are bounded as t becomes large, this limit yields

$$\langle Z^2 \rangle = 2\langle W^2 \rangle T_z t + \text{const.} \quad (13)$$

where $T_z = \int_0^\infty R_z(s) ds$ is the time in which a fluid particle forgets its initial velocity and is called the Lagrangian time scale. A good estimate of T_L in the canopy is (Raupach et al., 1996):

$$T_L \approx \frac{L_w}{\sigma_w} \approx \frac{U(h)}{2\pi U_c} \frac{m L_s}{\sigma_w} \approx 0.71 \frac{L_s}{\sigma_w} \quad (14)$$

where L_s is the shear length scale $U(h)/U'(h)$, U_c is the convective velocity, $m=8.1$ and $U_c/U_h=1.8$.

In the near field, when $t < T_L$, each scalar plume emitted from a leaf is concentrated and localized. The fact that local concentrations are most influenced by local sources suggests that the near-field regime dominates scalar dispersion in the crown. The more localized the crown source $S(z)$, the sharper the local maximum in C and the gradients dC/dz . A bimodal scalar source with some emittance at the soil surface results in a positive vertical flux existing throughout the depth of the canopy (see Equation 2). Due to the dominance of near-field effects, the locally imposed scalar

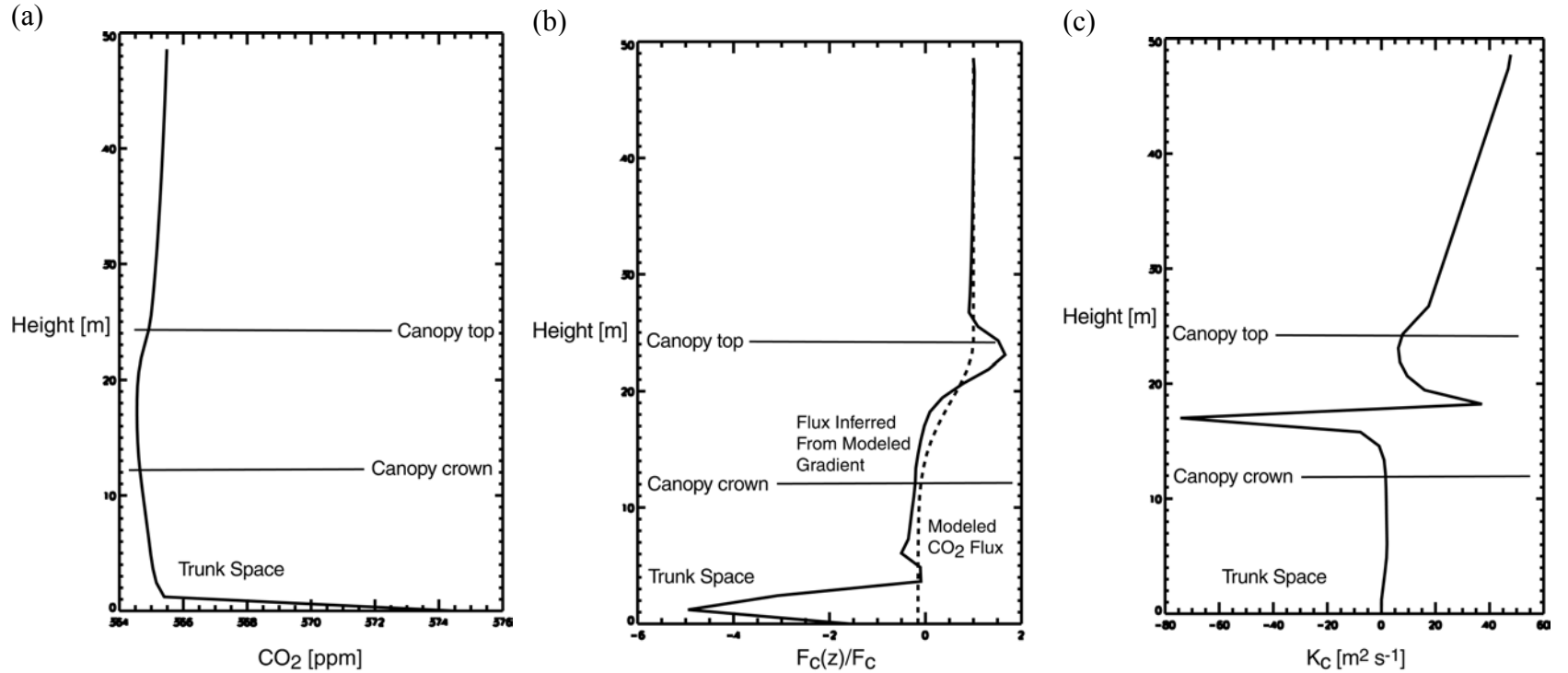


Figure 2. (a) Concentration of CO₂ with a soil respiratory source and a photosynthetic sink; (b) Normalized, modeled fluxes of CO₂ and those inferred from concentration gradients; (c) Scalar eddy diffusivity calculated from scalar concentration and flux.

gradient near the crown is truly a “local counter-flux gradient.” Raupach integrated a statistically stationary, homogeneous flow using a simple Lagrangian model and found regions of negative diffusivity in the crown region associated with strongly peaked source density distributions in the canopy crown. A similar exercise is shown in Figure 2 using our own model, in which some coherency exists in the form of a counter-gradient momentum flux.

There are two possible stories here. Whether one emphasizes a “counter-gradient flux” or a “counter-flux gradient” might depend on one’s Eulerian or Lagrangian outlook and one’s interest in near-field effects or coherent motions. Both are extremely important to vertical fluxes. They motivate the use of higher-order closure to further understand the coupling of physiology and transport. A brief discussion of coherent turbulence is provided at the end of the next section.

How does one distinguish between gradient sign reversals caused by non-local fluxes and those caused by local sources? A simple Large Eddy Simulation (LES) experiment in which the canopy as a CO₂ sink is turned “off” could potentially answer that question. By using a homogeneous turbulence field, Raupach (1988) isolated the passive effect of the local near-field on the nearby gradient.

2.2 The Mechanics of Canopy Turbulence

The Plane Mixing Layer Analogy

An assembly of single-point turbulence statistics across a range of canopies is shown in Figure 3 from Raupach et al. (1996). The quantities in Figure 3 are the mean velocity $U(z)$, the Reynolds shear stress $\langle u'w' \rangle$, the velocity variances σ_u and σ_w , the correlation coefficient $r_{uw} = \langle u'w' \rangle / \sigma_u \sigma_w$, the skewness of the vertical and horizontal velocities ($Sk_u = u'^3 / \sigma_u^3$), the single-point length scales L_u and L_w , and the leaf-area density $A(z)$. From the structure of the data, it is clear that the dominant length scale is h and the dominant velocity scale is u^* for turbulence in the canopy.

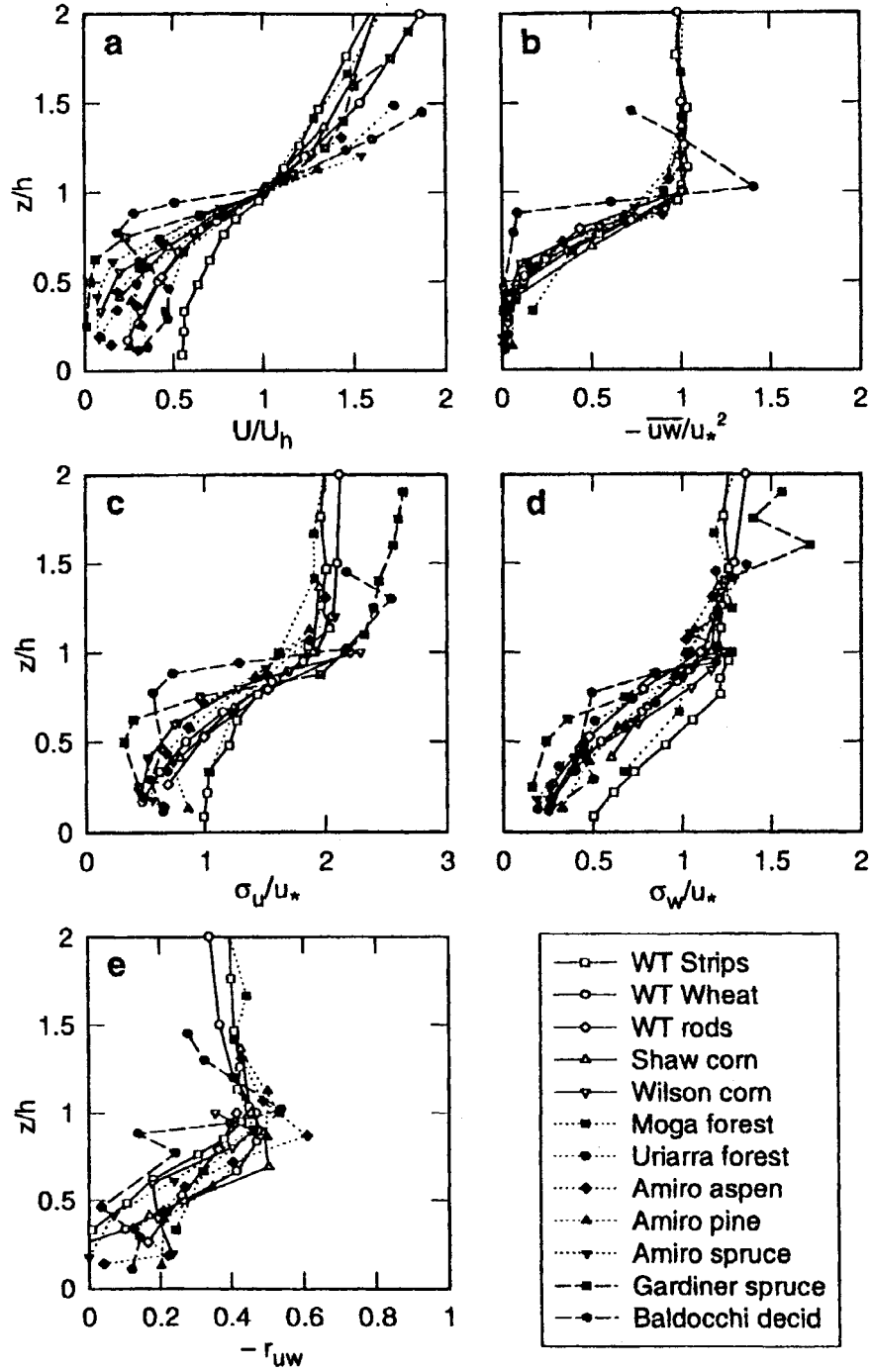


Figure 3 (a-e). Dimensionless profiles of turbulent statistics for a family of canopies: (a) U/U_h ; (b) $-\overline{uw}/u_*^2$; (c) σ_u/u_* ; (d) σ_w/u_* ; (e) $-r_{uw} = -\overline{uw}/(\sigma_u \sigma_w)$. From Raupach et al. (1996).

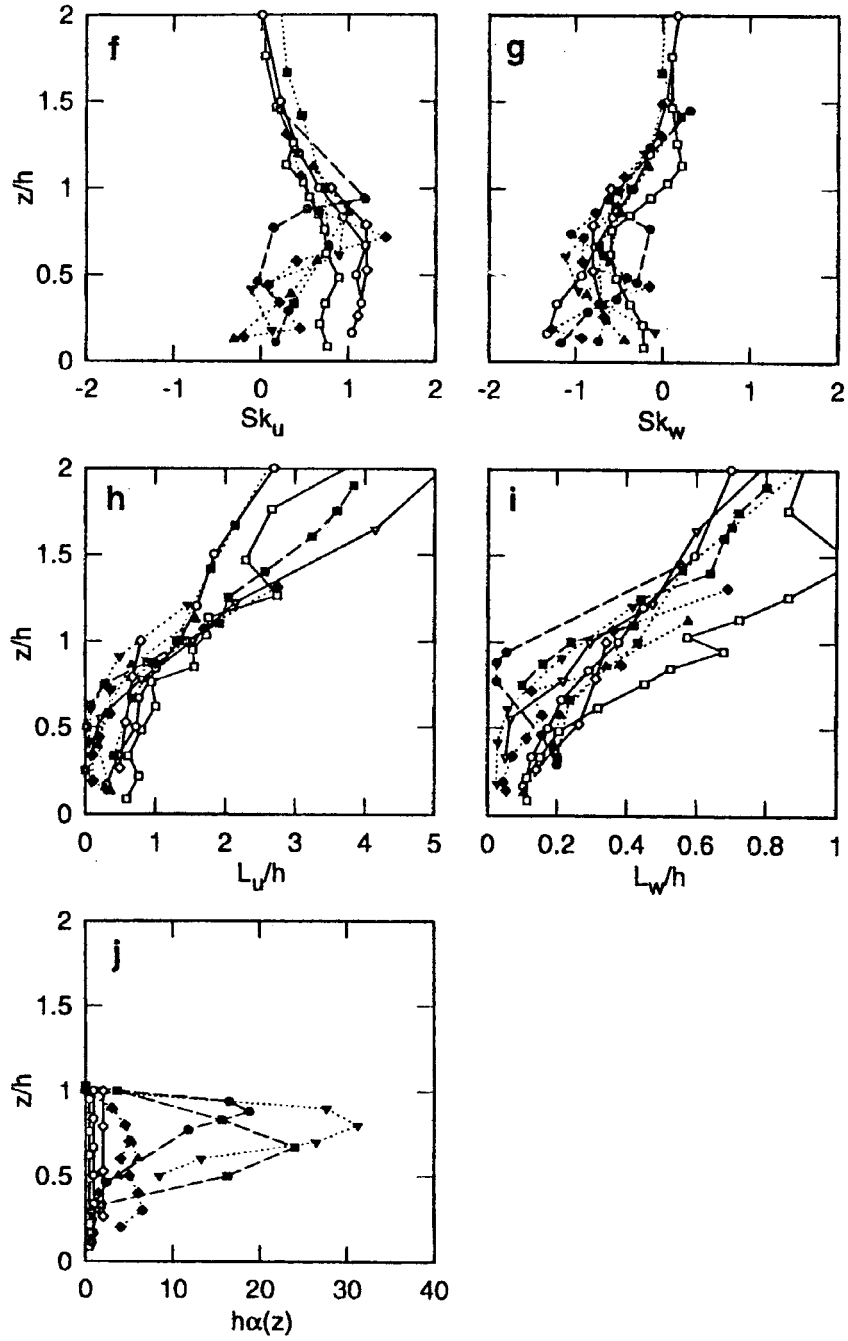


Figure 3 (f-j). Canopy statistics continued: (f) Sk_u ; (g) Sk_w ; (h) L_u ; (i) L_w ; and (j) $hA(z)$, where $A(z)$ is the leaf-area density and L_u and L_w are defined in Equation (15). From Raupach et al. (1996).

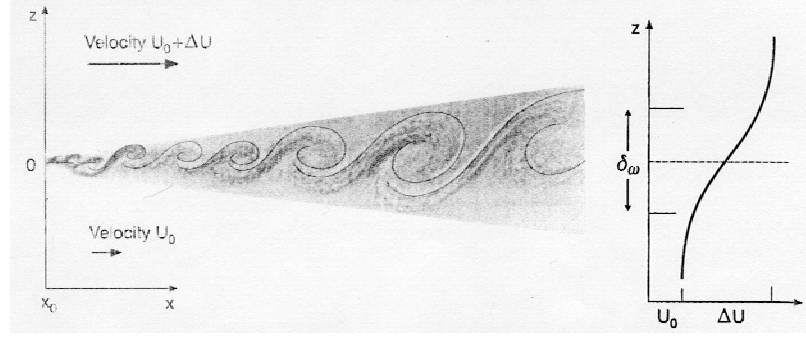
Within the canopy, there is a common vertical heterogeneity in which all statistics increase with height. Near the canopy top, where the shear is greatest, there is a strong inflection in U/U_h . This inflection triggers Kelvin-Helmholtz instability and longitudinal roll vortices. These instability processes determine the structure of coherent eddies at the canopy top. Well above the canopy, near $z=2h$, the flow takes on the familiar properties of a surface layer. The mean velocity becomes log-linear with height, and the ratios among Reynolds stress components σ_u/u^* and σ_w/u^* approach constant limits of 2.5 and 1.25 as in a constant stress layer. This gives an r_{uw} of -0.32 above the canopy, in contrast to an r_{uw} of about -0.5 near the canopy top. One can infer that canopy turbulence is somehow more coherent or more efficient at momentum transfer than turbulence in the atmospheric surface layer (Raupach et al., 1996). While skewness is small in the inertial sublayer above the canopy, the association of large positive Sk_u and negative Sk_w implies that the strongest events are strong downward motions of quickly moving air.

The intensity of turbulence in the canopy (typically $\sigma_u/U \geq 1$) makes single-point statistics less credible: L_u and L_w are almost certainly too small. The profiles in Figure 3 merely provide a qualitative picture of the nature of canopy turbulence. The single-point length scales are calculated as follows:

$$\begin{aligned} L_u &= \frac{U}{\sigma_u^2} \int_0^\infty \langle u(s)u(s+t) \rangle dt \\ L_w &= \frac{U}{\sigma_w^2} \int_0^\infty \langle w(s)w(s+t) \rangle dt \end{aligned} \tag{15}$$

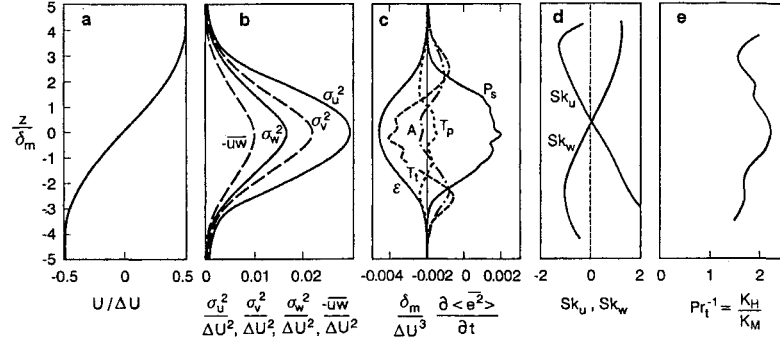
In practice, U is an underestimate of the convection velocity U_c . The proper two-point length scales L_u and L_w are about h and $h/3$, respectively, suggesting that the dominant eddies are of the scale of the canopy.

Raupach et al. (1996) presented a compelling analogy between canopy turbulence and a plane mixing-layer at the boundary between layers of air moving at different velocities. Figure 4 from Raupach et al. (1996) shows observations of a laboratory



(a)

(b)



(c)

Figure 4. Laboratory observations of a planar mixing layer. (a) Two co-flowing streams separated by a plate are allowed to mix; (b) An inflection in the mean velocity field is the source of shear instability in the growing mixing layer, which has vorticity thickness $\delta_\omega = \Delta U / (\partial U / \partial z)_{\max}$; (c) Measured statistics normalized by the momentum thickness δ_m , which is typically about $\delta_\omega / 4.5$. The quantity $\langle e^2 \rangle$ is twice the turbulent kinetic energy and Pr_t^{-1} , the inverse Prandtl number, is the ratio of diffusivities of heat and momentum. From Raupach et al. (1996).

Property	Surface Layer	Mixing Layer	Canopy ($z = h$)
$U(z)$ inflection	No	Yes	Yes
σ_u/u_*	2.5	1.7	1.8
σ_w/u_*	1.25	1.3	1.1
$r_{uw} = \overline{uw} / (\sigma_u \sigma_w)$	-0.32	-0.44	-0.5
$Pr_t^{-1} = K_H/K_M$	1.1	2	2
$ Sk_u , Sk_w $	Small	$O(1)$	$O(1)$
u, w	$\propto z - d$	$\propto \delta_w$	$\propto h - d$
TKE budget	Small T: $0 \sim P - \varepsilon$	Large T: $0 = P + T - \varepsilon$	Large T: $0 = P + T - \varepsilon$

Table 1. Comparison of the properties of surface layers, plane mixing layers, and canopy layers. From Raupach et al. (1996).

mixing-layer in which two co-flowing streams initially separated by a plate are allowed to mix. There is a strong inflection in U like that at the canopy top. The shear stress and variances increase with height to the centerline. The TKE budget reveals that turbulent transport T_t is moving energy from the region of greatest shear production to regions of weaker production. The TKE budget is far from the local equilibrium of the surface layer, in which shear production is balanced by dissipation ($P_s \approx \epsilon$). The anti-symmetric peaks in Sk_u and Sk_w suggest that sweeps dominate momentum transfer below the interface while ejections dominate above. The inverse Prandtl number Pr^{-1} (the ratio of the eddy diffusivities of heat and momentum K_H/K_M) is around 2, which is typical of free shear flows such as wakes and jets.

Canopy quantities are contrasted with those of a mixing layer in Table 1 from Raupach et al. (1996). Both canopies and mixing layers have an inflection in U , a Prandtl number of $1/2$, large velocity skewness, and significant transport of TKE. The transfer of momentum in the canopy is still more efficient than that of a mixing layer (r_{uw} of -0.5 and -0.44 , respectively) and provides evidence of the “short circuit” between the band of coherent shear production and the band of small-scale wake turbulence (see the section below). The difference in σ_u/u_* and σ_w/u_* between the canopy and the mixing layer may be due to the orientation of canopy elements, which redistribute the anisotropy of turbulent velocities, making w' smaller and u' larger. The controlling length scale of the mixing layer is the vorticity thickness $\delta_\omega = \Delta U / (\partial U / \partial z)_{\max}$, where ΔU is the difference between the two free-stream velocities.

Pathways of Energy Transformation

The pathways of energy transformation in the surface layer are altered by the presence of the canopy as shown in Figure 5 after Wilson (1988). Drag forces create a direct pathway between the mean flow and the “inactive” wake turbulence. They also extract energy from the “active” turbulence, thereby acting in addition to the normal energy cascade process. Compelling empirical evidence for this “spectral shortcut” appears in the spectra and co-spectra of eddy covariance measurements of temperature,

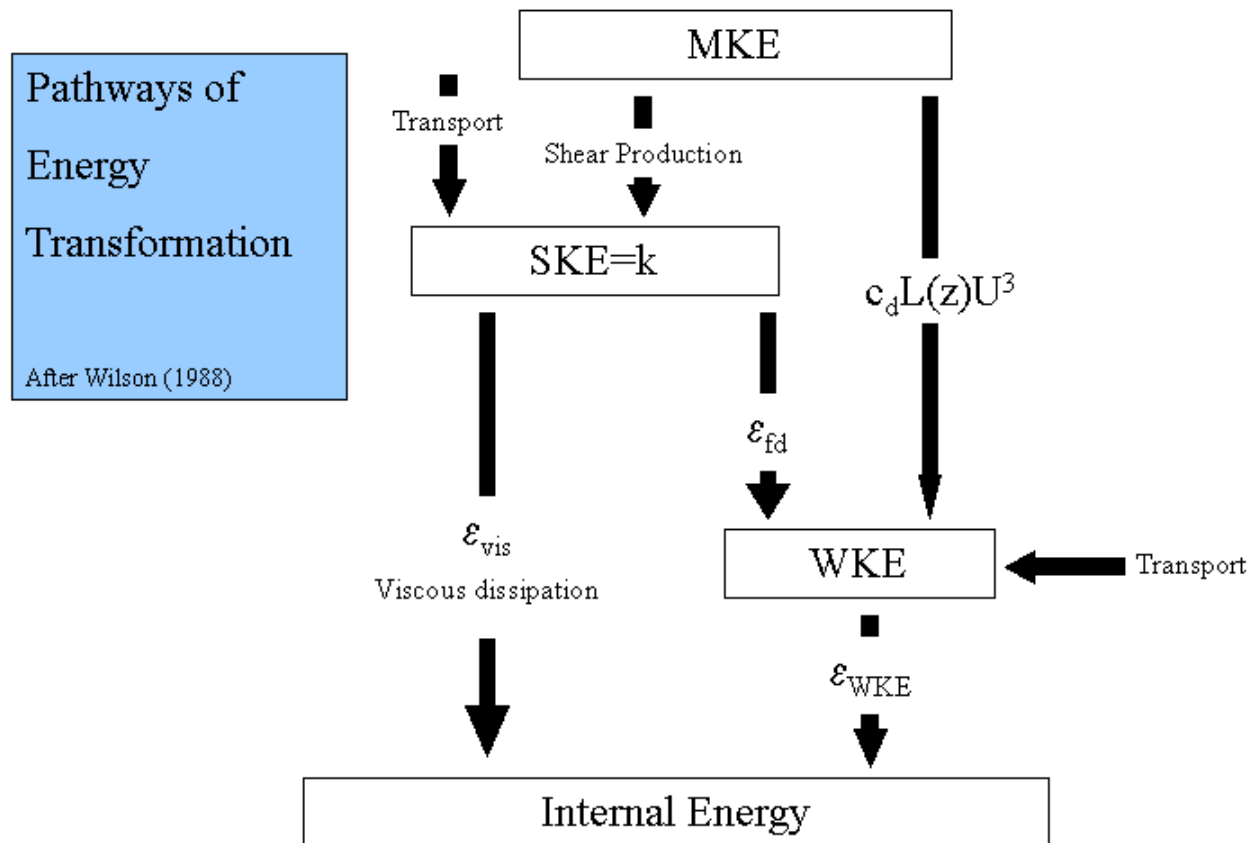


Figure 5. Conversion of mean kinetic energy (MKE) to resolved shear kinetic energy (SKE), inactive wake kinetic energy (WKE) and internal energy.

moisture and vertical velocity in forested canopies. The after-peak region of higher wave numbers associated with the inertial sub-range shows a slope steeper than the classical value of 2/3.

Evidence from simulations suggests that the normal energy cascade is bypassed. Simulations of a corn canopy by Wilson (1988) reveal that the conversion of "active" shear kinetic energy (SKE) to "inactive" wake kinetic energy (WKE) acts as a dissipative sink that balances shear production and turbulent transport. The pathway provided by drag may be thought of as the larger of two pipes, through which energy prefers to flow.

Some models capture the dual sinks of energy by partitioning turbulent kinetic energy into low-frequency (SKE) and high-frequency (WKE) bands. Instead of the invariant length scale λ used in our present model, a turbulent time scale governing the resolved band of SKE is used to close higher-order moments:

$$\tau = \frac{q^2}{\varepsilon} \quad (16)$$

where q^2 is one-half the turbulent kinetic energy (TKE) and ε is the total dissipation. In the absence of a meaningful ε budget equation for canopy flows, the loss of SKE is diagnosed from the flow field. One example of the rate of loss of SKE to WKE is that of Wilson et al. (1998):

$$\varepsilon_{fd} = 0.5C_d A(z)U (4 \langle \bar{u}'\bar{u}' \rangle + 2 \langle \bar{v}'\bar{v}' \rangle + 2 \langle \bar{w}'\bar{w}' \rangle) \quad (17)$$

where C_d is a bulk drag coefficient. This equation requires the tenuous assumption that $|u'| \gg |v'|, |w'|$ deep within the canopy. The viscous dissipation takes the form

$$\varepsilon_{cc} = \frac{q^3}{\Lambda \lambda} \quad (18)$$

where Λ is constant and λ is a length scale. This form was originally suggested by Mellor (1973) for the neutral surface layer. Far above the canopy, ε_{cc} is the only sink of

turbulent kinetic energy and approaches the correct limit as λ approaches $k(z-d)$, the expected von Karman length scale of a displaced surface layer.

The total loss of SKE may be the sum or the greater of the sinks to the high-frequency band and to internal energy:

$$\begin{aligned} \mathcal{E} &= \mathcal{E}_{cc} + \mathcal{E}_{fd} \\ \text{or} \quad \mathcal{E} &= \max(\mathcal{E}_{cc}, \mathcal{E}_{fd}) \end{aligned} \tag{19}$$

Whether energy prefers the path of least resistance or flows through both "pipes" in Figure 5 is a subtle point. Wilson et al. (1998) eliminated the "spectral shortcut" between SKE and WKE by setting \mathcal{E}_{fd} to zero and found that profiles of mean wind, Reynolds stress, and SKE were hardly affected. The loss of \mathcal{E}_{fd} was offset by a corresponding increase in \mathcal{E}_{cc} . This result supports the use of a single energy band in the present model. It is not sufficient, however, to justify lumping coherent and incoherent motions in a higher order closure model. If anything, the separate time and spatial scales of active and inactive canopy turbulence suggest that they not be co-parameterized. In light of the different scales revealed through Large Eddy Simulations (LES) of the canopy (Patton et al., 2001), some workers believe that higher-order closure may be getting the right statistics for the wrong reasons (Patton, personal communication).

Wilson et al (1998) studied a canopy of tombstones in which they questioned whether bluff-body interactions would transfer kinetic energy “not to irrelevant wake scales but to larger eddies within the waveband that k itself represents.” In other words, the long-wave roughness of the tombstones could contribute to resolved kinetic energy. This was suggested by the under-prediction of velocity variance by both first- and second-order closure models deep within the tombstone canopy. However, the proper selection of a mixing length made the issue moot: “In fact, for all three canopies we modeled, our profiles (of U , τ , k) are only *slightly* altered by eliminating the form-drag sink for TKE” (Wilson et al 1998; emphasis theirs). In other words, wake turbulence

does not feed back to larger scales and contribute to dispersion of scalars. In this study, I will assume that wake turbulence is “inactive.”

While coherent motions are familiar in the convective PBL, turbulence in tree canopies was long thought to be homogeneous. Strong evidence of the presence of microfronts in plant canopies was provided independently by Gao et al. (1989) and Collineau and Brunet (1993). Collineau and Brunet (1993) used a wavelet transform to detect ramp-like structures in time traces of velocity, temperature and their turbulent fluxes, while Gao et al. (1989) used a subjective visual identification. The former authors found a mean time interval $\Delta = 1.8h/u^*$ between contiguous coherent motions. A triple decomposition was performed on the conditionally averaged fluxes of sensible heat and momentum. Sweeps contributed a larger fraction of stress and sensible heat transfer: the ratio of stress fraction transferred by sweeps to that transferred by ejections was 1.04 at $z/h=1.24$ and 2.43 at $z/h=0.82$, while the ratios for sensible heat were 0.89 at $z/h=1.24$ and 1.82 at $z/h=0.82$. With different conditional sampling techniques, Gao et al. (1989) found that large-scale motions contributed as much as 75% of the heat and momentum transfer, while Collineau and Brunet (1993) found that large-scale contributions of sensible heat and momentum flux were 40% and 26% above the canopy and 39% and 31% within the canopy, respectively.

2.3 Vegetation Effects on the Isotope Composition of Canopy Air

The partitioning of matter between two substances of different isotopic compositions is referred to as fractionation. Plants and the atmosphere exist in an isotopically partitioned state brought about by fractionation due to two processes: kinetic effects, such as the different rates of diffusion and reaction among different isotopic species, and thermodynamic effects in the equilibrium balance of isotope exchange reactions.

Before we explain these effects, some conventions are in order. The isotopic composition of a compound is expressed as the ratio to some standard

$$\delta = \frac{R_A}{R_S} - 1 \quad (20)$$

where R_A is the ratio of the sample and R_S is the ratio of the standard. By convention, the standard $^{13}\text{C}/^{12}\text{C}$ ratio is that of a fossil belemnite from the Pee Dee formation (PDB) in South Carolina. The standard $^{18}\text{O}/^{16}\text{O}$ ratio is either PDB (for dry organic matter) or Standard Mean Ocean Water (SMOW; for water). The expression of δ is normally parts per mil.

The effect of a chemical process is expressed as the isotopic ratio of the reactant (R_R) and product (R_P):

$$\alpha = \frac{R_R}{R_P} \quad (21)$$

To amplify precision, isotope effects are expressed as discrimination:

$$\Delta = \alpha - 1 = \frac{R_a}{R_p} - 1 \quad (22)$$

where Δ is given in per mil units. Physically, when our reactant is the CO_2 in air and our product is plant matter, Δ is independent of source air composition. Mathematically, Δ is also independent of the standard. When weighted by the partial pressures of CO_2 in series, discriminations are additive.

Carbon Isotope Effects

The dominant mechanism behind carbon isotope discrimination in plants is the interplay between p_i/p_a , the ratio of internal to external CO_2 partial pressure, and the drawdown of CO_2 at Rubisco, which is governed by Rubisco activity. When stomatal resistance is limiting, the kinetic isotope effect associated with diffusion of CO_2 through air dominates; when the stomata are open, the effect of discrimination by Rubisco should be limiting. These effects are mediated by p_i/p_a . When Rubisco is limiting and conductance is high, p_i/p_a is large and the plant is choosy with its carbon; when stomatal

resistance is limiting and Rubisco is not, p_i/p_a is low and the plant uses all of the available carbon.

To see this mathematically, consider the diffusion of one gas into another, in which the diffusivity is related to the reduced molecular mass (Farquhar et al., 1982):

$$D_{12} \propto \left(\frac{m_1 m_2}{m_1 + m_2} \right) \quad (23)$$

The ratio of diffusivities of $^{12}\text{CO}_2$ to $^{13}\text{CO}_2$ in air is 1.004425, meaning that the discrimination associated with diffusion is 4.4 per mil. In contrast, the thermodynamic effect associated with Rubisco is ~30 per mil. The assimilation, A , of $^{12}\text{CO}_2$ is (Farquhar et al., 1982)

$$A = g(p_a - p_i) / P \quad (24)$$

where g is the series conductance of the boundary layer and stomatal pores, p_a and p_i , respectively, are the partial pressures of CO_2 in the atmosphere and the internal pore space, and P is the atmospheric pressure. The rate of fixation is given by

$$A = kc_i \quad (25)$$

where the parameter k depends on intercellular CO_2 . Combining the two equations above yields

$$A = \frac{kg/P}{k + g/P} c_a \quad (26)$$

An analogous set of equations applies to the assimilation of $^{13}\text{CO}_2$:

$$\begin{aligned} A' &= g'(c_a' - c_i') / P \\ A' &= k'c_i' \\ A' &= \frac{k'g'/P}{k' + g'/P} c_a' \end{aligned} \quad (26')$$

where $g' = g(1 - a/1000)$ and $k' = k(1 - b/1000)$. The isotopic ratio of reactant to product is then

$$\frac{A'/A}{c_a'/c_a} = \frac{k'(1 - a/1000) + g'(1 - b/1000)/P}{k' + g'/P} \quad (27)$$

and the resulting discrimination is

$$\Delta = \frac{k'a + g'b/P}{k' + g'/P} \quad (28)$$

Substituting Equation (26') into the above equation to replace g' gives

$$\Delta = a + (b - a) \frac{c_i'}{c_a'} \quad (29)$$

The ratio c_i'/c_a' is essentially equivalent to c_i/c_a . From Equation (22),

$$\Delta = \frac{\delta_{source} - \delta_{product}}{1 + \delta_{source}/1000} \quad (30)$$

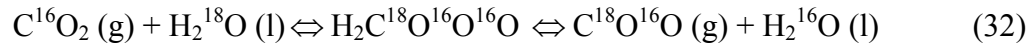
Applying this to plants and atmosphere,

$$\delta = \delta_{atm} - a - (b - a)c_i/c_a \quad (31)$$

As a rule of thumb, δ increases with water use efficiency (assimilation/transpiration).

Oxygen Isotope Effects

Consider first a closed container with an evaporating surface, in which gaseous CO_2 is moving in and out of solution. The equilibrium equation



The covalent bonds in the CO_2 molecule are more energetic than the ionic bonds in the H_2O molecule. To minimize free energy in this system at equilibrium, ^{18}O prefers to bond with carbon. The resulting fractionation between $\text{CO}_2/\text{H}_2\text{O}$ and H_2CO_3 is a thermodynamic effect, and occurs in the equilibration of CO_2 with leaf and soil water.

This thermodynamic effect is a constant background to the more variable kinetic effects. The diurnal evaporative enrichment of leaf water relative to the groundwater source occurs because H_2^{18}O evaporates more slowly than H_2^{16}O and because H_2^{18}O diffuses more slowly from the leaf. During photosynthesis, the heavier $\text{C}^{18}\text{O}^{16}\text{O}$ molecules diffuse more slowly into the leaf than do C^{16}O_2 . Of the CO_2 molecules that enter and exchange oxygen atoms with the enriched chloroplast water, approximately one third are ultimately assimilated, while two thirds diffuse back out into the canopy air space. The net effect of thermodynamic fractionation, diffusion and evaporative enrichment is a strong discriminatory signal in ^{18}O , which holds sway in the community effort to tease apart the photosynthetic and respiratory contributions of biomes to the global budget of CO_2 . The large enrichment of leaf water with respect to groundwater allows us to distinguish photosynthetic and respiratory effects at large scales (Farquhar et al., 1993; Ciais and Meijer, 1998).

Craig and Gordon (1965) derived the evaporative enrichment of a free water surface (δ_E) with respect to a source (δ_S):

$$\delta_E = (1 + \varepsilon^*)[1 + \varepsilon_k + (\delta_V - \varepsilon_k)e_a/e_i] - 1 \quad (33)$$

where δ_E and δ_V are isotopic compositions with respect to source water, e_a and e_i are the vapor pressures in the atmosphere and intercellular spaces, respectively, ε^* is the depression of equilibrium vapor pressure by the presence of ^{18}O , and ε_k is the kinetic fractionation factor. Bottinga and Craig (1969) gave us the following form for ε^* :

$$\varepsilon^* = [2.644 - 3.206(10^3/T) + 1.534(10^6/T^2)] \times 10^{-3} \quad (34)$$

The fractionation factor associated with the different diffusivities of H_2^{16}O and H_2^{18}O in free air is 28 per mil, while the fractionation for a laminar boundary layer, following the same 2/3 power law applied to carbon isotopes, is 19 per mil. One might simply assume that the two fractionations add in series, so that

$$\varepsilon_k = \frac{28r_s + 19r_b}{r_s + r_b} \times 10^{-3} \quad (35)$$

Differences between δ_E and the δ of whole leaf water are due to internal gradients in the leaf.

2.4 Soil Effects on the Isotopic Composition of Canopy Air

Soils and vegetation exist in a state of isotopic disequilibrium caused by secular trends in the isotopic composition of the atmosphere. The “Suess effect” refers to the lightening of the atmosphere’s $^{13}\text{C}/^{12}\text{C}$ ratio due to the burning of fossil fuels. Disequilibrium leads to a difference in isotopic composition of the inflow to the terrestrial biosphere (gross or net primary production) and its outflow (ecosystem or heterotrophic respiration). Hence, the age of the carbon leaving the terrestrial biosphere determines its isotopic composition. Plant respiration typically consists of very young carbon in the form of starches, and is influenced by factors such as temperature and stress. Soil respiration consists of older carbon and is controlled by factors such as temperature, texture, moisture, biota, relief, and nutrient availability.

The steady-state distribution of carbon leaving the system as a function of residence time is the impulse response of the system (Thompson and Randerson, 1999). The integral of the response function over time gives the total flux of carbon leaving the system:

$$\Phi_T = \int_0^{\infty} \Phi(\tau) d\tau \quad (36)$$

The impulse response function normalized by the total flux is the probability density function of transit times in the system. The impulse response function can be convolved against historical records of model tracer output to calculate the isotopic disequilibrium of ^{13}C in the terrestrial biosphere. The isodisequilibrium calculated in this fashion shows significant interannual variability. The mean residence time $\bar{\tau}$ of carbon in the system is the first moment of the kernel:

$$\bar{\tau} = \int_0^{\infty} \tau \Phi(\tau) d\tau \quad (37)$$

Similarly, Thompson and Randerson (1999) define a mean storage time \bar{T} as the first moment of a storage response function. The case $\bar{T} < \bar{\tau}$ describes the human population, in which the average age is much less than the average life expectancy; the case $\bar{T} = \bar{\tau}$ describes a well-mixed system in which the probability of respiration is the same for every particle; the case $\bar{T} > \bar{\tau}$ describes the soil carbon system, in which the probability of respiration declines with the time that a particle spends in the system.

The $^{13}\text{C}/^{12}\text{C}$ composition of respired CO_2 is thus dominated by the age or, equivalently, the depth or pool of the carbon source. The $^{18}\text{O}/^{16}\text{O}$ composition, in contrast, is determined largely by gradients of ^{18}O richness in soil water and the equilibration of dissolved CO_2 with $\text{H}_2^{18}\text{O}^{16}\text{O}$. The dissolution of CO_2 is catalyzed by the enzyme carbonic anhydrase. It is thought by Ciais et al. (1997) that even without carbonic anhydrase, CO_2 would diffuse upward slowly enough to fully equilibrate with soil water. These authors calculated the time for a CO_2 molecule to reach the surface from 30 cm depth as 6 hours. Here, $t = x^2/4D$, where D is the diffusivity of CO_2 in soil [$D = \kappa \epsilon_0 (1 - \beta) D_a$; ϵ_0 is the dry porosity (0.5); $(1 - \beta)$ the air-filled pore fraction of the soil (0.20), κ the tortuosity (0.66); and D_a the diffusivity of CO_2 in air ($0.15 \text{ cm}^2 \text{ s}^{-1}$)]. The tortuosity reflects the fact that the path of a CO_2 molecule around soil particles is circuitous. In comparison, the time $t = k_0 \epsilon_0 \beta$ required for the hydration of CO_2 in soil pores is about 7 minutes [k_0 is the rate of hydration in a reservoir of water at 10°C ($6.9 \times 10^{-3} \text{ s}^{-1}$)].

Based on these calculations, Ciais et al. (1997) opted to calculate the $\delta^{18}\text{O}$ of surface soil water from that of meteoric water and surface ground temperature and assumed that CO_2 was fully equilibrated. Only the fractionation of ^{18}O during diffusion of CO_2 between the soil surface and the atmosphere was calculated (about -5 per mille, in contrast to a calculation by Farquhar et al. (1993) of -7.6 per mille). Similarly, the

oxygen isotope fractionation model used in SiB2 takes the $\delta^{18}\text{O}$ of groundwater as fixed and applies a -5 per mille discrimination. The dominant influence of meteoric water on the $\delta^{18}\text{O}$ of soil water is ignored. In both models, soil CO_2 is assumed to be fully equilibrated with $\text{H}_2^{18}\text{O}^{16}\text{O}$.

The above procedures assume an abundance of unbound H_2O in soils, when in fact significant H_2O is adsorbed to soil surfaces. Carbonic anhydrase is assumed to be ubiquitous in soils. The effect of soil drying on gradients in ^{18}O near the soil surface and on the rate of hydration is neglected. Miller et al. (1999) explored these assumptions using soil sampling, chamber measurements, and gas chromatography measurements of soil CO_2 . These authors found that the $\delta^{18}\text{O}$ of respired CO_2 corresponds to apparent equilibrium with soil water at a depth of 5 to 15 cm, which is thought to correspond to partial equilibria over a range of depths. Large gradients in soil water composition in the upper 5 cm of soil did not influence the composition of respiration. Since the uncatalyzed hydration reaction occurs more slowly than diffusion of CO_2 out of the soil, any imprint of soil water from depths shallower than 5 cm in the presence of steep gradients in $\delta^{18}\text{O}$ of soil water would suggest the presence of carbonic anhydrase. In one out of five soil samples, the authors inferred the presence of catalysis. The assumption of instantaneously catalysed surface equilibration with a single diffusive fractionation appears to be false.

In this study, the apparent respiratory source was characterized using atmospheric measurements whenever possible. The simplistic model of soil equilibration was largely circumvented. A full discussion of this approach is found in the Methods section.

2.5 Recent Advances in Modeling Isotopic Exchange

Styles et al. (2001) optimized canopy and turbulence parameters in a Siberian coniferous forest canopy using measurements of three CO_2 species. A Lagrangian canopy turbulence model was combined with a two-stream, sunlit-shaded model of radiative transfer and isotopic fractionation models for oxygen and carbon. When

weighted for measurement error, the information in CO_2 and $\delta^{13}\text{C}$ was found to be more useful to the inversion than information in $\delta^{18}\text{O}$. The modeled carbon isotopic discrimination was lower than previously found for boreal ecosystems and was consistent with lower modeled values of intercellular CO_2 concentration. The optimized $dE/dA = \lambda$ (a Lagrange multiplier for the marginal water loss per unit carbon gain) was also low.

Styles et al. (2001) found that modeled carbon isotope discrimination decreased during the day and reasoned that increasing vapor pressure deficit, decreasing stomatal conductance and decreasing intercellular CO_2 concentration were the cause. Modeled oxygen isotope discrimination showed no clear trend, due to the opposing influence of vapor pressure deficit on leaf water and stomatal conductance.

A column mass balance within and above the plant canopy was considered by Lloyd et al. (1996). Using data from Amazonia and Siberia, Lloyd et al. (1996) divided the CBL into two reservoirs: one representing the canopy air space and the other representing the mixed layer above.

In the canopy model, one-way fluxes and their isotopic ratios were used in a one-dimensional isotopic molar mass balance:

$$M_i \frac{dR_i C_i}{dt} = R_o F_{oi} - R_{i(L)} F_{io} + R_R R - R_{i(A)} \frac{A}{1 + \Delta} \quad (38)$$

where R_i is the average $^{13}\text{CO}_2/^{12}\text{CO}_2$ ratio of the CO_2 within the column, C_i is the column average storage of the CO_2 species, R_o is the $^{13}\text{CO}_2/^{12}\text{CO}_2$ ratio of the CO_2 entering the column from above, $R_{i(L)}$ is the $^{13}\text{CO}_2/^{12}\text{CO}_2$ ratio of air leaving the column, R_R is the $^{13}\text{CO}_2/^{12}\text{CO}_2$ ratio of respired CO_2 entering the column, $R_{i(A)}$ is the $^{13}\text{CO}_2/^{12}\text{CO}_2$ ratio of assimilated CO_2 , and Δ is discrimination by photosynthesis. Horizontal advection was ignored. The canopy air space was later assumed to be well mixed so that $\delta_i = \delta_{i(L)} = \delta_{i(A)}$ and the equations were re-expressed in δ notation:

$$M_i C_i \frac{d\delta_i}{dt} = F_{oi} (\delta_o - \delta_i) + R(\delta_R - \delta_i) + A\Delta \quad (39)$$

The authors then defined the net ecosystem discrimination as the bulk effect of discriminatory fluxes:

$$\Delta_E = \frac{A\Delta + R(\delta_R - \delta_i)}{A - R} \quad (40)$$

Combining the two equations above yields the following empirical expression of net ecosystem discrimination:

$$\Delta_E = \frac{M_i C_i \frac{d\delta_i}{dt} - F_{oi} (\delta_o - \delta_i)}{F_{oi} - F_{io} - M_i \frac{dC_i}{dt}} \quad (41)$$

The one-way fluxes in Equation (41) were approximated using an eddy flux technique in which the conditional average mass transports were calculated. The mass transport across a plane uncontaminated by mean motion was divided into mean and fluctuating components.

$$F_{io} = \overline{(\rho w)'} C_{i(L)} \quad F_{oi} = \overline{(\rho w)'} C_o \quad (42)$$

In practice, the authors found that the storage terms in Equation (41) were small so that a good approximation to Equation (41) involves only F_{oi} , F_{io} , δ_o and δ_i .

The recycling of respired CO_2 by the forest canopy is defined here as $A/(A + F_{io})$. This parameter was always less than 0.01. Recycling was found to be greater in the Amazon, even though one-way fluxes were the same. In reality, recycling is not simply driven by assimilation but is also governed by buoyancy, mixing efficiency, and canopy structure. In addition, Lloyd et al. (1996) assumed that the composition of air immediately above the canopy reflected tropospheric values, which it does not. Due to greater respiratory and assimilatory fluxes but similar isotopic fractionations, the tropical

forest was found to exert a greater influence on the isotopic composition of the surrounding air than the boreal forest.

Lloyd et al. (1996) only quantified instantaneous recycling underneath a daytime convective PBL and found it to be small. Of greater relevance to PBL budgets of CO₂ is the assimilation-weighted daily average recycling rate, which is modulated by the relative timing of turbulent ventilation and the growth of assimilation in the morning. This early morning contribution was not modeled by Lloyd et al. (1996) and is potentially significant. Capturing this effect requires an adequate representation of the transition from a statically stable nighttime PBL to daytime convection. This is a point of weakness in many existing PBL parameterizations, including the mixed layer model used by these authors. Static stability is also the Achilles heel of canopy models today. It is likely that Lloyd et al. (1996) have underestimated the potential recycling of respired canopy air.

The authors also applied a prognostic model of a well-mixed CBL, taking into account the diurnal cycle in mixed layer height. The reassimilation of respired CO₂ within the CBL was taken as the ratio $A_R/(A_T+A_R)$, where A_R is the rate of canopy assimilation of CO₂ molecules that have been recently respired and have not recently entered the atmosphere above the CBL, and A_T is the rate of assimilation of CO₂ molecules that have originated from the free troposphere. A coupled model of molar conservation in which respiratory and tropospheric values were separately prognosed was developed for the canopy and mixed layers. The value of the ratio $A_R/(A_T+A_R)$ decreased monotonically in the canopy layer before leveling off near noon; the ratio peaked in the mixed layer in the early morning and also leveled off before noon. The ratio converged to a value below 0.1 in both layers. The decline of this ratio after sunrise was driven by convective mixing and stronger coupling between the two layers. The ratio was nearly independent of assimilation and scaled linearly with the ecosystem respiration rate. The ratio was generally lower in Siberia than in the Amazon.

Buchmann et al. (1997) looked for seasonal differences in the relative magnitudes of turbulent mixing and ecosystem exchange in a rainforest in French Guiana. These

authors took numerous snapshots of CO₂ gradients and isotopic composition over a 5-day period in each season. While they did not control for the intermittency of turbulent mixing, these authors found systematic and intuitive differences and generalized them to season and stand structure. Open stands showed greater enrichment in ¹³C and depletion in CO₂ due to the presence of a vigorous understory. The resulting diurnal cycles suggest little seasonal difference in the relative magnitudes of turbulent mixing and ecosystem exchange. During the dry season, soil CO₂ efflux was higher and local gradients of CO₂ were stronger near the soil surface. After rain events, soil respiration decreased. The inhibition of respiration in moist soils was possibly due to decreased diffusion or oxygen deficiency.

2.6 The Canopy and the Planetary Boundary Layer

Bottom-Up and Top-Down Diffusion

The analogy of bottom-up and top-down diffusion is developed by Wyngaard (1983) in an attempt to generalize mixed-layer similarity to include the effects of entrainment. Moeng and Wyngaard (1984) decompose the ensemble mean scalar mixing ratio $\langle C \rangle$ and the perturbation field c into the top-down and bottom-up components $\langle C \rangle_t$, $\langle C \rangle_b$, c_t , and c_b , respectively. The total mixing ratio C becomes

$$C = \langle C \rangle + c = \langle C \rangle_t + \langle C \rangle_b + c_t + c_b \quad (43)$$

In a laboratory experiment, the subscripts b and t might denote two different dyes which are released at the bottom and the top of the tank, respectively. Considering two dyes of the same color leads to the superposition hypothesis. If one considers the b dye alone, the relevant variables must be the height (z), the depth of the tank (h), the surface scalar flux ($\langle w c \rangle_s$), and the convective velocity scale ($w_* = (g \langle w \theta \rangle_s h / \langle \theta \rangle)^{1/3}$). The brackets indicate an ensemble mean, while w and θ are deviations from the mean state. In the limiting case of free convection, the friction velocity vanishes. Dimensional analysis then implies the existence of a gradient function

$$g_b = - (w_* h / \langle w c \rangle_s) \partial \langle C \rangle_b / \partial z \quad (44)$$

The relevant variables for the t dye are the height, the depth of the tank, the convective velocity scale, and the scalar flux at h ($\langle wc \rangle_l$). The gradient function for the t dye is

$$g_t = - (w^*h / \langle wc \rangle_l) \partial \langle C \rangle_l / \partial z \quad (45)$$

The gradient functions capture the efficiency with which turbulent energy is transferred to smaller scales. A smaller gradient function corresponds to more efficient vertical diffusion. Are the two gradient functions alike? No. While the energy applied to the surface flux is externally imposed, the energy that drives entrainment is limited by the efficiency with which energy trickles up through the PBL. Exceptions include the case of stratocumulus clouds, where radiative cooling is leading to atmospheric instability aloft and shear, which also drives entrainment. Because energy is lost through viscous dissipation, entrainment will always be less “efficient” than the surface process of bottom-up diffusion. The flux of buoyancy in the entrainment zone will be smaller than the surface flux.

Under quasi-steady conditions, the scalar flux at any height in the mixed layer is a linear combination of the surface and entrainment fluxes, so that

$$\langle wc \rangle = \langle wc_t \rangle + \langle wc_b \rangle = z/h \langle wc \rangle_l + (1 - z/h) \langle wc \rangle_s \quad (46)$$

The conceptual decomposition of two transport processes leads to a separate closure assumption for each of the two fluxes

$$\langle wc_t \rangle = - K_t \partial \langle C \rangle_l / \partial z \quad (47)$$

$$\langle wc_b \rangle = - K_b \partial \langle C \rangle_b / \partial z$$

The physical assumption of local, down-gradient diffusion is no more valid for each transport component than it is for the total process. Substituting the closure assumptions into the expressions for the component fluxes leads to the following expressions for the diffusivities:

$$K_t = zw^* / g_t \quad (48)$$

$$K_b = (1 - z/h) w^*h / g_b$$

In the simulations of Moeng and Wyngaard (1984), the bottom-up gradient function passes through zero within the PBL, creating a singularity in K_b . The assumption of local transport fails where the gradient function vanishes, and non-local transport of the scalar is implied.

Like the scalar flux, the variances and covariance of the two processes can be expressed in terms of dimensionless variance functions

$$\begin{aligned} \langle c_b^2 \rangle &= f_b (\langle wc \rangle_s / w_*)^2 \\ \langle c_t^2 \rangle &= f_t (\langle wc \rangle_l / w_*)^2 \\ \langle c_b c_t \rangle &= f_{bt} (\langle wc \rangle_s \langle wc \rangle_l) / w_*^2 \end{aligned} \quad (49)$$

The co-existence of surface and entrainment fluxes leads to a covariance between the bottom-up and top-down processes. The variance of the total scalar field becomes

$$\langle c^2 \rangle = \langle (c_t + c_b)^2 \rangle = \langle c_t^2 + 2 c_b c_t + c_b^2 \rangle \quad (50)$$

Substituting Equations 49 into the above equation yields an expression for the total variance as a function of the convective velocity scale and the driving fluxes

$$\langle c^2 \rangle = f_t (\langle wc \rangle_l / w_*)^2 + 2 f_{bt} (\langle wc \rangle_s \langle wc \rangle_l) / w_*^2 + f_b (\langle wc \rangle_s / w_*)^2 \quad (51)$$

The correlation between the two processes can be measured by the correlation coefficient $r = f_{bt} / (f_t f_b)^{1/2}$. This correlation is greatest in the middle of the PBL, where both transport processes are important.

These authors apply the analogy of top-down and bottom-up diffusion to the time-dependent budgets of scalar fluxes and variances. The authors also compare modeled variances of temperature and moisture with historical observations. The simulations illustrate the limitations of a local eddy-diffusivity closure in the convective PBL. Individual terms in the budgets of scalar flux and variance reveal the structure of turbulence in the PBL and provide insight into higher order closure.

Tree Canopies and Diffusion

A tree canopy provides a distributed source of scalar flux to a transport process that is altered by the presence of the canopy itself. That canopies influence bottom-up diffusion is no surprise. The greater mystery of Moeng and Wyngaard (1984) is that for large ratios of the entrainment and surface fluxes, top-down diffusion can influence the scalar variance profile all the way down to the surface. It seems possible then that the presence of a canopy where the ratio of entrainment and surface fluxes is small might influence the scalar variance profile at the top of the PBL. An eddy-resolving model is the chosen tool to answer this question. Patton et al. (2000) ask whether canopies might influence top-down diffusion and find that only bottom-up diffusion is significantly altered.

The authors present the results of two large-eddy simulations of the convective PBL. One simulation includes the presence of a forest canopy and one does not. A drag term in the Navier-Stokes equations represents the aerodynamic presence of the canopy. The drag imposed on the flow by the canopy is written as the product of a drag coefficient (C_d), a one-sided leaf area density (a), and the square of an instantaneous velocity u_i :

$$F_i = -C_d a U u_i \quad (52)$$

where F_i is three-dimensional and time-dependent and U is the magnitude of the wind speed $(u_i u_i)^{1/2}$. An upward sensible heat flux from the canopy to the surrounding air decreases exponentially with depth toward the surface. The sensible heat flux integrated over the depth of the canopy is equal to the surface sensible heat flux in the no-canopy case. The canopy-integrated source of the bottom-up scalar is also equal to the surface scalar flux in the no-canopy case.

Twenty-four time realizations are averaged in Patton et al. (2000). A nested grid model is used to allow both adequate resolution of the canopy layer and coverage of the

full convective PBL. Both cases are driven by a geostrophic wind of 5 ms^{-1} , compared to a value of 10 ms^{-1} used by Moeng and Wyngaard (1984).

Top-down diffusion is unaffected by the presence of the tree canopy. This is not surprising, since the canopy is not a source of the top-down scalar. Turbulence structure in the entrainment region near the PBL top is not affected by the presence of enhanced turbulence in the roughness sublayer above the canopy. In contrast, bottom-down diffusion is significantly influenced by the presence of the canopy. Smaller values of the gradient function g_b throughout the lower PBL suggest that diffusion is enhanced. The difference in g_b extends all the way up to $z \sim 0.6 h$, the level at which the gradient function passes through zero and the assumption of local transport no longer applies.

The profiles of the scalar variance functions f_t and f_b echo the profiles of the gradient function. Top-down scalar variance is unaltered, while bottom-up scalar variance is slightly smaller in magnitude than that in the no-canopy case. The pattern is consistent with the relationship between scalar flux and variance. Patton et al. (2000) observe that mean gradient production is the greatest source of variance; this element is the product of the flux and the mean scalar gradient. However, the difference in the variance function extends throughout the entire depth of the PBL. Patton et al. (2000) offer no explanation for this difference in the vertical extent of the influence of the canopy.

These authors present recent results concerning the influence of the canopy on top-down and bottom-up diffusion in the convective PBL. The influence of the canopy on the covariance between transport processes and on the time-dependent budgets of turbulent statistics are possible continuations of this work. New investigations of top-down and bottom-up diffusion in higher order closure models and the coupling of closure models between the canopy and the PBL follow from these experiments.

3

Methods

In this study, I had the luxury of selecting methods which I hoped would fulfill certain long-term goals, and which did ultimately fulfill a set of revised and realistic objectives. The evolution of these methods is described in five parts: first, an overview of the experimental design; second, a formalization of the selection of methods; third, a description of the numerical methods; fourth, a description of the field and laboratory methods; and fifth, a description of the synthesis of models and data.

3.1 Experimental Design

A diagram of model-data synthesis is presented in Figure 11. At the heart of the experimental design is the disaggregation of a bulk eco-physiological model using a Beer's law extinction of photosynthetically active radiation with cumulative leaf-area depth in the canopy. At the boundary of the transport model, disaggregation yields scaled source distributions of three passive tracers: $^{12}\text{C}^{16}\text{O}^{16}\text{O}$, $^{12}\text{C}^{18}\text{O}^{16}\text{O}$, and $^{13}\text{C}^{16}\text{O}^{16}\text{O}$. Measured internal boundary conditions at the canopy top and soil respiratory fluxes prognosed by SiB determine the transport problem.

Meteorological forcing was provided by local observations. Physiological state variables were derived from literature and remote sensing observations of the geographic region. The modeled physiology was prognosed at 30-minute time steps, while transport in the vertically resolved model was perfectly stationary and without memory. One

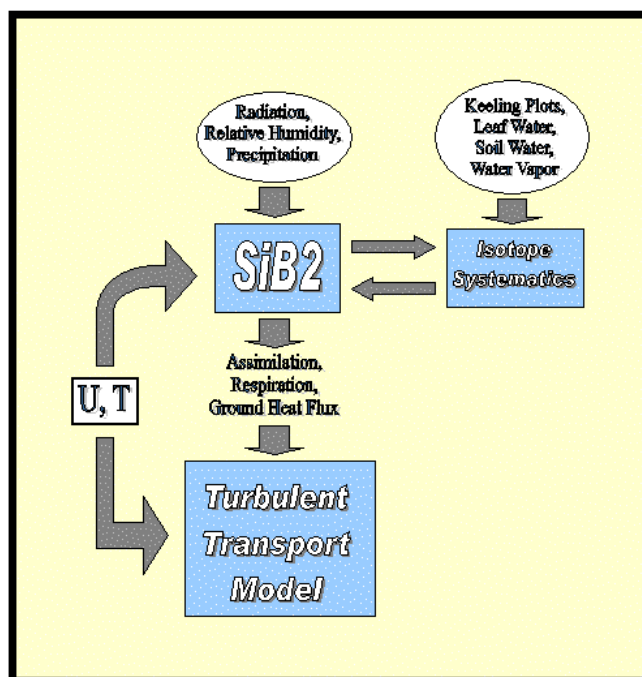


Figure 11. Flowchart of the experimental design of a forward test of tracer transport and physiological scaling.

disengenuity in the design was the presence of bulk aerodynamics in SiB2, with fixed assumptions regarding friction velocity, canopy roughness length, or displacement height.

The design of field experiments served three purposes: a direct comparison of measured and modeled isotope signals; direct boundary conditions for the transport model; and indirect constraints on isotope systematics in the bulk physiology model. Samples taken in the field included air profiles within the canopy, soil water, leaf water and organic carbon, water vapor profiles, and nighttime characterizations of the isotopic composition of the respiratory source.

Each field experiment was progressively designed to fill in knowledge gaps regarding stable isotope plant physiology. A regional characterization of ecosystem stable isotope exchange was underway at the time: the nighttime respiratory signature in the boundary layer was characterized, neighboring ecosystems were sampled physiologically and their leaf, respiratory and ecosystem isotope exchanges were

characterized. One of these ecosystem sites was a mature upland hardwood site thought to be physiologically similar to the site at which this study was conducted. While these studies were underway, continuous micrometeorological measurements in the boundary layer were taken at a neighboring tall TV tower. Contextual weather information and boundary layer richness data both proved useful to the interpretation of events at the canopy site.

3.2 The Selection of Methods and the Fulfillment of Goals

As discussed in the Introduction, two of the long-term goals were to quantify recycling under stably stratified conditions and to invert a tracer transport model for vegetative fluxes (see the discussion of future work in the Conclusion). To develop the next generation of aerodynamics in SiB, I needed to find a balance between realism and frugality. In the forward sense, it might have sufficed to use 1-1.5-order closure in a multi-layered domain. The original goals of quantifying recycling and inverting a tracer transport model mandated the use of more complex dynamics. An Eulerian model is appealing because it provides powerful statistical information. The development of a coupled Lagrangian model which uses Eulerian statistics would follow naturally from this initial choice.

The choice of SiB as a bulk plant physiological and soil respiration model was expedient and promised the fulfillment of another long-term goal: a true test of bulk plant physiological assumptions using a vertically resolved transport model. As it turned out, the forward modeling approach and sampling design ultimately caused this thesis to become a physiological validation study. To truly test the assumptions of bulk physiology and a well-mixed canopy air space, one must make certain homogeneous assumptions in the tracer transport model and invert (see the discussion of future work in the Conclusion).

Measurement methods for air sampling were designed to fulfill the long-term goal of a coupled mass balance solution between a tall canopy and the PBL. Quantifying and constraining boundary conditions to the transport model, such as soil respiration and the

isotopic composition of photosynthate, determined measurement methods for plants and soil. Opportunities to validate (or refute) our understanding of isotope systematics arose in the field and certain sampling strategies (such as the isotopic composition of water vapor) exploited those opportunities.

3.3 Modeling Methods

The Momentum Equations

The canopy airspace is a reticulate and multiply intersecting domain in which the air is a porous enclosure about a chemically and thermodynamically active substrate. In the land-surface applications that were considered in the previous chapter, volume averages may be on the scale of kilometers. Even at the scale of a single canopy stand, a closed parcel of air will nearly enclose multiple intersecting plant parts. Some intellectual reconciliation between landscape and stand-scale heterogeneity is needed, for we cannot simply assume that perturbations tend towards zero at very large distances. In this application, the averaging volume is on the scale of a cubic meter. Hence we refer to a “multiply-connected domain” at all scales. In the free atmosphere, spatial and temporal averages are commutable; in the multiply connected domain, residual terms arise from horizontal averaging, such as the horizontal and vertical variations in pressure as air flows around an obstacle. In a multiply-connected domain, Gauss’s divergence theorem takes on new implications (Finnigan, 1985):

$$\begin{aligned} \left\langle \frac{\partial}{\partial x_j} a_j \right\rangle &= \frac{1}{V} \iiint_V \frac{\partial a_j}{\partial x_j} dx_1 dx_2 dx_3 \\ &= -\frac{1}{V} \iint_{S_0} a_j n_j - \frac{1}{V} \sum_{i=1}^m \iint_{S_i} a_j n_j ds \end{aligned} \quad (100)$$

where brackets denote a volume average, a_j is any vector, n_j is the normal projecting outward from the leaf, and S_i are the surfaces of m leaves in the averaging volume. The last term in the equations above is what will become a source term and m will remain

arbitrary. Using Leibniz's rule without regard to the multiply-connected domain, we find that

$$\frac{\partial}{\partial x_j} \langle a_j \rangle = -\frac{1}{V} \iint_{S_0} a_j n_j ds \quad (101)$$

First, consider the following simple scalar conservation equation (Finnegan, 1985):

$$\frac{\partial c}{\partial t} + \frac{\partial}{\partial x_j} (u_j c) = \frac{\partial}{\partial x_j} \left(k_c \frac{\partial c}{\partial x_j} \right) \quad (102)$$

where we have assumed incompressibility and a boundary condition of no normal flow across the solid surface. After horizontal or volume averaging,

$$\frac{\partial \langle c \rangle}{\partial t} + \frac{\partial}{\partial x_j} \langle u_j c \rangle = \frac{\partial}{\partial x_j} \left\langle k_c \frac{\partial c}{\partial x_j} \right\rangle - \frac{1}{V} \sum_{i=1}^m \iint_{S_i} k_c \frac{\partial c}{\partial n} ds \quad (103)$$

where the last term on the RHS is the molecular flux of a scalar from the leaves into the averaging volume. Similar residual terms arise on the LHS which cancel. By further decomposing the time mean into a spatial average and the deviation from that average, we find that

$$\langle u_j c \rangle = \langle \overline{u_j c} \rangle + \langle \overline{u_j}' \overline{c}' \rangle \quad (104)$$

If $\overline{u_j} = \langle \overline{u_j} \rangle + \overline{u_j}''$ and $\overline{c} = \langle \overline{c} \rangle + \overline{c}''$, then

$$\langle \overline{u_j c} \rangle = \langle \overline{u_j} \rangle \langle \overline{c} \rangle + \left\{ \langle \overline{u_j}' \overline{c}' \rangle - \langle \overline{u_j} \rangle \langle \overline{c} \rangle + \langle \overline{u_j} \rangle \overline{c}'' + \langle \overline{u_j}'' \overline{c} \rangle + \langle \overline{u_j}'' \overline{c}'' \rangle \right\} \quad (105)$$

The term in brackets is a dispersive flux, which in practice is found to be small in vegetative canopies. Finnigan (1985) pointed out that

$$\langle \overline{u_j}' \overline{c}' \rangle = \langle \overline{u_j} \rangle \langle \overline{c} \rangle + 0 \left(\frac{r^2}{6L^2} \right) \quad (106)$$

where $2r$ is the length of the side of an averaging box and L is the scale of variations in $\langle u_j \rangle$ or $\langle c \rangle$ parallel to r . Or equivalently, when taking a temporal average

$$\overline{\overline{ab}} = \overline{ab} + 0(T/\tau) \quad (107)$$

where T is the averaging period and τ is the time scale for changes in \bar{a} and \bar{b} . After substituting the volume-averaged form of the continuity equation, and neglecting the dispersive flux, the flux form of the scalar conservation equation becomes

$$\frac{\partial}{\partial t} \langle c \rangle + \frac{\partial}{\partial x_j} \langle u_j c \rangle = \langle u_j \rangle \frac{\partial}{\partial x_j} \langle c \rangle + \frac{\partial}{\partial x_j} \langle u_j' c' \rangle \quad (108)$$

Next, consider the equations of motion for a Boussinesq-approximated flow. The unaveraged equations are

$$\frac{\partial u_i}{\partial t} + u_j \frac{\partial u_i}{\partial x_j} = -\frac{1}{\rho} \frac{\partial p}{\partial x_i} + \nu \frac{\partial^2 u_i}{\partial x_j \partial x_j} + \beta_i \Theta + f \varepsilon_{ij3} u_j \quad (109)$$

$$\frac{\partial \Theta}{\partial t} + u_j \frac{\partial \Theta}{\partial x_j} = \kappa \frac{\partial^2 \Theta}{\partial x_j \partial x_j} \quad (110)$$

where $\beta = (0, 0, \alpha g)$, α in this study is the inverse of the domain-averaged temperature, ν is a kinematic viscosity, and κ is a thermal diffusivity. After decomposing $u = \bar{u} + u'$ and $\Theta = \bar{\Theta} + \theta'$ and taking a time mean, these equations become

$$\frac{\partial \bar{u}_i}{\partial t} + \bar{u}_j \frac{\partial \bar{u}_i}{\partial x_j} + \frac{\partial \overline{u_i' u_j'}}{\partial x_j} = -\frac{1}{\rho} \frac{\partial \bar{p}}{\partial x_i} + \nu \frac{\partial^2 \bar{u}_i}{\partial x_j \partial x_j} + \beta_i \bar{\Theta} + f \varepsilon_{ij3} \bar{u}_j \quad (111)$$

$$\frac{\partial \bar{\Theta}}{\partial t} + \bar{u}_j \frac{\partial \bar{\Theta}}{\partial x_j} + \frac{\partial \overline{u_j' \theta'}}{\partial x_j} = \kappa \frac{\partial^2 \bar{\Theta}}{\partial x_j \partial x_j} \quad (112)$$

For now, we consider only the mean momentum equation. By decomposing $\bar{u}_i = \langle \bar{u}_i \rangle + \bar{u}_i''$ and averaging over a horizontal plane or volume, Equation (111) becomes

$$\begin{aligned}
& \frac{\partial \langle \overline{u_i} \rangle}{\partial t} + \langle \overline{u_j} \rangle \frac{\partial \langle \overline{u_i} \rangle}{\partial x_j} + \underbrace{\frac{\partial \langle \overline{u_i'' u_j''} \rangle}{\partial x_j}}_I + \frac{\partial \langle \overline{u_i' u_j'} \rangle}{\partial x_j} = - \underbrace{\frac{1}{\rho} \frac{\partial \langle \overline{p} \rangle}{\partial x_i}}_{II} - \underbrace{\frac{1}{\rho} \left\langle \frac{\partial \overline{p''}}{\partial x_i} \right\rangle}_{III} + \underbrace{\nu \frac{\partial^2 \langle \overline{u_i} \rangle}{\partial x_j \partial x_j}}_{IV} \\
& + \underbrace{\nu \left\langle \frac{\partial^2 \overline{u_i''}}{\partial x_j \partial x_j} \right\rangle}_{IV} + \beta_i \overline{\Theta} + f \varepsilon_{ij3} \langle \overline{u_j} \rangle
\end{aligned} \tag{113}$$

A dispersive flux appears in Terms I, which is neglected. Terms II and IV arise from the noncommutivity of differentiation and integration over a multiply connected domain. Term II is a form drag term, while Term IV is a viscous drag term. The second moment equation is similarly averaged to yield

$$\begin{aligned}
& \frac{\partial \langle \overline{u_i' u_k'} \rangle}{\partial t} = - \left(\langle \overline{u_j' u_k'} \rangle \frac{\partial \langle \overline{u_i} \rangle}{\partial x_j} + \langle \overline{u_i' u_j'} \rangle \frac{\partial \langle \overline{u_k} \rangle}{\partial x_j} \right) - \underbrace{\left(\frac{\partial \langle \overline{u_i u_j u_k} \rangle}{\partial x_j} \right)}_V - \underbrace{\left(\left\langle \overline{u_k'} \frac{\partial \overline{p'}}{\partial x_i} \right\rangle + \left\langle \overline{u_i'} \frac{\partial \overline{p'}}{\partial x_k} \right\rangle \right)}_{VI} \\
& + \underbrace{\left(\langle \overline{u_k} \rangle \left\langle \frac{\partial \overline{p''}}{\partial x_i} \right\rangle + \langle \overline{u_i} \rangle \left\langle \frac{\partial \overline{p''}}{\partial x_k} \right\rangle \right)}_{VII} + \underbrace{\nu \left(-2 \left\langle \frac{\partial \overline{u_i'} \partial \overline{u_k'}}{\partial x_j \partial x_j} \right\rangle + \left\langle \frac{\partial^2 \overline{u_i'' u_k''}}{\partial x_j \partial x_j} \right\rangle \right)}_{VIII} - \underbrace{\beta_i \overline{\theta u_k} - \beta_k \overline{\theta u_i}}_{IX}
\end{aligned} \tag{114}$$

The Momentum Parameterizations

Before moving on to the closure assumptions used to approximate the terms above, it is timely to discuss the importance of length scales. Many of the closure assumptions used below use a master length scale λ and a velocity scale q , which is twice the turbulent kinetic energy, or $\langle \overline{u'^2} \rangle + \langle \overline{v'^2} \rangle + \langle \overline{w'^2} \rangle$. The higher-order eddy diffusivity [$\text{m}^2 \text{s}^{-1}$] used to represent the turbulent transport of second moments, for example, is a coefficient, times q , times λ . Given the confined nature of canopy flows, and the absence of a meaningful prognostic equation for dissipation, the importance of a governing length

scale should be obvious. The prescribed length scale λ_i is limited by the geometry of the canopy and the scaling of a free surface layer:

$$\begin{aligned}\lambda_i &= a_i L; \quad i=1,2,3 \\ L &= \min\left(\frac{\alpha}{C_d A(z)}, kz\right) \\ \left|\frac{dL}{dz}\right| &\leq k\end{aligned}\tag{115}$$

where $A(z)$ [m^2m^{-3}] is the leaf area density as a function of height, C_d is a dimensionless drag coefficient, α is a dimensionless coefficient chosen along with C_d , and k is the von Karman coefficient (~ 0.4). The coefficients a_i correspond to length scales for the turbulent diffusion of second moments, pressure transport, and dissipation, respectively. The constants a_i and C_w are tuned to the asymptotic ‘outer’ limit of the inertial layer above the canopy, which simply means that production is set equal to dissipation, transport is neglected, and the coefficients are solved analytically. The coefficients α and C_d correspond to a particular canopy architecture, so that simulated and measured mean velocities have the closest correspondence given u^* .

Now we are ready to move on to the approximation of terms in the mean momentum and second velocity moment equations. Term II in the mean momentum equation and Term VII in the second moment equation are parameterized as form drag to the second and third power of mean velocity, respectively, e.g.:

$$\left\langle \frac{\partial p''}{\partial x_i} \right\rangle = C_d A(z) \langle \overline{u_i} \rangle^2\tag{116}$$

Term IV in the mean momentum equation is neglected, so that all drag due to the presence of the canopy is form drag. Since Term III in the mean momentum equation scales with the Reynolds number, it is neglected for canopy flows.

In the second moment equation, Term V is parameterized using a simple downgradient diffusion approximation:

$$\frac{\partial \langle \overline{u_i u_j u_k} \rangle}{\partial x_j} = \frac{\partial}{\partial x_j} \left(q \lambda_1 \left(\frac{\partial \langle \overline{u_i' u_j'} \rangle}{\partial x_k} + \frac{\partial \langle \overline{u_j' u_k'} \rangle}{\partial x_i} + \frac{\partial \langle \overline{u_k' u_i'} \rangle}{\partial x_j} \right) \right) \quad (117)$$

Expanding Term VI in the second moment equation yields

$$\left\langle \overline{u_i' \frac{\partial p'}{\partial x_k}} \right\rangle + \left\langle \overline{u_k' \frac{\partial p'}{\partial x_i}} \right\rangle = - \left\langle \overline{p' \frac{\partial u_i'}{\partial x_k}} \right\rangle - \left\langle \overline{p' \frac{\partial u_k'}{\partial x_i}} \right\rangle + \left\langle \overline{\frac{\partial p' u_i'}{\partial x_k}} \right\rangle + \left\langle \overline{\frac{\partial p' u_k'}{\partial x_i}} \right\rangle \quad (118)$$

The latter two terms on the RHS above are believed to be negligible. When we derive Poisson's equation (by taking the divergence of the mean momentum equation), we find three terms: non-linear turbulent self-interactions, mean-shear turbulence interactions, and buoyancy-turbulence interactions. The “slow” self-interactions are modeled as return-to-isotropy (Rotta 1951), while similar forms were modified by Launder et al. (1975), Lumley (1979) and others to parameterize the mean shear-turbulent interactions and the buoyancy- turbulence interactions. The form of closure used in this model is

$$\begin{aligned} \left\langle \overline{p' \frac{\partial u_i'}{\partial x_k}} \right\rangle + \left\langle \overline{p' \frac{\partial u_k'}{\partial x_i}} \right\rangle = & - \frac{q}{3 \lambda_2} \left[\langle \overline{u_i' u_k'} \rangle - \delta_{ik} \frac{q^2}{3} \right] + C_w q^2 \left[\frac{\partial \langle \overline{u_i} \rangle}{\partial x_k} + \frac{\partial \langle \overline{u_k} \rangle}{\partial x_i} \right] \\ & - \frac{3}{10} \beta_l \left(\overline{\theta u_i} \delta_{lk} + \overline{\theta u_k} \delta_{li} - \frac{2}{3} \overline{\theta u_l} \delta_{lk} \right) \end{aligned} \quad (119)$$

where another dimensionless coefficient C_w appears. Moving on to Term VIII, the first part is a viscous dissipation:

$$2\nu \left(\left\langle \overline{\frac{\partial u_i'' \partial u_k''}{\partial x_j \partial x_j}} \right\rangle \right) = \frac{2q^3}{3\lambda_3} \delta_{ik} = \frac{2}{3} \langle \varepsilon \rangle \delta_{ik} \quad (120)$$

where ε is the dissipation of turbulent kinetic energy. The second part of Term VIII is neglected. The resulting equations of motion are shown below. The meridional momentum equations have been omitted for clarity, while the applied model equations

include coupling between zonal and meridional momentum. Horizontal homogeneity is assumed and spatial and temporal averaging are implied.

Zonal Mean Momentum :

$$\frac{\partial \bar{U}}{\partial t} = 0 = -\frac{\partial \langle \bar{u}'\bar{w}' \rangle}{\partial z} - C_d L(z) \bar{U}^2 - \frac{1}{\rho} \frac{d \langle \bar{p} \rangle}{dx} + f \bar{V}$$

Reynolds Stress :

$$\frac{\partial \langle \bar{u}'\bar{w}' \rangle}{\partial t} = 0 = -\langle \bar{w}'^2 \rangle \frac{\partial \bar{U}}{\partial z} + 2 \frac{\partial}{\partial z} \left(q \lambda_1 \frac{\partial \langle \bar{u}'\bar{w}' \rangle}{\partial z} \right) - q \frac{\langle \bar{u}'\bar{w}' \rangle}{3 \lambda_2} + C_w q^2 \frac{\partial \bar{U}}{\partial z} + \frac{7}{10} \frac{g}{\Theta} \langle \bar{u}'\bar{\theta}' \rangle$$

Vertical Velocity Variance :

$$\frac{\partial \langle \bar{w}'^2 \rangle}{\partial t} = 0 = \frac{\partial}{\partial z} \left(3 q \lambda_1 \frac{\partial \langle \bar{w}'^2 \rangle}{\partial z} \right) - \frac{q}{3 \lambda_2} \left(\langle \bar{w}'^2 \rangle - \frac{q^2}{3} \right) - 2 \frac{q^3}{3 \lambda_3} + \frac{16}{10} \frac{g}{\Theta} \langle \bar{w}'\bar{\theta}' \rangle$$

Turbulent Kinetic Energy :

$$\begin{aligned} \frac{\partial (2e)}{\partial t} = 0 = -2 \langle \bar{u}'\bar{w}' \rangle \frac{\partial \bar{U}}{\partial z} + 2 C_d L(z) \bar{U}^3 + \frac{\partial}{\partial z} \left(q \lambda_1 \frac{\partial (2e)}{\partial z} \right) + \frac{\partial}{\partial z} \left(2 q \lambda_1 \frac{\partial \langle \bar{w}'^2 \rangle}{\partial z} \right) - 2 \frac{q^3}{\lambda_3} + 2 \frac{g}{\Theta} \langle \bar{w}'\bar{\theta}' \rangle \\ 2e = q \langle \bar{u}'^2 + \bar{v}'^2 + \bar{w}'^2 \rangle \end{aligned}$$

(121 a-d)

Note that the equation for horizontal velocity variance is not critical to the model, yet it appears implicitly in the equation for turbulent kinetic energy, in which form drag makes an appearance as a cubic term in mean velocity.

Passive and Active Scalar Transport

Taking the decomposition $\bar{\Theta} = \langle \bar{\Theta} \rangle + \bar{\Theta}''$ and spatially averaging over Equation 112 yields

$$\underbrace{\frac{\partial \langle \bar{\Theta} \rangle}{\partial t} + \langle \bar{u}_j \rangle \frac{\partial \langle \bar{\Theta} \rangle}{\partial x_j}}_I + \underbrace{\frac{\partial \langle \bar{\Theta}'' \bar{u}_j'' \rangle}{\partial x_j}}_{II} + \underbrace{\frac{\partial \langle \bar{u}_j'' \bar{\theta}'' \rangle}{\partial x_j}}_{III} = \kappa \frac{\partial^2 \langle \bar{\Theta} \rangle}{\partial x_j \partial x_j} + \kappa \left\langle \frac{\partial^2 \bar{\Theta}''}{\partial x_j \partial x_j} \right\rangle \quad (122)$$

Here, Term I is a dispersive flux which I neglect, Term II is the diffusion along the mean temperature gradient which, for this high Peclet-number flow, is negligible compared to turbulent diffusion. Term III represents a physiological source. In the model, Equation

YY simplifies to a balance between flux divergence and a source. The second moments of sensible heat are

$$\begin{aligned} & \frac{\partial \langle \overline{u_i' \theta'} \rangle}{\partial t} + \langle \overline{u_j} \rangle \frac{\partial \langle \overline{u_i' \theta'} \rangle}{\partial x_j} + \langle \overline{u_i' u_j'} \rangle \frac{\partial \langle \overline{\Theta} \rangle}{\partial x_j} + \langle \overline{u_j' \theta'} \rangle \frac{\partial \langle \overline{u_i} \rangle}{\partial x_j} - \beta_i \langle \overline{\theta'^2} \rangle = -\frac{1}{\rho} \overline{\theta'} \frac{\partial p'}{\partial x_i} - \frac{\partial \langle \overline{\theta' u_i' u_j'} \rangle}{\partial x_j} \\ & - (\nu + \kappa) \frac{\partial^2 \langle \overline{\theta' u_i'} \rangle}{\partial x_j \partial x_j} \end{aligned} \quad (123)$$

and

$$\frac{\partial \langle \overline{\theta'^2} \rangle}{\partial t} + \langle \overline{u_j} \rangle \frac{\partial \langle \overline{\theta'^2} \rangle}{\partial x_j} + \langle \overline{u_j' \theta'} \rangle \frac{\partial \langle \overline{\Theta} \rangle}{\partial x_j} = -\frac{\partial \langle \overline{\theta'^2 u_j} \rangle}{\partial x_j} \quad (124)$$

In the closure of the scalar moments used in this study, a simple one-band energy model was adopted. The scalar continuity and turbulent vertical flux equations are

$$\frac{\partial \langle \overline{c} \rangle}{\partial t} = -\frac{\partial \langle \overline{w' c'} \rangle}{\partial z} + S_c \quad (125)$$

$$\frac{\partial \langle \overline{w' c'} \rangle}{\partial t} = -\langle \overline{w'^2} \rangle \frac{\partial \langle \overline{c} \rangle}{\partial z} - \frac{\partial \langle \overline{w' w' c'} \rangle}{\partial z} - \overline{c'} \frac{\partial p'}{\partial z} \quad (126)$$

where S_c is a source (or sink) term arising from an integral average over a multiply-connected domain. As in the dynamic model, the quasi-Gaussian approximation is adopted for the quadruple velocity correlation and local down-gradient transport follows in the closure of scalar flux transport terms $\langle \overline{w' w' x'} \rangle$, e.g.:

$$\langle \overline{w' w' c'} \rangle = -q \lambda_1 \frac{\partial \langle \overline{w' c'} \rangle}{\partial z} \quad (127)$$

The pressure transport term is approximated as a destroyer of vertical flux:

$$\left\langle c' \frac{\partial p'}{\partial z} \right\rangle = C_4 \frac{\langle w' c' \rangle}{\tau} \quad (128)$$

where C_4 is a dimensionless coefficient. Since the passive scalar does not amplify or resist pressure perturbations, there is no redistribution of scalar flux among the component axes. Katul and Albertson (1999) pointed out that Equation 128 does not adequately represent the pressure-scalar covariance in the CBL because of the different timescales governing top-down and bottom-up diffusion (see Moeng and Wyngaard, 1989). By analogy, one would not expect Equation 128 to capture the twin timescales of ejections and sweeps in the canopy.

The turbulent flux equation can also be expressed as

$$\frac{\partial \langle w' c' \rangle}{\partial t} = A_1(z) \frac{\partial^2 \langle w' c' \rangle}{\partial z^2} + A_2(z) \frac{\partial \langle w' c' \rangle}{\partial z} + A_3(z) \langle w' c' \rangle - A_4(z) \quad (129)$$

$$A_1(z) = \frac{2\tau}{C_8 \langle w'^2 \rangle}$$

$$A_2(z) = \frac{\tau}{C_8} \frac{\partial \langle w'^2 \rangle}{\partial z} + 2 \frac{\partial}{\partial z} \left(\frac{\tau}{C_8 \langle w'^2 \rangle} \right)$$

$$A_3(z) = \frac{\partial}{\partial z} \left(\frac{\tau}{C_8} \frac{\partial \langle w'^2 \rangle}{\partial z} \right) - \frac{C_4}{\tau}$$

$$A_4(z) = \langle w'^2 \rangle \frac{\partial \langle \bar{c} \rangle}{\partial z} - \frac{\partial}{\partial z} \left(\tau \frac{\langle w'^3 \rangle}{C_8} \right) \frac{\partial \langle \bar{c} \rangle}{\partial z} - \left(\tau \frac{\langle w'^3 \rangle}{C_8} \right) \frac{\partial^2 \langle \bar{c} \rangle}{\partial z^2}$$

(130 a-d)

Given a mean concentration field, the above equations can be used to invert for a flux distribution. This method was used by Katul and Anderson (1999) and Katul (personal communication) has suggested using this method to infer the effect of biology on source distributions of CO_2 species. The source distribution implied by SiB's bulk assumption may be inverted using a uniform CO_2 species concentration; the measured concentrations

at four levels can be inverted and compared to discern the effects of physiology. This is an area of future work intended to bring this thesis to publication.

Numerical Methods

One challenge in engineering an Eulerian turbulence model is to find a physical solution to an overdetermined mathematical problem. The canopy domain is problematic because the neglect of certain terms, such as vertical advection, leave less room for exogenous information in the model. The mean momentum equation is a first-order ordinary differential equation, while the second moment equations are second-order in the second moments and first-order in mean momentum. In theory the whole set should be satisfied by three pieces of boundary information, yet we have four items with which to dispense: two observed upper boundary conditions in mean velocity and Reynolds stress, a vanishing mean velocity at the lowest grid point, and a Reynolds stress that is determined by von Karman surface layer scaling at the lowest grid point. Failure to adequately satisfy these conditions leads to discontinuities in mean velocity at the upper or lower boundary.

Previous workers engineered similar models by neglecting Coriolis and pressure gradient forces. Instead of allowing pressure gradients to force the mean wind, momentum was “forced” using the boundary conditions. In the absence of a driving pressure gradient force, Reynolds stress reached a constant value above the canopy. The lack of momentum flux divergence caused turbulent transport to vanish above the canopy. To remedy this, the gradient of Reynolds stress was smoothed in order to accomplish transport. This was a nonphysical solution to a problem caused by the absence of physical terms in the model. In the present model, the driving pressure gradient force and Coriolis force are balanced by momentum flux divergence above the canopy, and the smoothing is not applied. Finally, previous workers applied three pieces of information as boundary conditions to a dimensionless model. The dimensionless mean velocity U/u^* was integrated from the ground upwards and the friction velocity

remained implicit. Thus, there was no true disjoint between the calculated upper velocity value and the measured mean wind.

In this study, a dimensionless shadow model was created for the neutral buoyancy case, in which all dynamical variables were scaled by h and u^* . This model is similar to those of previous workers. The dimensionless mean velocity is integrated upward from the soil surface using the Reynolds stress equation. Reynolds stress is solved by multiplying the Reynolds stress equation by $2C_d A^2 u$ and taking the vertical derivative of the mean momentum equation, so that $d/dz (d\langle p \rangle / dx) = 0$ and the constant pressure gradient force is moot. The resulting neighbor equation is second order in Reynolds stress and results in a tridiagonal matrix. For testing purposes, a robust matrix solver replaced the Thomas algorithm, which is unstable under some circumstances. In the absence of Coriolis and pressure gradient forces, the gradient of Reynolds stress is smoothed. This shadow model is used as the initial guess in subsequent iterations of a fully physical, dimensional model.

For dimensional cases, the measured velocity at the top of the tower is used as a boundary condition. The friction velocity may be an exogenous measured variable or an endogenous calculated variable. Mean velocity is integrated downward using the Reynolds stress equation, while Reynolds stress is integrated upward using the mean momentum equation. Vertical velocity variance, total velocity variance, temperature variance, temperature-water vapor covariance, velocity-temperature covariance, and horizontal velocity variance are solved in their second-order linear ODEs using a generalized and robust LU decomposition and backsubstitution from Press et al. (1992). Mean temperature and water vapor are integrated in a fashion similar to mean velocity using the second-order ODE of vertical heat flux.

The dimensional model uses a staggered grid in which mean quantities are defined at layer centers, while second moments are defined at layer edges. All vertical derivatives are centered differences. Leaf area density is defined everywhere, while the

governing length scales are defined at the layer edges. The triple moment terms are defined at layer centers.

In order to prevent instability, all variable profiles are relaxed by taking a weighted average of the new, raw profile with that of the previous iteration. The result is a semi-implicit scheme in which each profile is recursively weighted in Fortran:

$$u(i)^{n+1} = \alpha u(i)^{n+1} + (1 - \alpha) u(i)^n$$

where the factor α varies between 0.1 and 0.9. Numerical instability was a critical problem in the development of the model.

For passive scalars, the scalar continuity equation is integrated using a four-part smoothing stencil to obtain a profile of vertical scalar flux. The vertical flux equation is posed as a linear, second-order ODE in $\langle \overline{w'c'} \rangle$ and integrated for the mean scalar concentration. The scalar-temperature covariance is solved as a second-order linear ODE using the Thomas algorithm to iterate towards a steady-state solution. The gradient production terms in the scalar-temperature covariance equation form the inhomogeneous part of the equation. All vertical derivatives are centered differences. Each variable profile is then relaxed by a factor that varies from 0.9 to 0.1. When the absolute difference in mean scalar concentration falls below a critical value, the solution has converged.

Local Free Convection, Similarity, and Boundary Conditions

Monin and Obukhov's (1954) similarity theory yielded empirical evidence that only the height z , the buoyancy parameter $\beta=g/T$, the surface heat flux H , and the surface shear stress τ are needed to describe surface wind and scalar fields. Dually defined frictional and convective scales follow from this assumption:

$$\begin{aligned}
\text{velocity:} \quad u_* &= (\tau / \rho)^{1/2}; \quad u_f = \left(z \frac{g}{T} \frac{H}{\rho C_p} \right)^{1/2} \\
\text{temperature:} \quad T_* &= -\frac{H}{\rho C_p u_*}; \quad T_f = \left[\frac{T}{gz} \left(\frac{H}{\rho C_p} \right)^2 \right]^{1/2} \\
\text{length:} \quad z; \quad L &= \frac{-u_*^3 T \rho C_p}{kgH}
\end{aligned} \tag{131}$$

where ρ is a constant air density, C_p the specific heat at constant pressure and k is Von-Karman's constant. In truth one only has four independent scales and four parameters, since

$$\begin{aligned}
u_f / u_* &\propto (-z / L)^{1/3} \\
T_f / T_* &\propto (-z / L)^{-1/3}
\end{aligned} \tag{132}$$

As H becomes large and the surface stress vanishes, as it does in free convection (positive H ; $-z/L \rightarrow \infty$), only one velocity scale remains. Thus near the ground ($z/L \ll 1$), one should find perturbations of order u_* and T_* ; aloft ($z/L \ll -1$), one should find free convection behavior with perturbations of order u_f and T_f . Monin and Obukhov (1954) suggested that surface layer behavior at $-z/L \gg 1$ is like that in free convection. This became known as “local free convection.”

The challenge here is to relate second-order scalar and wind moments to mean properties at the upper and lower boundaries of the domain. Previous workers in micrometeorology have used local free convection (Pyles et al. 2000, Meyers and Paw U 1987). While I am not comfortable with these assumptions at the values of $-z/L$ found in real canopies, I found no better alternative. After reviewing the literature, I settled on forms similar to those used by Pyles et al. (2000), with different limiting values for the shape of second order wind moments under neutral conditions. My discussion of local free convection closely follows that of Wyngaard et al. (1971).

The dimensionless gradients of mean temperature and wind are important to the second moments. The non-dimensional temperature gradient, for example, is

$$\frac{kz}{T_*} \frac{\partial \Theta}{\partial z} = \phi_h(z/L) \quad (133)$$

No dimensionless Π group may be formed from u_f , T_f , and z ; instead, the dimensionless gradient is required to be constant under local free convection:

$$\frac{kz}{T_f} \frac{\partial \Theta}{\partial z} = \text{constant} \quad (134)$$

Using the relationship of T_f to T_* , we find that

$$\frac{kz}{T_*} \frac{\partial \Theta}{\partial z} \propto (-z/L)^{-1/3} \quad (135)$$

According to Wyngaard et al. (1971), observations show a $-1/2$ power law and the prediction of local free convection has not been validated. The empirical form of the dimensionless temperature gradient is (Wyngaard et al. 1971):

$$\begin{aligned} \phi_h &= 0.74 + 4.7 \frac{z}{L}, & 0 \leq \frac{z}{L} \\ \phi_h &= 0.74 \left(1 - 9 \frac{z}{L} \right)^{-1/2}, & 0 \geq \frac{z}{L} \end{aligned} \quad (136)$$

The dimensionless wind shear and its empirical form are

$$\begin{aligned} \frac{kz}{u_*} \frac{\partial U}{\partial z} &= \phi_m \\ \phi_m &= 1 + 4.7 \frac{z}{L}, & 0 \leq \frac{z}{L} \\ \phi_m &= \left(1 - 15 \frac{z}{L} \right)^{-1/2}, & 0 \geq \frac{z}{L} \end{aligned} \quad (137)$$

Armed with these forms, one can predict the behavior of $\overline{u\theta}$ under unstable conditions. Under free convection, $\overline{u\theta} \propto u_f T_f$ and the constant of proportionality is just zero. To see how $\overline{u\theta}$ approaches zero, consider that $\overline{u\theta}$ is created by $\partial U / \partial z$ and

$\partial\Theta/\partial z$, and will change sign as they change sign. Wyngaard et al. (1971) hypothesized that

$$\frac{\overline{u\theta}}{\frac{\partial U}{\partial z} \frac{\partial \Theta}{\partial z}} \propto z^2 \quad (138)$$

The authors then divided by $\overline{w\theta}$ and made use of surface layer scales:

$$-\frac{\overline{u\theta}}{\overline{w\theta}} = a_2 \phi_m \phi_h \quad (139)$$

which yielded a good match to the data for $a_2=5$. The local free convection prediction for temperature variance is

$$\frac{(\overline{\theta^2})^{1/2}}{T_f} = \text{constant} \quad (140)$$

I followed Pyles et al. (2000) in using the empirical form

$$\frac{\overline{\theta^2}}{T_*} = 4 \left(1 - 8.3 \frac{z}{L} \right)^{-2/3} \quad (141)$$

The empirical and predicted forms of $\overline{\theta^2}$ agree over the entire unstable range. The vertical velocity variance is also successful, and follows from similar arguments, i.e.

$$\begin{aligned} \frac{(\overline{w'^2})^{1/2}}{u_f} &= \text{constant} \\ \frac{(\overline{w'^2})^{1/2}}{u_*} &1.5 \left(1 - 2.2 \frac{z}{L} \right)^{1/3} \end{aligned} \quad (142)$$

Each of the empirical relationships can be thought of as a hybrid forced convection relationship, with an implicit dependence on both u_* and u_f , which approaches the limit of free convection as $-z/L$ becomes large. Similar relationships for the horizontal velocity variances are far less certain. I found some hope in Hicks (1985), who suggested additive

mechanical and buoyant contributions from u_* and w_* . I modified the shape of the horizontal variances to reflect the measurements of Shaw et al. (1974):

$$\begin{aligned}\frac{\overline{(u'^2)}}{u_*^2} &= 3.5 + 0.35 \frac{w_*^2}{u_*^2} \\ \frac{\overline{(v'^2)}}{u_*^2} &= 1.5 + 0.35 \frac{w_*^2}{u_*^2}\end{aligned}\tag{143}$$

Scalar boundary conditions in the second moments used hybrid forms derived from the forms for temperature variance and velocity-temperature covariance. For the mean scalar boundary condition, several possibilities were considered. For example, the ratio of scalar variance to mean CO_2 concentration measured within the domain could be used as a measure of scalar “intensity” and extended to the top of the domain. The variance of a tracer could be determined from similarity theory and a mean concentration backed out from these estimations at the top of the domain. The problem with this approach is that the tower top is located in the roughness sublayer, where similarity rules do not apply. In the end, I settled for an internal boundary condition at the canopy top, integrating upward and downward in the tracer model to the boundaries of the domain. Various other forms of estimating boundary conditions may become useful when I consider component tracers such as top-down and bottom-up tracers.

Physiological Scaling

In order to distribute the source terms of CO_2 and its isotopic species with height in the canopy, an implicit physiological scaling model was needed. I faced several choices in the selection of a physiological model. One option was to engineer a fully interactive, vertically resolved model with coupled energy budget and biogeochemical modules. This option was set aside for doctoral work. For this thesis, some components of physics or physiology would be prescribed or forced, and the Simple Biosphere Model (SiB2) was the obvious candidate to provide the forcing. One option was to couple a prognostic tracer transport model to a biogeochemical model at every height and force the system using components of the energy balance derived from SiB2. A simpler

approach was to distribute bulk photosynthetic fluxes of each CO₂ species calculated by SiB2 as source terms within the canopy. The same scaling assumptions that allow integration of canopy assimilation in SiB2 could be used to distribute fluxes over leaf area in a vertically resolved model. Lastly, the soil respiration model in SiB2 could be used to provide lower boundary fluxes of each passive tracer.

The Collatz et al. (1991) model of C3 photosynthesis describes the leaf assimilation (or gross photosynthetic) rate as the minimum of three limiting rates:

$$A \leq \text{Min}(w_c, w_e, w_s) \quad (144)$$

where w_c reflects the efficiency of the photosynthetic enzyme system (Rubisco-limited), w_e the amount of PAR captured by the leaf chlorophyll, and w_s the capacity of the leaf to export or utilize the products of photosynthesis. The physiological limit on assimilation w_c ($\mu\text{mol}/\text{m}^2/\text{s}$) depends on the biochemical processing capacity of the leaf:

$$w_c = V_m \left[\frac{C_i - \Gamma^*}{C_i + K_c (1 + O_2 / K_o)} \right] \quad (145)$$

where

V_m = maximum catalytic capacity of Rubisco ($\mu\text{mol}/\text{m}^2/\text{s}$)

C_i = concentration of CO₂ in the leaf interior (Pa)

O_2 = partial pressure of O₂ in leaf interior (Pa)

Γ^* = CO₂ compensation point (Pa)

K_c = Michaelis-Menten constant for CO₂ (Pa)

K_o = inhibition constant for O₂ (Pa)

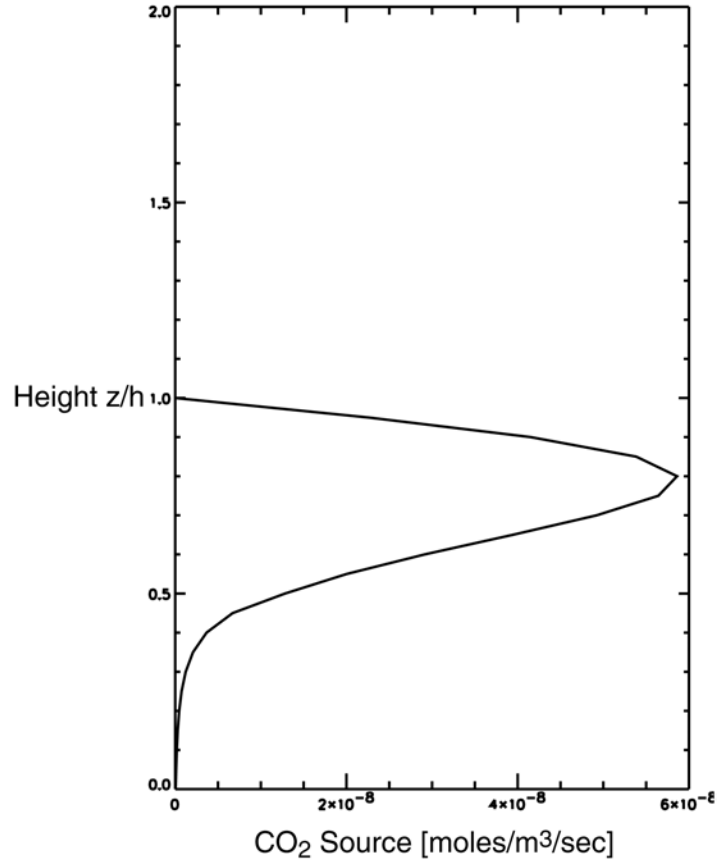


Figure 12. Example source distribution of CO₂.

The parameter V_m is given as the product of V_{\max} , the maximum photosynthetic capacity of Rubisco and a temperature-dependent function. The light-limited rate of assimilation w_e is

$$w_e = (\overline{F} \cdot \overline{n}) \varepsilon (1 - w_v) \left[\frac{C_i - \Gamma^*}{C_i + 2\Gamma^*} \right] \quad (146)$$

where w_v is the leaf-scattering coefficient for PAR, ε is the quantum efficiency for CO₂ uptake ($\mu\text{mol}/\mu\text{mol}$ or $\mu\text{mol}/\text{J}$), and $\overline{F} \cdot \overline{n}$ is the normally incident solar flux. Collatz et al. (1991) defined a third limiting rate, the capacity for export or utilization of products of photosynthesis:

$$w_s = \frac{V_m}{2} \quad (147)$$

Nature smooths the transition between limiting photosynthetic rates, and Collatz et al. (1991) represented this smoothing using two quadratic equations with coupling coefficients θ and β :

$$\begin{aligned}\theta w_p^2 - w_p(w_c + w_e) + w_e w_c &= 0 \\ \beta A^2 - A(w_p + w_s) + w_p w_s &= 0\end{aligned}\tag{148}$$

where A is the assimilation rate. So, w_p , the smoothed photosynthetic modifier, is expressed as

$$w_p = \left[\frac{(a_o + b_o) - \sqrt{(a_o + b_o)^2 - 4\theta a_o b_o}}{2\theta} \right]\tag{149}$$

The coupling coefficients θ and β range from 0 (full coupling) to 1, and are typically found to be $\sim 0.8-0.99$. The net assimilation is then $A_n = A - R_d$, where $R_d = 0.015V_m$.

Leaf physiological properties are thought to vary in response to the time-mean, radiation-weighted distribution of photosynthetically active radiation (PAR). The PAR-flux vertical component is assumed to attenuate with depth in the canopy according to the semi-empirical expression of Goudriaan (1977):

$$F_L = F_0 e^{-kL}\tag{150}$$

where F_L is the PAR flux at leaf area index L in the canopy, F_0 is the PAR flux above the canopy, L is the cumulative leaf area index, and k is the extinction coefficient.

First, the bulk photosynthetic flux of CO_2 was distributed with depth according to the distribution of PAR. Local variations in CO_2 concentration and the microclimate energy balance were ignored. Next, bulk fluxes of the following three isotopic species were distributed in the same way: $^{12}C^{16}O^{16}O$, $^{13}C^{16}O^{16}O$, and $^{12}C^{18}O^{16}O$. In the vertical distribution, discrimination was implicitly assumed constant with height. An example source distribution is shown in Figure 12.

One can imagine various distributions for the flux of ^{18}O : a weighting that depends on evaporative demand or leaf area density, for example. In future work, we may invert for weighted sums of various source distributions. For now, we only distribute fluxes with respect to assimilation. In further work, we will use this configuration to test our bulk assumptions about canopy physiology using an inversion suggested by Katul (pers. comm.)

Isotope Calculations

A complete pathway of additive discrimination for the carbon isotope is shown in Figure 15. The total transport of carbon through the leaf as modeled in SiB2 consists of four steps (Suits et al., in review):

1. Flow of CO_2 across the leaf boundary layer. For laminar flows, the theoretical calculation of discrimination is that of free-air diffusion to the $2/3$ power, that is $(1.044^{2/3} - 1)$ or 2.9 per mil.
2. Molecular diffusion through the stoma: 4.4 per mil.
3. Dissolution into mesophyll cell water. This is the equilibrium fractionation as CO_2 enters solution: 1.1 per mil.
4. Aqueous phase transport to the chloroplast. This is the discrimination associated with diffusion of dissolved CO_2 in water: 0.7 per mil.
5. Calculate carbon isotope ratio of the assimilated CO_2 flux.
6. Calculate the $\delta^{13}\text{C}$ of the canopy air space based on the carbon isotope ratios of respired CO_2 , assimilated CO_2 and CO_2 turbulently mixed within and into the canopy air from the overlying atmosphere.

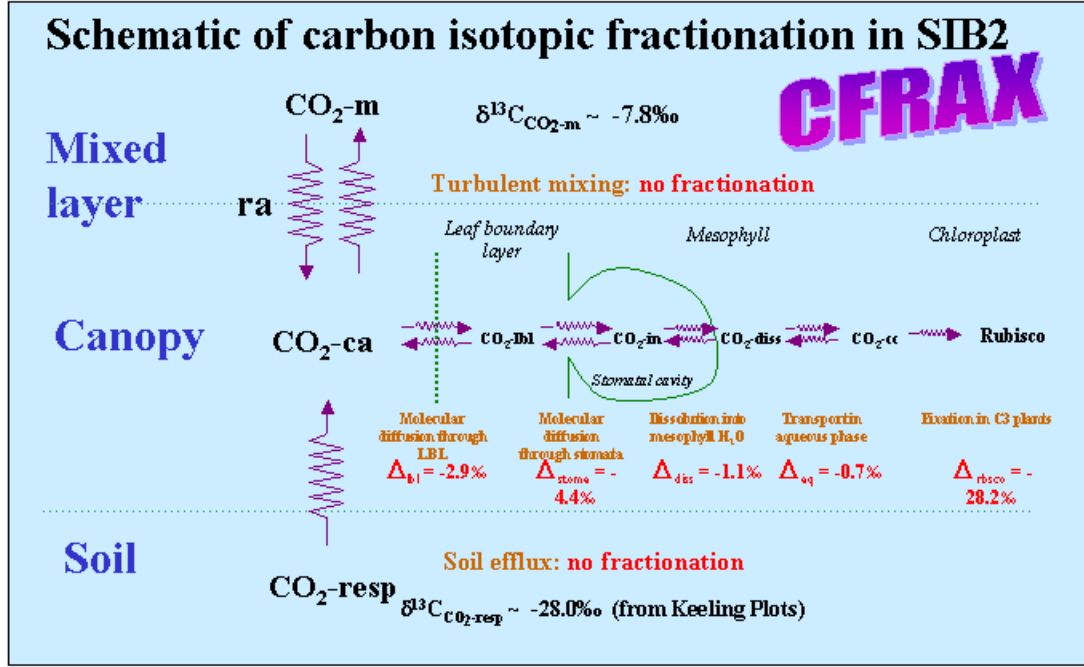


Figure 15. The pathway of carbon isotope discrimination in CFRAX, a submodule of SiB2. After Suits et al., in press.

The model of Suits et al. does not consider photorespiration explicitly, or it assumes that photorespiration fractionates exactly as assimilation. Net isotope fractionation in C3 plants is determined as follows (Suits et al., in review):

$$\Delta_{C3} = \Delta_S \frac{C_{ca}}{C_{ca}} + (\Delta_i - \Delta_S) \frac{C_s}{C_{ca}} + (\Delta_{diss} + \Delta_{aq} - \Delta_i) \frac{C_i}{C_{ca}} + (\Delta_{rbco} - \Delta_{diss} - \Delta_{aq}) \frac{C_c}{C_{ca}} \quad (151)$$

where Δ_S , Δ_i , Δ_{diss} , Δ_{aq} and Δ_{rbco} are kinetic isotope effects associated with transport through the leaf boundary layer, into the stomatal cavity, into solution, aqueous phase transport and fixation by rubisco, respectively, and C_{ca} , C_s , C_i and C_c are the corresponding CO₂ concentrations in the canopy, at the leaf surface, within the stomatal

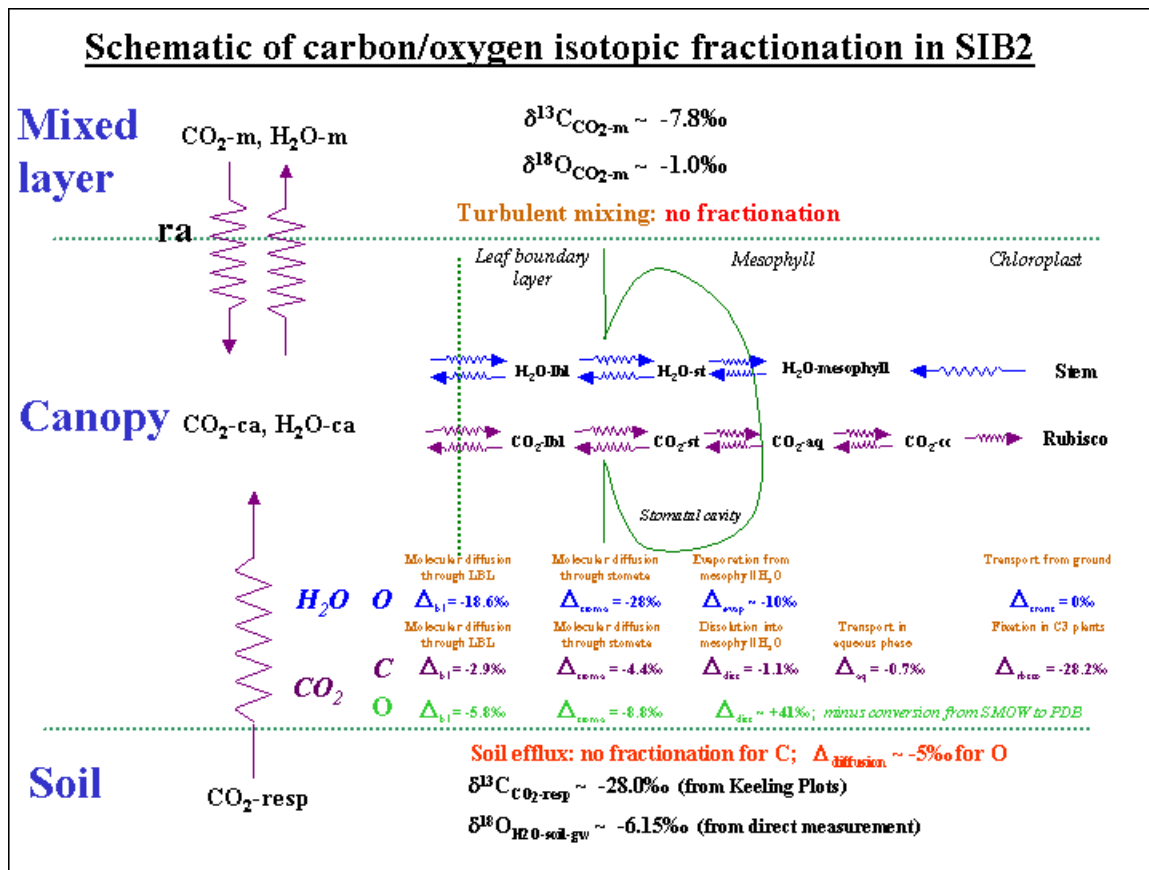


Figure 16. Pathways of oxygen isotope discrimination in SiB2. Courtesy of Dr. Neil Suits, Denning Research Group, Colorado State University.

cavity and chloroplast. Since the stepwise discriminations are approximately constant, differences in total discrimination are largely driven by changes in internal gradients of CO_2 concentration. Meanwhile, the calculation of the $\delta^{13}\text{C}$ composition of respired CO_2 simply assumes that no fractionation occurs during heterotrophic respiration. The age and composition of the soil carbon pool are fixed.

For the oxygen isotope calculations, the complete pathway is shown in Figure 16. The structure of oxygen isotope calculations is as follows:

1. Prescribe $\delta^{18}\text{O}$ of groundwater/stem H_2O vs SMOW.

2. Calculate equilibrium oxygen isotope fractionation between H₂O liquid and H₂O vapor in the leaf as a function of canopy temperature (Bottinga and Craig, 1969). This will tend to enrich $\delta^{18}\text{O}$ of liquid leaf water by about 10‰.
3. Calculate kinetic isotope effects (KIE) associated with molecular diffusive transport of water out of the leaf. This will tend to enrich the residual leaf water by an additional 10 to 15‰ during the peak of daily photosynthesis/transpiration (Dongmann et al., 1974; Förstel, 1978; Zundel, 1978; Flanagan et al. 1991a; Wang and Yakir, 2000). More transpiration means greater enrichment of the remaining leaf water, which then reacts and exchanges oxygen with CO₂.
4. Calculate $\delta^{18}\text{O}$ of internal H₂O vs SMOW (Baertschi, 1976).
5. Convert $\delta^{18}\text{O}$ of internal H₂O to PDB scale. This will reduce the apparent $\delta^{18}\text{O}$ of the water by about 41‰.
6. Calculate equilibrium oxygen isotope fractionation for CO₂⇌H₂O exchange (Bottinga and Craig, 1969; Brenninkmeijer et al. 1983). Heavy oxygen, i.e. ¹⁸O, will tend to move to the molecule in which the oxygen is most tightly bonded. In this case that is CO₂. This enriches the $\delta^{13}\text{C}$ of CO₂ by about 41‰, roughly canceling out the ‘effect’ of converting from SMOW to PDB.
7. Calculate kinetic isotope effects associated with molecular diffusive transport of CO₂ into the leaf (Craig and Gordon, 1965; Flanagan et al. 1991b, 1994, 1997). The net CO₂ flux is into the leaf. The enrichment of leaf water in ¹⁸O results in changes in the concentration gradients of ¹⁶O and ¹⁸O of CO₂ between the canopy and the mesophyll/chloroplast water. Specifically, it decreases the concentration gradient of ¹⁸O, while increasing the concentration gradient of ¹⁶O. This is how it enriches canopy CO₂ in ¹⁸O. The kinetic isotope effects of molecular diffusion will tend to work in the opposite direction, i.e., they will produce less fractionation of $\delta^{18}\text{O}$ of canopy CO₂, however, they are relatively small compared to the kinetic isotope effects imposed on leaf water, (compare KIEs of -5.8 and

-8.8 for CO₂ to -18.6 and -28 for H₂O).

8. Calculate oxygen isotope ratio of the assimilated CO₂ flux.
9. Calculate the $\delta^{18}\text{O}$ of the canopy air space based on the oxygen isotope ratios of respired CO₂, assimilated CO₂ and CO₂ turbulently mixed within and into the canopy air from the overlying atmosphere (same method as used for ¹³C in Suits et al., in review).

An important question that is yet to be determined is whether it is appropriate to assume complete equilibrium between mesophyll CO₂ and 'internal' H₂O (Walker et al., 1989; Yakir et al., 1994; Williams et al., 1996; Gillon and Yakir, 2000, 2001). Incomplete equilibration would tend to reduce the ¹⁸O enrichment of canopy CO₂.

The model of Suits et al. (in press) assumes that no fractionation is associated with heterotrophic respiration. In addition, soil CO₂ in solution is assumed to be in equilibrium with soil H₂O in the upper layers. Equilibration depends on the quantity and activity of carbonic anhydrase in the soil, which may exist in insufficient quantities for equilibration to occur. The diffusion of CO₂ out of the upper soil layers is associated with a -5 ‰ fractionation effect in ¹⁸O (i.e. a 5 ‰ depletion in respired CO₂). The $\delta^{18}\text{O}$ of soil water is calculated solely from that of ground water, with no meteoric input or temperature dependence. The fixed fractionation effects applied to the evaporative enrichment and diffusion of ¹⁸O are consistent with the model of Craig and Gordon (1965).

3.4 The Willow Creek Site

The Willow Creek Ameriflux tower site (latitude: 45° 48.47' N; longitude: 90° 04.72' W) is a mature and productive upland hardwood ecosystem. The species composition includes green ash (*Fraxinus pennsylvanica*), sugar maple (*Acer saccharum*), and basswood (*Tilia americana*). The canopy is approximately 24 meters tall with a leaf area of 4.2. The Willow Creek site is consistently more productive than its lowland neighbor, the WLEF Tall Tower in Park Falls, Wisconsin (Cook et al. 2002).



Figure 17 (a) Understory of the Willow Creek tower site.



Figure 17 (b) View from the Willow Creek flux tower.

As a best estimate, Willow Creek took up (-) $425 \text{ g C m}^{-2} \text{ yr}^{-1}$ during 2000, in contrast to the near annual carbon balance of the greater WLEF area, which released (+) $16 \text{ g C m}^{-2} \text{ yr}^{-1}$ in 1997 (Cook et al. 2002). The site is purposely situated in an area of little topography. Photos of the site are included in Figure 17.

The Willow Creek canopy has a closed architecture, yet time-averaged profiles of CO_2 isotope species in the canopy appear intermittently well-mixed. From the point of view of eddy-covariance, this is considered an asset, as eddy flux measurements should not have to be corrected for storage (Davis, personal communication). In practice, the Willow Creek flux tower is plagued by hours-long releases of respired air from surrounding lowlands under stable conditions, so that a storage correction is indeed necessary (Cook et al., 2002).

3.5 Measurement Methods

Micrometeorological Measurements

Full descriptions of the Willow Creek site and measurements taken there can be found at <http://cheas.psu.edu/wcreek.html> and <http://public.ornl.gov/ameriflux>.

The following basic measurements are taken continuously at Willow Creek:

- CO_2 and H_2O fluxes at 29.6m
- CO_2 mixing ratio profile (0.6, 1.5, 3.0, 7.6, 13.7, 21.3, and 29.6m)
- H_2O mixing ratio profile (2, 7.6, 12.2, 18.3, 24.4, and 29.6 m)
- Above canopy radiation (29.6 m)
 - Solar (incoming and reflected)
 - Infrared (incoming and emitted)
 - Photosynthetically active radiation (incoming direct and diffuse PAR)
- Below canopy radiation
 - Photosynthetically active radiation profile (2, 7.6, 12.2, and 18.3 m)
 - Net radiation above the forest floor (2 m)
- Air temperature profile (0.25, 0.5, 0.75, 1, 2, 7.6, 12.2, 18.3, 24.4, 29.6 m)

- Wind speed/direction profile (2, 12.2, 24.4, and 29.6 m)
- Soil temperature and soil moisture profile (surface, 5, 10, 20, 50, 100 cm)
- Soil heat flux (7.5 cm)
- Tree stem temperatures (maple, north and south facing)
- Leaf wetness indicator (29.6 m)
- Precipitation (rain and snow)

The frequency of measurements are as follows:

- 0.1 second – eddy covariance measurements (wind speed/direction, CO₂, H₂O)
- 1 second – radiation, air temperature, H₂O mixing ratio, barometric pressure
- 5 seconds – canopy PAR, net rad, wind speed/dir, air temperature/humidity
- 1 minute – incoming direct/diffuse PAR, leaf wetness
- 10 minutes – air/soil/tree temperatures, soil moisture, soil heat flux
- 21 minutes – interval between profile CO₂ measurements at a given level

Measurements of CO₂ mixing ratio using a LICOR 6251 are zeroed every 42 minutes and calibrated with standards every 4 hours. Measurements of CO₂ and H₂O flux using a LICOR 6262 are continuously calibrated with the LICOR 6251 (CO₂) and chilled mirror hygrometer measurements (H₂O). The CO₂ standards used are NOAA standards at 340, 440, and 550 ppm CO₂ in air.

Wind speed is measured using a CSI CSAT Sonic anemometer. Air temperature is measured using an RM Young 43347 RTD temperature probe (29.6 m), Type T thermocouples (0.25 to 2m), and CSI CS500 temperature and relative humidity probes. A Kipp and Zonan CNR1 net radiometer and CSI 100 ohm current shunt module are used above the canopy; LICOR Quantum sensors sense PAR elsewhere. Pressure is measured using a Vaisala PTB101B analog barometer. Humidity at 29.6 m is measured using an EdgeTech model 200 DewTrak humidity transmitter; CSI CS500 probes are used elsewhere. A CSI CR23X and CSI CR10X datalogger are linked to a Toshiba Libretto portable computer.

Plumbing at Willow Creek consists of Brailsford TD4x2NA double acting diaphragm pumps, 1/4" PFA or Dekabon 1300 tubing, and Gelman Acro 50 teflon inlet filters.

Field Methods for Daytime Isotopic Air Measurements

Given the intermittency of turbulence and the likelihood of sampling coherent, ramp-like structures, I decided to sample time-averages of isotopic composition using buffer volumes. The buffer volumes allowed me to average over the stochastic noise



Figure 18. Stable isotope canopy profiling system with buffer volumes.

contained in individual snapshots. Continuous air sampling would avoid the filtering effect of digital sampling. In addition, the buffer volumes would provide averages comparable to the Reynolds averaged terms in the governing equations. As discussed below, the Reynolds average and the buffer volume average are not entirely equivalent.

An example of my isotopic measurement system is pictured in Figure 18. The laboratories of Professor James Ehleringer and Professor Joseph Berry were instrumental in advising, developing the sampling design, and providing field support¹. In the figure, four buffer volumes (A) are in-line with Teflon filters (B), tubes of magnesium perchlorate (MgCl_2) used as a dessicant (C), 100 mL flasks (D), and pumps (E) which, in this case, flow at a rate of 0.6-0.8 L/min. The buffer volumes are sealed with Teflon tape. O-rings protect the connection between each component, and metal spurs may be used to forge permanent connections in the outdoors. Each flask opens and closes with two stopcocks sealed with O-rings.

In the field, the downstream stopcock is typically closed first to ensure an adequate sample of air. The Ehleringer lab evacuates and bakes the flasks shown in Figure 18 in order to remove moisture and trace organic material; the Berry lab does not evacuate or bake their flasks. Each flask is flushed for an approximate residence time (usually 3 minutes) before a sample is taken; the buffer volumes are typically flushed for 15 or 20 minutes while sealed and in-line. In the sampling system pictured here, two flasks are flushed at a time. The lines are broken and re-sealed between each run. An entire profile of four levels takes approximately an hour. In other configurations, we are able to flush all four flasks at once using a four-way manifold and sample two profiles per hour. Care is taken to avoid the development of a vacuum in the lines: at Willow Creek, where the Teflon filters are located at the inlets on the tower, we observed that low pressure develops in the lines due to the resistance of the filters.

From the tower to the sample system, air is drawn through tubing (Dekoron 1300; 0.625 cm outer diameter; Aurora, Ohio, USA). Lines are placed quasi-logarithmically with height, at levels already used for the ongoing measurement of CO_2 profiles at Willow Creek. In damp weather, these lines are typically backflushed before sampling begins; between visits to the site, the lines are sealed. While the two sampling systems (the on-site eddy-flux system and the Berry lab's mass spectroscopy system) use the

¹ Professor James Ehleringer, Department of Biology, University of Utah, Salt Lake City, Utah. Professor Joseph Berry, Carnegie Institute of Washington, Stanford University, Palo Alto, California. See

same NOAA standards, they were not calibrated to one another. The canopy profiles used in storage calculations in eddy-covariance applications are typically allowed to drift, since only relative changes in CO₂ storage and relative eddy fluxes are significant: the system at Willow Creek is unusual in its use of NOAA standards every 4 hours.

Local anthropogenic influences are a serious concern. The concentration footprint of a flux tower is larger than its flux footprint and is largest at night, when static stability allows air parcels to travel long distances before they are sampled by the measurement system. The sampling system is placed a reasonable distance away from the tower and disturbances are generally avoided. A statistical test in which the lowest measurement level is discarded and the slope or intercept of a Keeling plot is tested for significant change may reveal human influence (see “Nighttime and Daytime Keeling Plots” below).

The buffer volumes shown in Figure 18 were selected to have a residence time of ~ 20 minutes at a flow rate of about 1 L/min. The residence time model was tested in the Berry lab, using reservoirs of a standard CO₂ mixture and CO₂-free air. A sampling transform was derived in which the molar quantity lost downstream is proportional to the richness of the mixture:

$$dn_r = -\alpha n_r dt \quad \text{or} \quad dr = \frac{dn_r}{n_{total}} = -\alpha r dt \quad (152)$$

$$\alpha = \frac{1}{V} \frac{dV}{dt}$$

where n_r is the number of moles, n_{total} is the constant molar capacity of the volume, r is a molar mixing ratio, V is the fixed volume of the container, and dV/dt is the pumping rate.

Why does this matter? It matters because this sample is not truly an average. In order to compare this transformed sample of air to a modeled Reynolds average, I want to

Acknowledgements for details.

know if apples are apples. It also matters to the post-hoc calibration of the two measurement systems, which is important to later work. For example, I can use our profile measurements to calculate total ecosystem discrimination, if the two measurement systems are properly calibrated (Lloyd et al. 1996). If $\delta^{13}\text{C}$ and CO_2 are well correlated during the day, I can also calculate the flux of ^{13}C (Bowling et al. 1999).

Integration of Equation 152 yields:

$$n_r(t) = n_r(t=0) \exp(-\alpha t) \quad (153)$$

The decay equation applied separately to each batch of air that enters the volume from the upstream line. The molar amount of a single discrete batch is

$$\begin{aligned} \delta n_r &= r_{line} \frac{dn_{mixture}}{dt} \delta t = r_{line} \frac{d(PV/RT)}{dt} \delta t \\ &= r_{line} \frac{P}{RT} \frac{dV}{dt} \delta t \end{aligned} \quad (154)$$

where $\frac{dn_{mixture}}{dt}$ is the molar flow rate through the line, P is pressure, T is temperature, R is the universal gas constant, and the ideal gas law has been used. Based on scale analysis, we may ignore the contribution of $n_{mixture} \frac{dr_{line}}{dt}$ to $\frac{dn_r}{dt}$. The contribution of this batch to the molar mixing ratio is

$$\frac{\delta n_r}{n_{total}} = \frac{\delta n_r}{(PV/RT)} = r_{line} \frac{1}{V} \frac{dV}{dt} \delta t = r_{line} \alpha \delta t \quad (155)$$

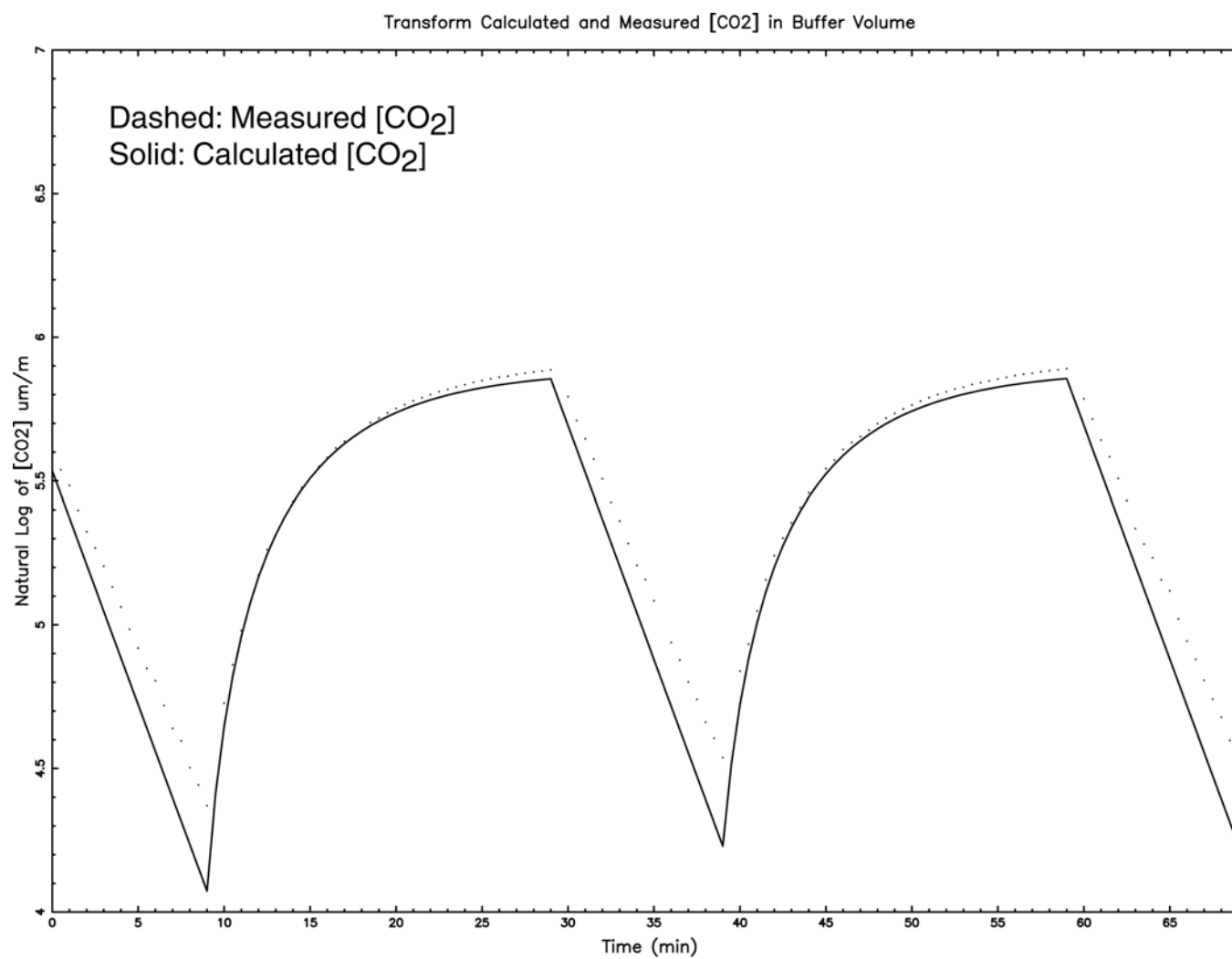


Figure 19. Measured and calculated in-line concentrations of CO₂ using a buffer volume.

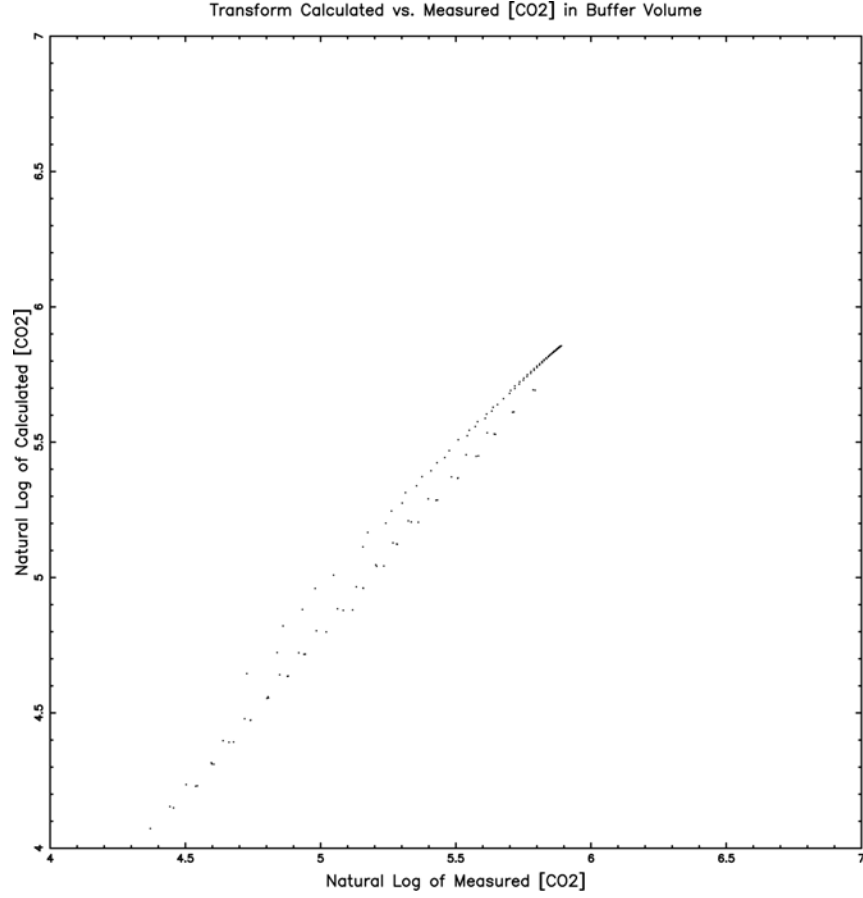


Figure 20. Comparison of measured and calculated CO₂ concentrations using a buffer volume.

The independent decay of this batch is

$$\frac{\delta n_r(t)}{n_{total}} = r_{line}(t=0)\alpha \exp(-\alpha t) \quad (156)$$

If we sum over many contributions, we have

$$r_{volume}(t) = \sum_{i=0}^{N-1} r_{line}(t=i\Delta t)\alpha \exp(-\alpha(t-i\Delta t))\Delta t \quad (157)$$

where $r_{volume}(t)$ is the mixing ratio of tracer in the buffer volume and $N = \frac{T}{\Delta t}$ is the number of contributions. The exact integral is an exponential transform in which

information about $r_{line}(t)$ accrues over the residence interval T and is expressed in $r_{volume}(t)$:

$$r_{volume}(t) = \alpha \exp(-\alpha t) \int_{t'}^t r_{line}(t') \exp(\alpha t') dt' \quad (158)$$

Lastly, we include the decay of tracer initially found in the line and distinguish solutions for $t \leq T$ and $t > T$.

for $t \leq T$:

$$r_{volume}(t) = r_{volume}(t=0) \exp(-\alpha t) + \alpha \exp(-\alpha t) \int_0^t r_{line}(t') \exp(\alpha t') dt' \quad (159)$$

for $t > T$:

$$r_{volume}(t) = r_{volume}(t-T) \exp(-\alpha T) + \alpha \exp(-\alpha t) \int_{t-T}^t r_{line}(t') \exp(\alpha t') dt'$$

Now we have a sampling transform. The proper residence time T follows from the decay function:

$$T = -\ln \left(\frac{r_{volume}(t)}{r_{volume}(t=0)} \right) \frac{1}{\alpha} \quad (160)$$

The transform model was tested very successfully at the Berry lab, using a portable infra-red gas analyzer (IRGA). The experimental setup is shown in Figure 21. A step function of ordinary air (at 20-minute intervals) and CO₂-free air (at 10-minute intervals) was passed through a flow meter before entering the buffer volume. After leaving the volume, a tiny flow of air was diverted to the IRGA using a valve. The diverted flow passed through another flow meter before entering the sample port of the IRGA. A comparison of measured and calculated CO₂ concentrations is shown in Figures 19 and 20. The offset between the two may be caused by uncertainty in the measured flow rate. The instrument flow meters were known to be inaccurate; the “true” flow rate was measured using a highly sophisticated soap-bubble method.

Nighttime and Daytime Keeling Plots

A powerful method of inferring the isotopic composition of a source is a plot of $1/[CO_2]$ vs. δ , known as a Keeling plot. The intercept of the Keeling plot, in the limit that $[CO_2]$ approaches infinity, is a valid description of the respiratory apparent source under various conditions. For the simple nighttime case in which respiration does not discriminate, a simple two-reservoir mixing model devised by Keeling (1958; 1961) reveals the isotopic composition of CO_2 respired by the whole forest system:

$$\delta_f = \frac{[CO_2]_a}{[CO_2]_f}(\delta_a - \delta_r) + \delta_r \quad (161)$$

where δ_f is the isotope ratio of forest air, δ_a is the isotope ratio of air above the forest, and δ_r is the isotope ratio of respired air. Knowing the composition of respired air, one can estimate total ecosystem discrimination.

In the presence of a distributed source with varying discrimination, some of the assumptions surrounding Keeling plots break down: under poorly stratified daytime conditions, I found a non-linear curve in place of a functional linear relationship. From mass conservation, a daytime expression similar to Equation 161 can be derived:

$$[CO_2]_f = [CO_2]_a - [CO_2]_p + [CO_2]_s \quad (162)$$

$$\delta_f [CO_2]_f = \delta_a [CO_2]_a - \delta_p [CO_2]_p + \delta_s [CO_2]_s$$

$$\delta_f = \frac{[CO_2]_a}{[CO_2]_f}(\delta_a - \delta_r) + \frac{[CO_2]_p}{[CO_2]_f}(\delta_r - \delta_p) + \delta_r$$

where $[CO_2]_p$ is the contribution of photosynthesis and δ_p is the isotopic composition of assimilated air. The intercept of the Keeling plot in the last equation above has a different physical meaning: under quasi-steady conditions, the middle term in the last equation contributes to the intercept and is a measure of isotopic disequilibrium. Under unsteady conditions, the intercept also tells us about the relative contribution of

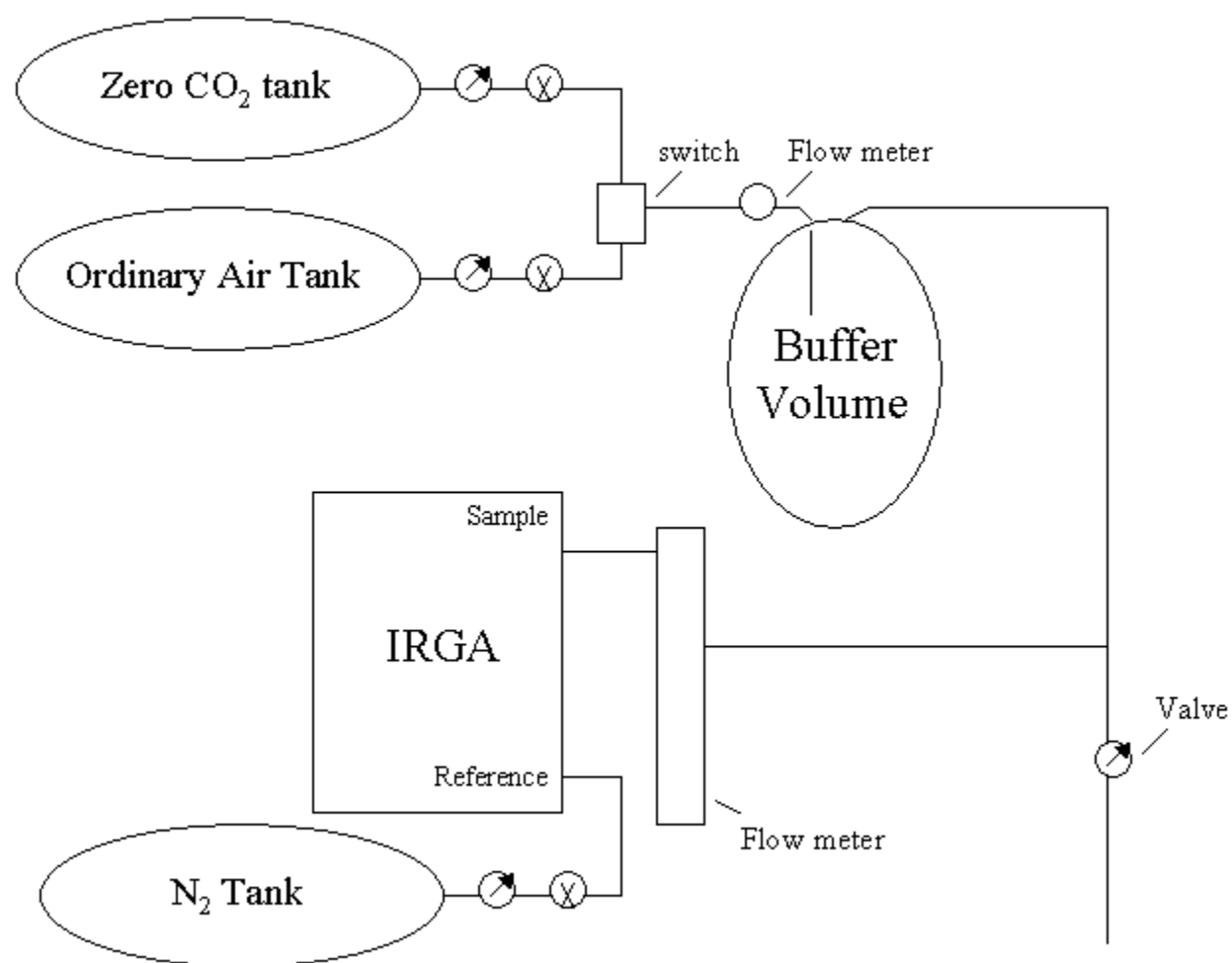


Figure 21. Laboratory schemata for the testing of a buffer volume.

photosynthesis to the CO₂ concentration of canopy air. The slope of the daytime Keeling plot provides information regarding the relative magnitude of turbulent mixing vs ecosystem exchange. This discussion goes against the grain of majority thinking: Keeling plots are thought to break down under conditions of multiple sources and turbulent daytime mixing. It is true that correlations are poor under unstratified conditions. Most workers are afraid of noise for very good reasons. However, subtle systematic differences between sites may offer insights into instantaneous isotopic disequilibrium and turbulent mixing. In a later section, we will explore whether these differences are measurable or significant at all.

Nighttime Keeling plots provided bounding conditions to the isotopic fractionation model of SiB2. A single Keeling plot typically uses 16 flasks, with samples taken at four levels. The protocol at the Ehleringer lab required sampling four levels, waiting one half hour, and then sampling again, etc. The flasks were flushed two at a time at alternate levels for three minutes. When possible, a portable LICOR gas analyzer was used to test for stratification in [CO₂] before isotopic sampling began.

The statistical model used for Keeling plots is one in which errors are accommodated in both δ and [CO₂]⁻¹. In this study, the methods of Press et al. (1992) were used to generalize the regression. The merit function becomes

$$\chi^2(a,b) = \sum_{i=1}^N \frac{(y_i - a - bx_i)^2}{\sigma_{yi}^2 + b^2 \sigma_{xi}^2} \quad (163)$$

where σ_{yi} and σ_{xi} are the standard deviations for the dependent and independent variables, respectively. This equation must be minimized with respect to a and b. Press et al. (1992) use a nonlinear iterative technique to minimize with respect to b, while solving exactly for a.

Isotopic Measurements of Soil, Water, Water Vapor, and Vegetation

When possible, leaf samples for leaf water (^{18}O) measurements were collected from three levels in the canopy: bottom, middle, and top. The “shotgun-removal” method was used in an attempt to randomly sample sunlit and shaded leaves. Stem water samples were also taken at three levels. Soil samples (for ^{18}O in soil water) were taken from 5-10 cm depth. Soil samples were taken in transects. All water samples were adequate for the collection of 0.5 mL of water; all samples were parafilm. Leaf water samples were refrigerated in the field, during shipment, and in the lab.

Water vapor measurements were taken in the field using a cold trap. Air was drawn slowly through Dekoron tubing from four levels on the tower to the cold trap. Sets of glass pipettes (a small pipette within a larger one) were placed in a cold bath of dry ice and alcohol in a metal deware. A T-fitting, sealed with O-rings, was used to close the pathway. Moist air flowed through the Dekoron tubing and into the pipettes, where water was trapped, and then out to the pump. Small flow rates were used to avoid aspirating ice particles. A single sampling run took approximately 20-25 minutes. After sampling, the pipettes were sliced or broken and sealed with parafilm. One concern was presence of dry ice at the field site during flask sampling. Dry ice was often kept in a closed container at the margins (one hoped) of the concentration footprint. Human influence was also potentially greater for water vapor than for CO_2 . For this reason, I stayed out of the footprint completely during water vapor sampling.

3.6 Methods of Model-Data Synthesis

One aspect of the experimental design presented in Figure 11 remains. The Eulerian closure model and SiB2 are dually driven by observations of mean wind, mean temperature, dewpoint temperature, visible and infrared downwelling radiation, pressure, and precipitation. The Eulerian model is dynamically driven by observations and physiologically driven by SiB2. Scaled source distributions of each isotopic species of CO_2 , as well as soil respiratory boundary sources, are provided to the Eulerian model by SiB2.

The driving data must be physically modeled in order to diagnose the appropriate quantities and fill missing data. For the month of each field campaign, a continuous data set of forcing variables was created to drive SiB2.

The following raw Willow Creek data were extracted: temperature, relative humidity, and wind speed at 24.4 m; incoming solar and infrared radiation at 29.6 m; and pressure. Raw WLEF data consisted of temperature, relative humidity, and wind speed at 30 m; pressure; and PAR. The WLEF data were then converted to SiB2 driver variables. Photosynthetically active radiation was converted to downwelling shortwave radiation using a factor of 0.45. Longwave emissivity was calculated using the following equation:

$$\varepsilon = 0.70 + \left(5.95 \times 10^{-5} e_{vap} \exp\left(\frac{1500}{T_{396m}}\right) \right) \quad (164)$$

where e_{vap} is the vapor pressure and T_{396m} is the temperature at the top of the WLEF tall tower. Downwelling longwave radiation was then calculated using the Stefan-Boltzmann Law: $\sim \varepsilon \sigma T_{396m}^4$. Vapor pressure was calculated from measured relative humidity as

$$\begin{aligned} e_{vap} &= e_{sat} \frac{RH}{100} \\ e_{sat} &= 6.11 \exp\left(\frac{L_v}{R_v} \left(\frac{1}{273} - \frac{1}{T_{396m}}\right)\right) \end{aligned} \quad (165)$$

where RH is relative humidity, e_{sat} is the saturation vapor pressure, L_v is the latent heat of vaporization and R_v is the gas constant for water vapor.

A continuous set of SiB2 driver data was constructed using the following steps:

1. Contemporaneous WLEF raw data and Willow Creek raw data were averaged to half-hourly values.
2. Half-hourly averages were set to missing if they exceeded certain physical limits (250 K < temp < 350 K; 250 K < dew point < 350 K; 0 m/s < wind speed < 50

m/s; $90000 \text{ kPa} < \text{pressure} < 10000 \text{ kPa}$; $200 \text{ W/m}^2 < \text{longwave} < 500 \text{ W/m}^2$; $20 \text{ W/m}^2 < \text{shortwave} < 1200 \text{ W/m}^2$; $0 \text{ mm} < \text{precipitation} < 20 \text{ mm}$).

3. Precipitation data from the NCDC cooperative observing network at Rhineland, WI were substituted for the Willow Creek precipitation data.
4. Willow Creek raw data were binned with and regressed on WLEF half-hourly averages.
5. Linear regressions using data from the WLEF tall tower were used to substitute for areas of missing driver data at Willow Creek. Downwelling longwave and shortwave radiation were forced to fit through the origin.
6. WLEF climatological values were interpolated to half-hourly values.
7. Where both Willow Creek and WLEF data were missing, climatology was substituted from previous years.

In order to allow soil temperature and moisture profiles to reach equilibrium, SiB2 was spun up using 5 years of WLEF data constructed by Dr. Niall Hanan at CSU's Natural Resource Ecology Laboratory. The model spin-up used 10-minute time steps and a six-layer soil model, and was driven hourly from 122 m.

5

The Walker Branch Case

5.1 The Neutral Shadow Model

The statistically stationary flow field for the most idealized case is shown in Figure 22. The mean velocity field displays a characteristic inflexion across the canopy top, which drives dynamical instability. Notably absent is a secondary wind maximum that would suggest countergradient momentum transport. As will be discussed below, this model is theoretically capable of such transport.

In the profile of Reynolds stress, we may divide the canopy layer into two regimes: a lower layer of no momentum flux divergence and correspondingly little form drag ($0 < z/h < 0.5$), and an upper layer of large momentum flux divergence and large work against form drag ($0.5 < z/h < 1$). In cases of horizontal heterogeneity, the lower layer is one in which streamwise advection is balanced by form drag. As discussed in the Methods section, this model does not account for gradients of Reynolds stress above the canopy. To achieve turbulent transport of Reynolds stress, a smoothing calculation is applied to the momentum flux divergence. As will be seen below, most model profiles are smoother than measured profiles.

In the profiles of vertical velocity variance ($\langle w'^2 \rangle$) and TKE ($1/2 q^2$), the same two regimes are evident. In the lower layer of the canopy, in the limit that gradients of variance disappear, the governing equation for vertical variance suggests that pressure transport is balanced by dissipation:

$$\frac{q}{3\lambda_2} \left(\left\langle \overline{w'^2} \right\rangle - \frac{q^2}{3} \right) \approx -\frac{2}{3} \frac{q^3}{\lambda_3} \quad (166)$$

In the equation for TKE, the same balance applies, as shear production and form drag both diminish in the lower canopy. This does not suggest equilibrium, nor does it suggest a regime dominated by turbulent transport. Instead, it is a regime of low energy in which some energy is introduced by turbulent transport, redistributed among the three components of variance, and dissipated isotropically. In the upper layer of the canopy, all terms in the variance equations are important.

In the budget of TKE, local equilibrium (production \propto dissipation) only applies in the inertial sublayer above the canopy. Shear production is greatest at the canopy top. Wake production, a weighted combination of the 3rd power of velocity and the leaf area, is greatest in the upper canopy. Transport carries energy from the region of

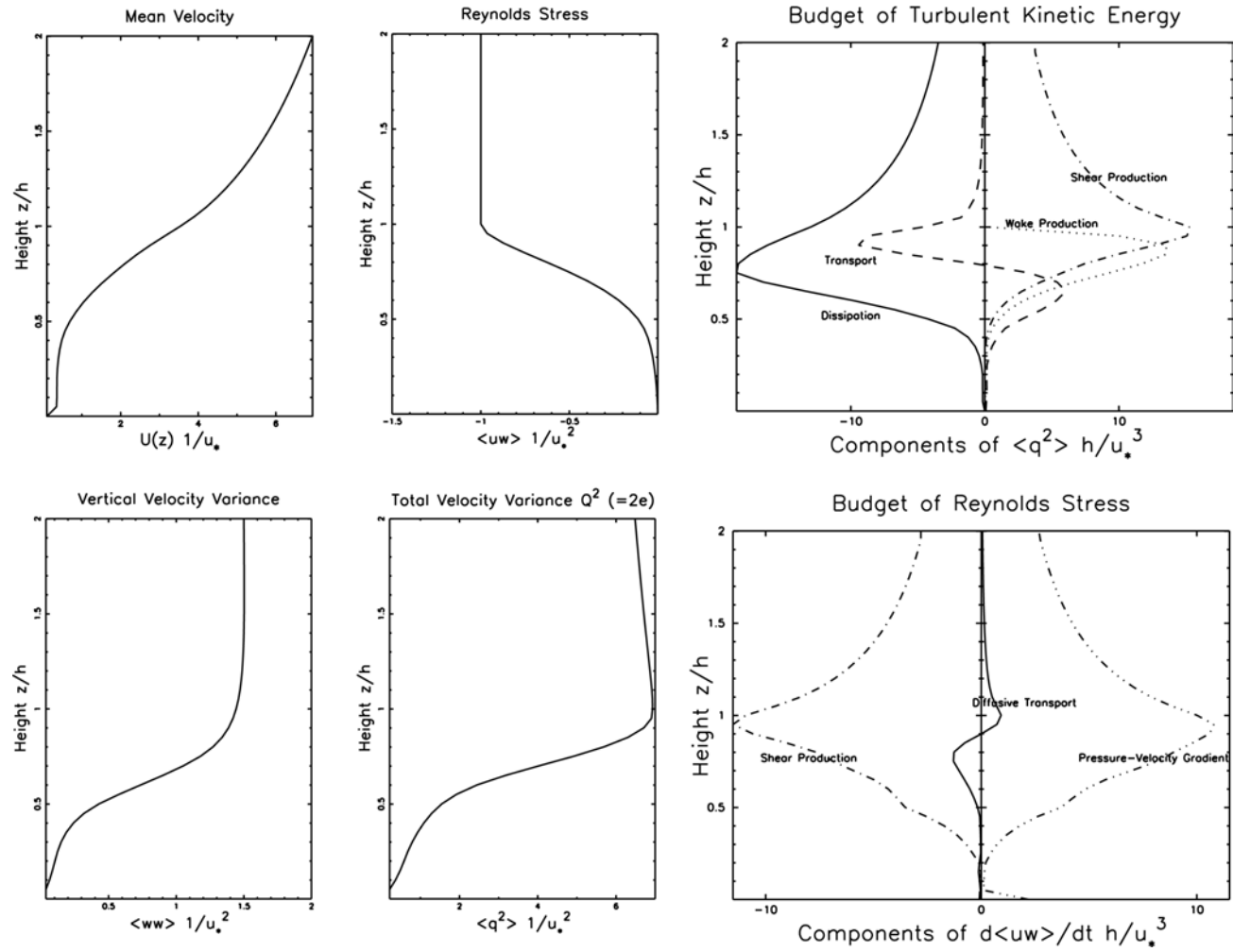


Figure 22. The neutral dynamics of a dimensionless shadow model. Clockwise from upper left: (a) The dimensionless mean velocity U/u_* , whose shear is a measure of inverse viscosity; (b) The normalized Reynolds stress $\langle u'w' \rangle / u_*^2$; (c) The budget of a squared velocity scale, or twice the turbulent kinetic energy ($q^2 = 2 \cdot \text{TKE}$); (d) The normalized vertical velocity variance $\langle w'^2 \rangle$; (e) The velocity scale q^2 ; (f) The budget of Reynolds stress $\langle u'w' \rangle / u_*^2$.

greatest production (both shear and wake forms) to an area in which dissipation exceeds production. Of course, pressure transport does not arise in the budget of total energy.

The budget of Reynolds stress generally shows that shear production is balanced by pressure transport:

$$\left\langle \overline{w'^2} \right\rangle \frac{d\overline{U}}{dz} \approx C_w q^2 \frac{d\overline{U}}{dz} - \frac{q \left\langle \overline{u'w'} \right\rangle}{3\lambda_2} \quad (167)$$

Diffusive transport is a sink of Reynolds stress in the upper canopy and a source above the canopy.

These regimes suggest simplifications to the full physics model that may be applied to future versions of SiB. The canopy could be approximated using an upper and lower regime, in which flux divergences are neglected in the lower canopy and the turbulent transport of Reynolds stress is also neglected. Although these approximations may distort the physics, they are still superior to the assumption of first-order closure.

5.2 The Walker Branch Case

The shadow model of a dimensionless, neutral canopy was tested using data by Baldocchi and Meyers that represent daytime conditions at Walker Branch. In this closed canopy, over 75% of the leaf area is in the upper 25% of the canopy. For this reason, Walker Branch carries distinct profiles compared to the “family portrait” of Raupach. It operates more like a tropical forest (Baldocchi, pers. comm.; Kruijt, 2000). Walker Branch is therefore a very challenging daytime case to pose to this model.

A full suite of model-data comparisons are shown in Figure 23. Quantitatively, the comparisons of mean wind and Reynolds stress are within reason. The convergence of Reynolds stress reflects the model assumption of symmetric leaf area: it is generally overestimated throughout the lower 75% of the canopy depth. In the data, a region of negative curvature in $\langle u'w' \rangle$ vs. z/h roughly co-occurs with a reversal in the gradient of the mean wind. Such a secondary wind maximum is possible

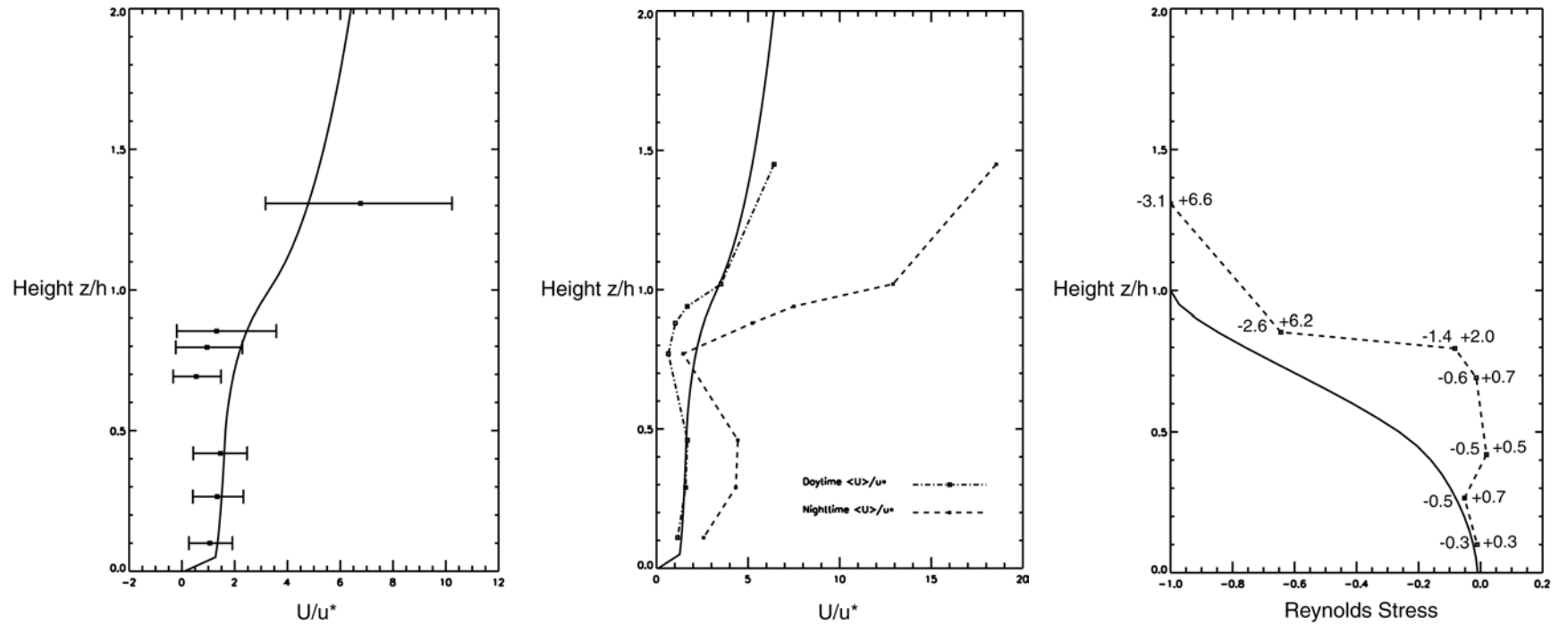


Figure 23. Comparison of neutral model output to the Walker Branch data of Baldocchi and Meyers. From left to right: (a) Normalized mean velocity; (b) Daytime and nighttime data (dash-dot and dashed, respectively) and model (solid line); (c) Normalized Reynolds stress data (dashed line) and model (solid line). The first standard deviation is a multiple of the Reynolds stress at a reference height: it is “absolute” as plotted here. The standard deviations of Reynolds stress data are listed to the left and right of the data points. As shown, measured Reynolds stress has an extremely high variance.

in the context of second-order closure in the governing equation for shear stress (Shaw, 1977):

$$\frac{\partial \langle u'w' \rangle}{\partial t} = 0 = \underbrace{-\langle w'^2 \rangle \frac{\partial \bar{U}}{\partial z}}_I - \underbrace{\frac{\partial \langle u'w'w' \rangle}{\partial z}}_{II} + \underbrace{\overline{p' \left(\frac{\partial u'}{\partial z} + \frac{\partial w'}{\partial x'} \right)}}_{III} \quad (168)$$

All that is necessary for a reversal in the mean wind gradient is that Term II oppose and exceed Term III. In the model, the curvature of $\langle u'w' \rangle$, along with gradients in $q(z)$ and $\lambda(z)$, determine turbulent transport. While the model is theoretically capable of producing a secondary wind maximum, in practice the model is stiff and secondary maxima are weak. One possible explanation for this stiffness is the smoothing of the gradient of Reynolds stress that occurs everywhere in the domain during the calculation of mean velocity. The deficit in turbulent transport is felt, through the neighbor equations, in the entire profiles of U and $\langle u'w' \rangle$.

Daytime and nighttime profiles of mean velocity suggest that the canopy is relatively inviscid at night. The flow sustains a strong internal inflection relative to the turbulent transfer of momentum, measured as Reynolds stress. It makes sense that static stability would damp turbulent shear stress at night, resulting in higher values of U/u^* everywhere in the canopy.

For the comparison of horizontal and vertical velocity intensities, an experiment was conducted in which leaf area profiles were varied among five cases: the symmetric case used in Figure 22, a top-heavy or closed canopy, a bottom-heavy or open canopy, a uniform canopy, and one with a very high center of mass and an open understory which might best approximate Walker Branch. Dimensionless profiles of leaf area density and λ are shown in Figure 24. The comparison of turbulence intensity σ_u/U is troublesome in every case (Figure 25). The authors of the data report significant run-to-run variability in profiles of intensity. The near-symmetry of modeled intensity about the canopy middle was a robust result that was nearly independent of canopy structure, with the exception of the high mass case. Given the apparent insensitivity of intensity to form drag, we must look to other terms in the governing equation for horizontal variance:

$$0 = \underbrace{-2\langle u'w' \rangle \frac{\partial \bar{U}}{\partial z}}_I + \underbrace{\frac{\partial}{\partial z} \left(q\lambda_1 \frac{\partial \langle u'^2 \rangle}{\partial z} \right)}_{II} + \underbrace{2C_d A \bar{U}^3}_{III} - \underbrace{\frac{q}{3\lambda_2} \left(\langle u'^2 \rangle - \frac{q^2}{3} \right)}_{IV} - \underbrace{\frac{2}{3} \frac{q^3}{\lambda_3}}_V \quad (169)$$

The overestimation of absolute Reynolds stress everywhere in the canopy causes Term I to be somewhat too large, but that can't be sufficient explanation. Another clue is the dissipation, which is isotropically distributed among the velocity variances. In both the model and the data, U is aligned with the direction of the mean wind and $\langle u'^2 \rangle$ is the largest of the velocity variances. One would expect $\langle u'^2 \rangle$ to also have the largest dissipation. The answer could also lie in the diffusivity $q\lambda_1$. In the profile of absolute horizontal variance (not shown), there is little curvature in $\langle u'^2 \rangle$ within the canopy, leaving turbulent transport to be accomplished by gradients in $\langle u'^2 \rangle$, $q(z)$ and $\lambda(z)$.

The normalized vertical velocity scale σ_w/U is a measure of vertical turbulence intensity (Figure 26). As the center of mass in the canopy is raised, the center of σ_w/U also rises, but does not approach that of the data. In the relatively extreme case of a high mass and an open understory, the normalized variance decreases everywhere in the canopy. The effects of anisotropy in the real canopy may account for these differences. The anisotropic orientation of leafs surely affects the distribution of dissipation. As with the calculations of horizontal variance, I have assumed an isotropic distribution of dissipation. Our poor understanding of the duality of dissipation in the canopy, which motivates the use of a length scale, is likely the root cause of these differences. Meanwhile, artifacts in σ_u/U and σ_w/U near the soil surface are a result of the prescription of anisotropy there. As shown in Figure 22, profiles of dimensionless $\langle u'^2 \rangle/u^*$ and $\langle w'^2 \rangle/u^*$ do not show similar artifacts.

An alternative explanation of the profiles in σ_w/U is that the upper canopy (where the majority of leaf area lies at Walker Branch) is more viscous than the model. This is consistent with reports of shifts to smaller length scales in a tropical canopy with similar structure (Kruijt, 2000). Smaller length scales correspond to lower diffusivity in the diffusive transport of vertical variance. The measured profiles are indeed less smooth

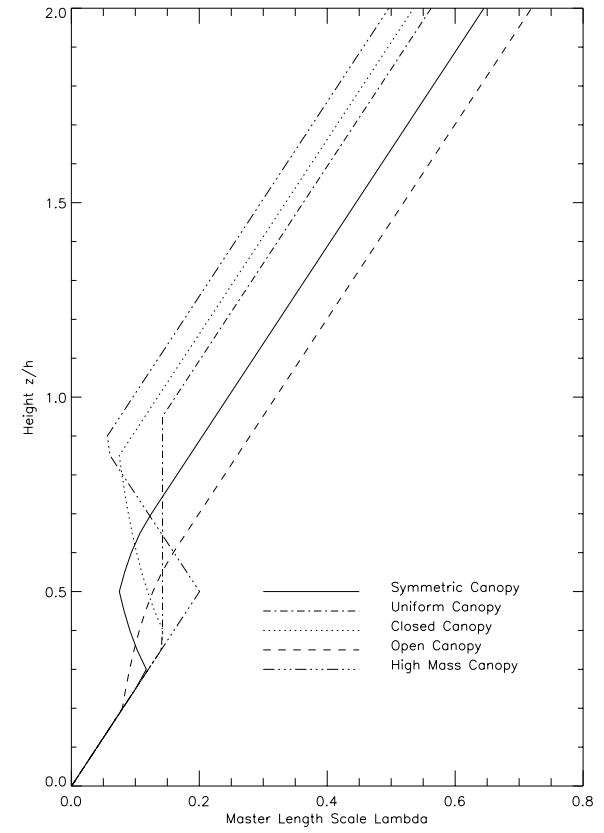
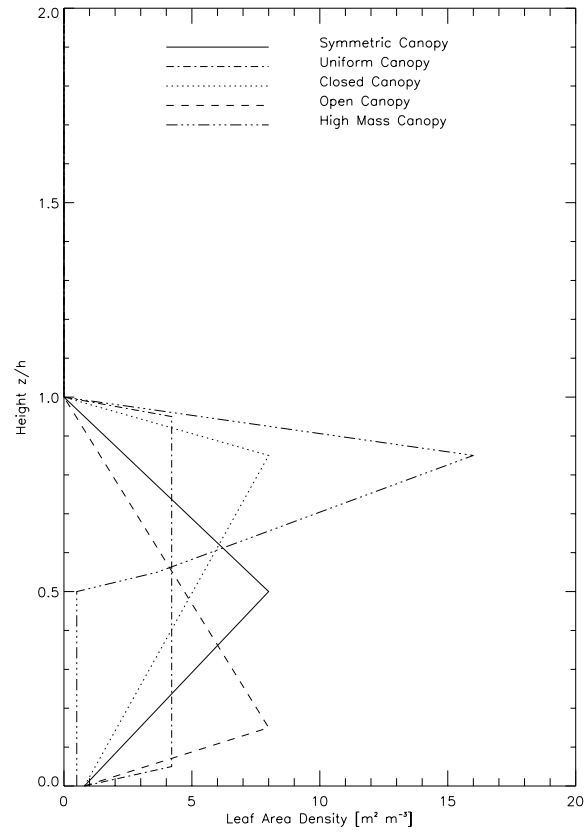


Figure 24. Profiles of dimensionless leaf area density and master length scale λ for four cases of canopy structure: a symmetric canopy, a uniform canopy, a closed canopy, an open canopy, and an extremely top-heavy canopy that most resembles Walker Branch.

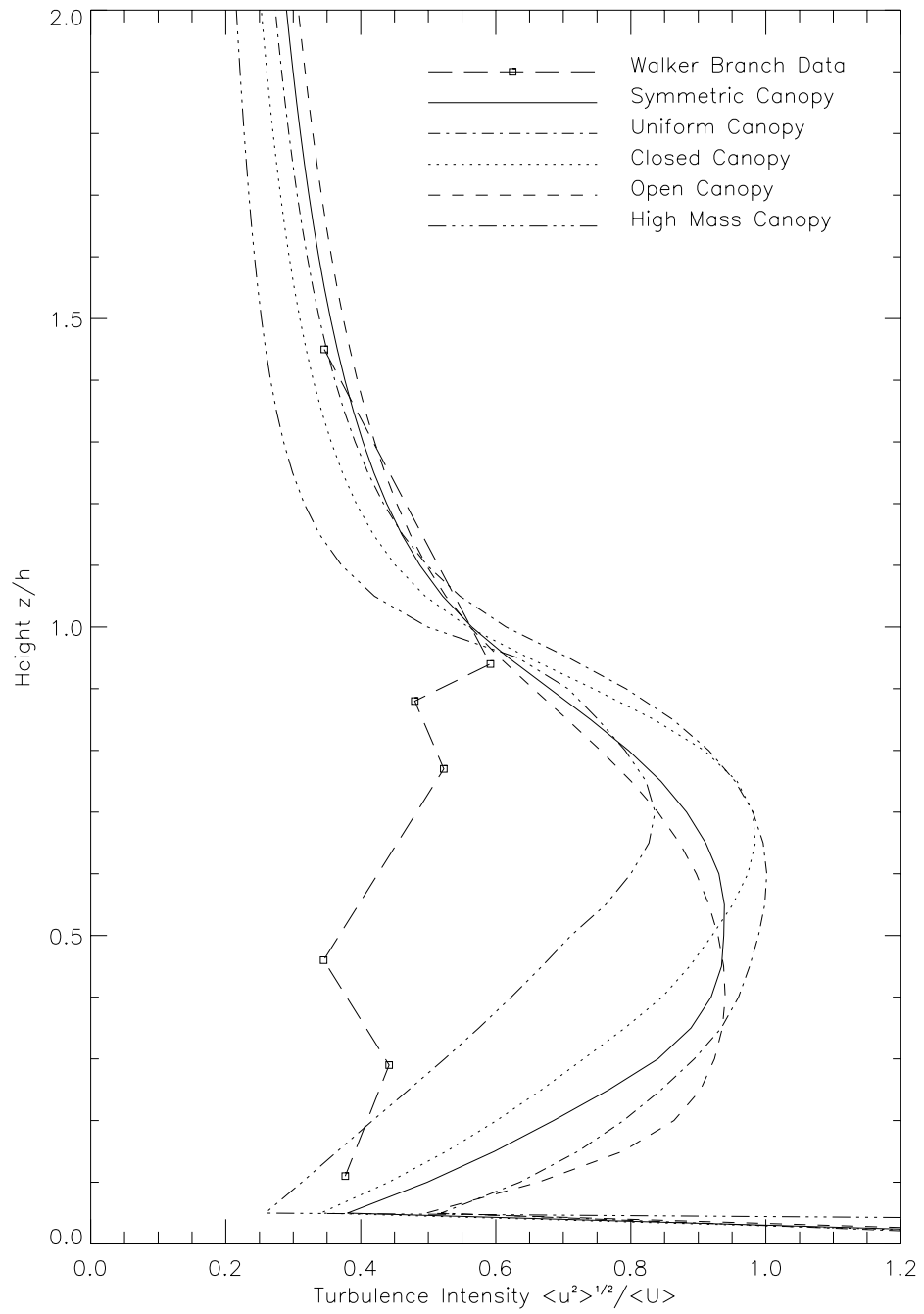


Figure 25. Measured and modeled profiles of turbulence intensity $\langle u'^2 \rangle^{1/2} / \langle U \rangle$ for the five cases presented in Figure 24.

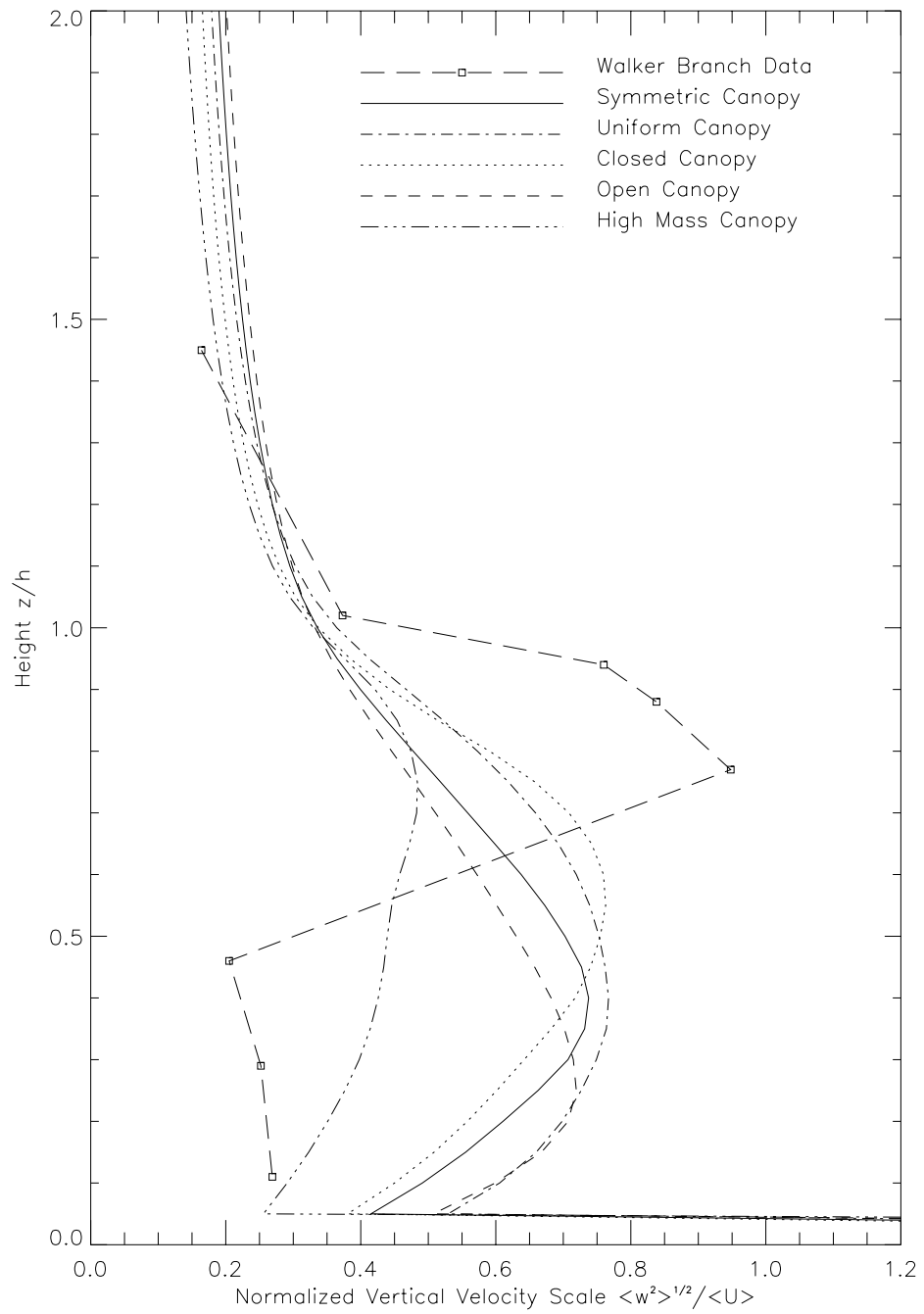


Figure 26. Measured and modeled profiles of normalized vertical velocity deviation $\langle w'^2 \rangle^{1/2}/U$ for the five cases presented in Figure 24.

than the modeled profiles, showing a deficit of σ_w/U within and an abundance aloft. However, the profile of horizontal turbulence intensity at Walker Branch does not corroborate this explanation.

The measured profiles of skewness in both u' and w' are consistent with the plane mixing layer analogy (Figure 27). Both profiles generally increase with height to the canopy top. Above the canopy, Sk_u decreases as expected, while Sk_w continues to increase. The co-occurrence of positive skewness in u' and negative skewness in w' suggests that sweeping motions (downward gusts of quickly moving air) dominate the flow regime within the canopy. The presence of Sk_u also implies horizontal heterogeneity in the real canopy. Recall, our variation of the closure for $\langle u'^3 \rangle$ looks something like this:

$$\langle \overline{u'u'u'} \rangle = -3q\lambda_1 \frac{\partial \langle \overline{u'u'} \rangle}{\partial x} \quad (170)$$

If the mean and transient components of the flow are both non-divergent, it follows that the horizontal divergence of $\langle u'^2 \rangle$ must be balanced by other horizontal flux divergence terms and by advective terms in the transient flow:

$$\frac{\partial \langle \overline{u'u'} \rangle}{\partial x} = -\frac{\partial \langle \overline{u'v'} \rangle}{\partial y} + \overline{v' \frac{\partial u'}{\partial y}} - \frac{\partial \langle \overline{u'w'} \rangle}{\partial z} + \overline{w' \frac{\partial u'}{\partial z}} \quad (171)$$

So the presence of skewness in u' implies the presence of a two- or three-dimensional advective flow. This is a strong contrast to the one-dimensional, horizontally homogeneous model flow in which $\langle u'^3 \rangle$ does not exist.

The model-data comparison in Sk_w makes sense in the upper half of the canopy, but fails near the soil surface, where the model boundary condition is artificially prescribed to the anisotropy measured *above* the canopy. A stronger understanding of anisotropy near the soil surface, or a generalized boundary condition is needed to resolve this contrast. In the dimensional model, generalized lower boundary conditions of zero gradient are used for the second moments.

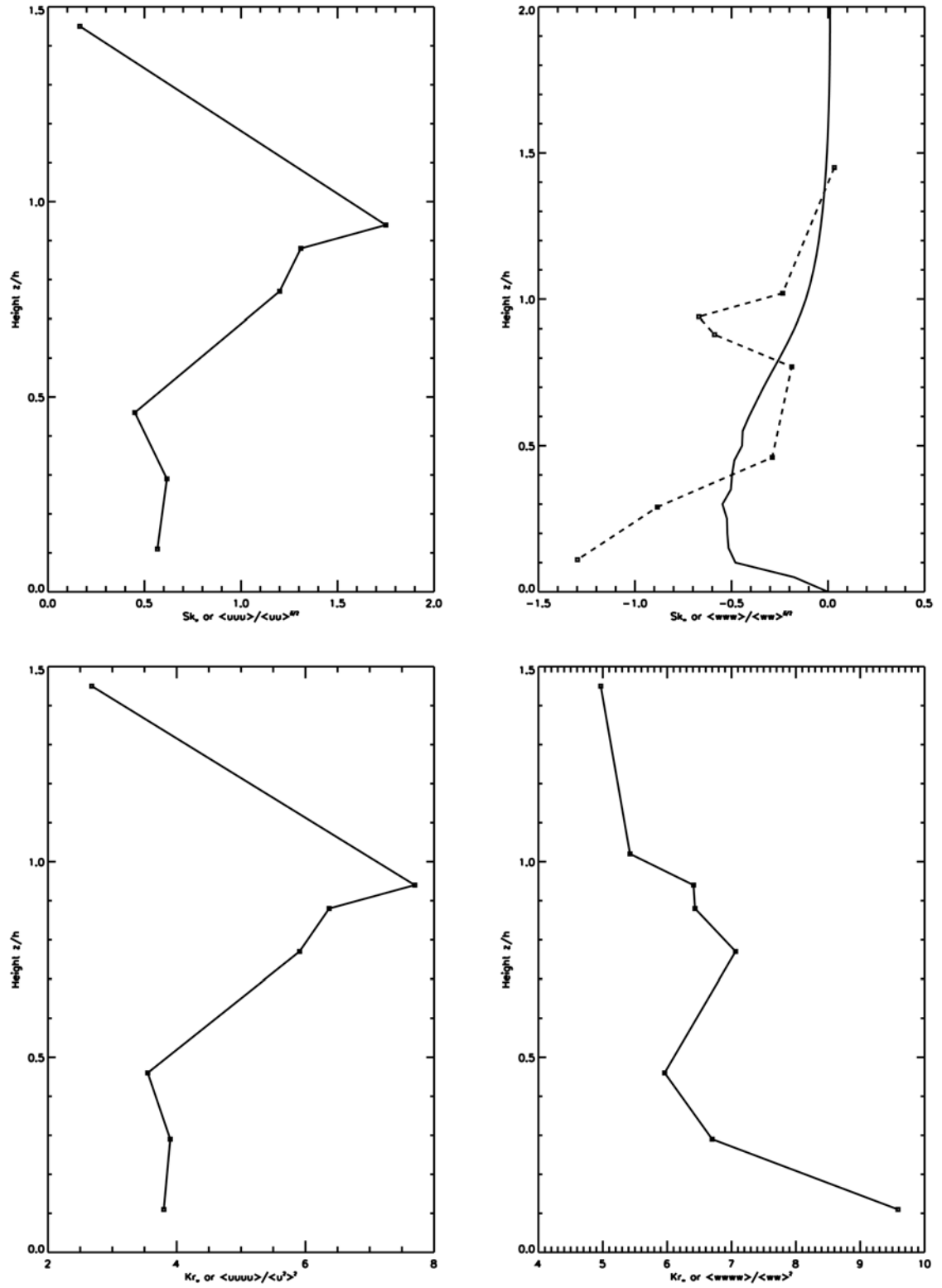


Figure 27. Clockwise from upper left: (a) Measured $Sk_u = \langle u'^3 \rangle / \langle u'^2 \rangle^{3/2}$; (b) Measured and modeled $Sk_w = \langle w'^3 \rangle / \langle w'^2 \rangle^{3/2}$; (c) Measured $Kr_u = \langle u'^4 \rangle / \langle u'^2 \rangle^2$; (d) Measured $Kr_w = \langle w'^4 \rangle / \langle w'^2 \rangle^2$.

Kurtosis is a measure of intermittency or peakedness in the velocity statistics. While I do not model fourth moments in the canopy, I do make a tacit assumption that velocity statistics are Gaussian, so that

$$\langle \overline{w'w'w'w'} \rangle = 3 \langle \overline{w'w'} \rangle \langle \overline{w'w'} \rangle \quad (172)$$

Deviations from a kurtosis of ~ 3 suggest that velocity statistics are non-Gaussian. While it makes sense that turbulence is more intermittent near the soil surface, where only the strongest gusts penetrate, I expected to find the same profile of intermittency in u' .

6

The Willow Creek Case

The component influences of soil, vegetation and the PBL on the isotopic composition of canopy air were modeled and measured. The immediate modeled transport compared well with time-dependent measurements of isotopic composition. However, the most enlightening contrasts were temporal differences in the dynamics of CO₂ transport and the systematics of isotope discrimination that were not captured by the model. By drilling down into the boundary conditions, ecological questions were revealed that can only be answered through time-dependent solutions to the governing equations of motion.

Isotopic signals in the canopy were fragile: in many cases, the canopy air space was so well mixed that there was almost no signal at all. When these canopy profiles are compared with contemporary isotopic samples of the PBL, it appears that signals of greater amplitude are found aloft on diurnal time scales. The motivation to scale from leaves to the PBL has in part become a search for stronger signals.

These results confirm the concept of two coupled and well-mixed “boxes” of canopy air, one “slow” or resistive reservoir near the soil surface and another “fast” or well-mixed reservoir aloft. Each reservoir is named for diffusion’s ability to iron out (or relax) tracer perturbations, as well as influence the efficiency of vertical communication. Thus the “slow” reservoir has larger storage relative to diffusive transport, while the “fast” reservoir has relatively less storage relative to diffusive transport. In the next generation of SiB, two-layer exchange between these two reservoirs will capture both the amplitude and the structure of these observed profiles. Differences in mixing aloft and

below suggest that the ecosystem flux of CO_2 does not equally sample respiratory and photosynthetic components in time. Inefficient communication between “slow” and “fast” reservoirs in the canopy may lead to natural biases in the flux footprint sampled by eddy covariance measurement systems.

The use of a single well-mixed canopy layer, such as in SiB, may lead to overestimates of the magnitude of soil heat fluxes. Soil fluxes should be governed by local scalar gradients and not by the bulk gradient of a mixed canopy. Likewise, the storage of respiratory contributions to NEE (Net Ecosystem Exchange) may be underestimated by SiB. Such a step forward would require new assumptions regarding local closure near the soil surface, where our understanding of canopy turbulence is still ambiguous (Raupach, personal communication).

6.1 Meteorological Contexts

Each canopy isotope profile was imbedded in the large-amplitude, large-scale diurnal cycle of the PBL. While internal model gradients of tracer composition were driven by sources and sinks, the bulk drawdown and isotopic enrichment of CO_2 was driven by measurements. Likewise, the model would have spun down dynamically in the absence of a pressure gradient were it not for the boundary condition in mean velocity and the second moments. Thus the driving conditions are important to the interpretation of these results. For all temporal changes, I look to the boundary conditions.

An examination of boundary layer dynamical forcing yields insight into the expected nature of the canopy response. Wind series are shown in Figures 28 through 31. Long periods of persistence in the forcing wind, punctuated by periods of rapid change, allow plenty of time for the canopy to relax and achieve near statistical stationarity. The flow in the PBL is obviously two-dimensional and may be three-dimensional, while we have made a one-dimensional approximation to the modulus of the mean velocity in the canopy. The very cases that are highly windy, advective and three dimensional in the PBL may be well-mixed and stationary in the canopy.

An example of the passage of a synoptic system is shown in Figure 28. Samples were taken at the nearby *Acer platanoides* site on both days. Overnight, a storm came through and cleansed the canopy and PBL of local ecological information. The soil respiratory signal in $\delta^{18}\text{O}$ of CO_2 was reset and would be evaporatively enriched in the days preceding the next synoptic event. For this reason, one does not directly compare boundary conditions or water composition measurements from the two June days.

6.2 Daytime Measured Profiles

Daytime profiles at a maple (*Acer platanoides*) site in the Chequamegon National Forest sampled in June, 2001, shown in Figure 32, have a temporal amplitude of equal order to their spatial amplitude. The influence of soil respiration, which is isotopically light, provides the strongest gradients near the soil surface. Photosynthesis causes a slight drawdown, isotopic enrichment and gradient reversal aloft. The same June profiles, viewed as a time series in Figure 33, show three discernable trends: component influences, opposing temporal trends in “slow” and “fast” reservoirs, and the establishment of photosynthetic gradients as the afternoon progresses. The near-soil reservoir stores more CO_2 , with a more depleted signature, as the afternoon progresses, while the canopy reservoir becomes drawn down and enriched until midafternoon, when gradients establish themselves. Thus there is a slight decoupling between the two reservoirs. One could say that the canopy reservoir lags the near-soil reservoir, but canopy mixing is not that slow.

Daytime profiles taken at Willow Creek in August, 2001 are shown in Figure 34. The maple stand, which possessed a vigorous understory, exhibited stronger gradients and greater drawdown and enrichment compared to the Willow Creek site. On these productive days in June and August, the maple stand exhibited over twice the storage change in the early afternoon (at the maple stand, $\Delta\text{CO}_2 = -9.3$ ppm, $\Delta\delta^{18}\text{O} = +2.7$ per mille, $\Delta\delta^{13}\text{C} = +0.38$ per mille; at the Willow Creek stand, $\Delta\text{CO}_2 = -4.3$ ppm, $\Delta\delta^{18}\text{O} = -.27$ per mille, $\Delta\delta^{13}\text{C} = +0.12$ per mille). Contrasting values of meteorological drivers and the canopy response as simulated by SiB for the two days are shown in Table BB.

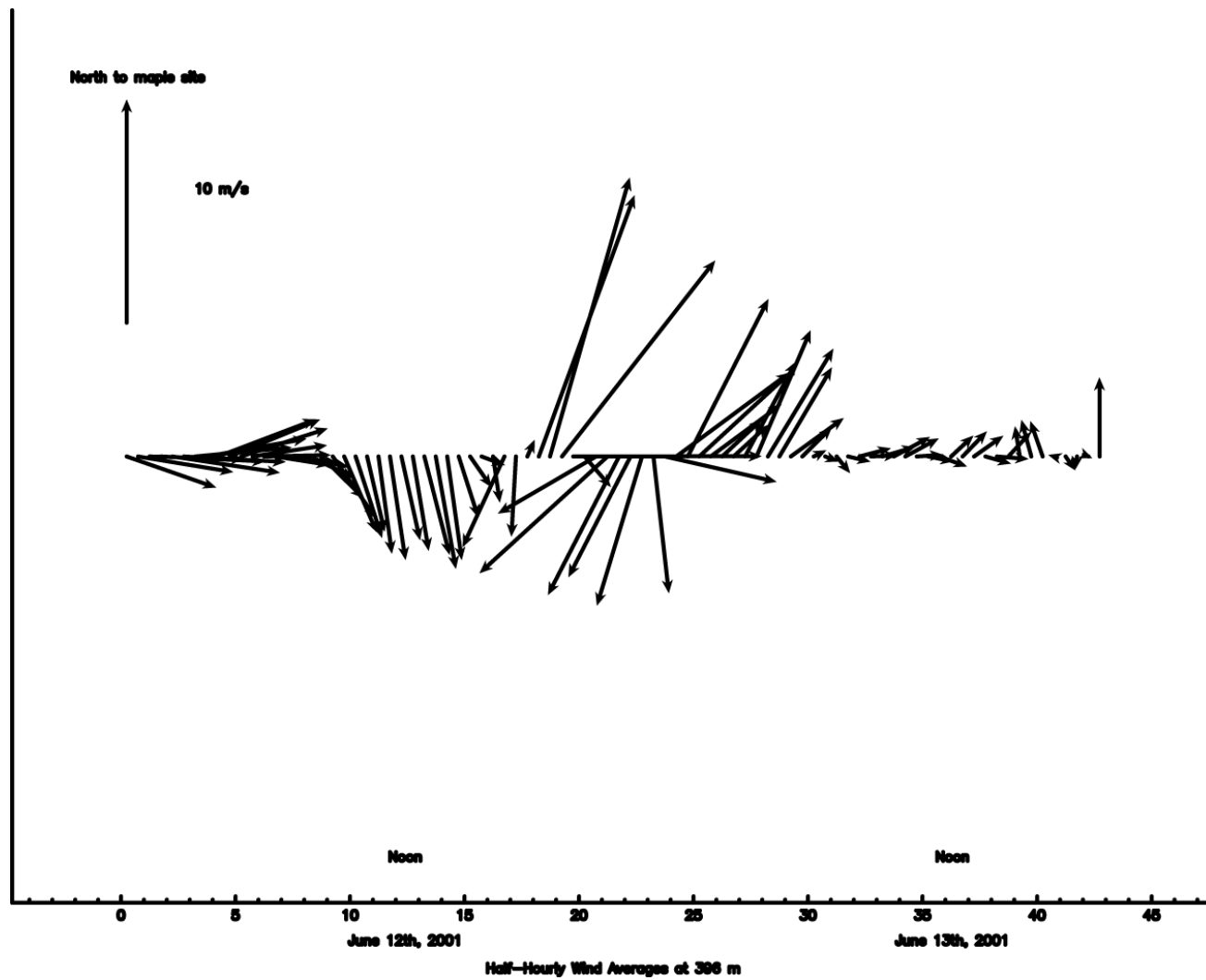


Figure 28. Passage of a synoptic storm over the WLEF area in mid-June, 2001.

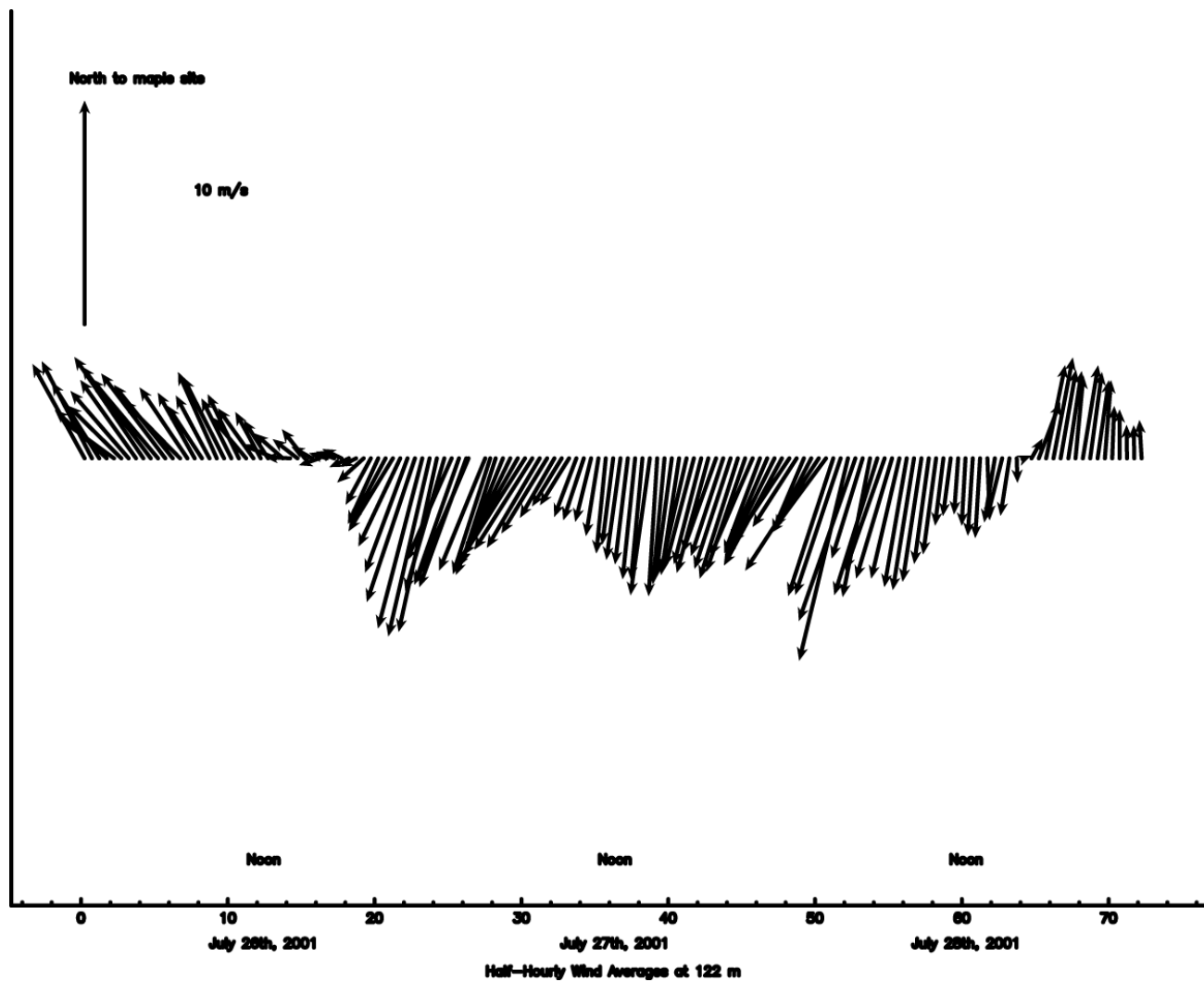


Figure 29. Winds at the WLEF tall tower site during the July, 2001 field campaign.

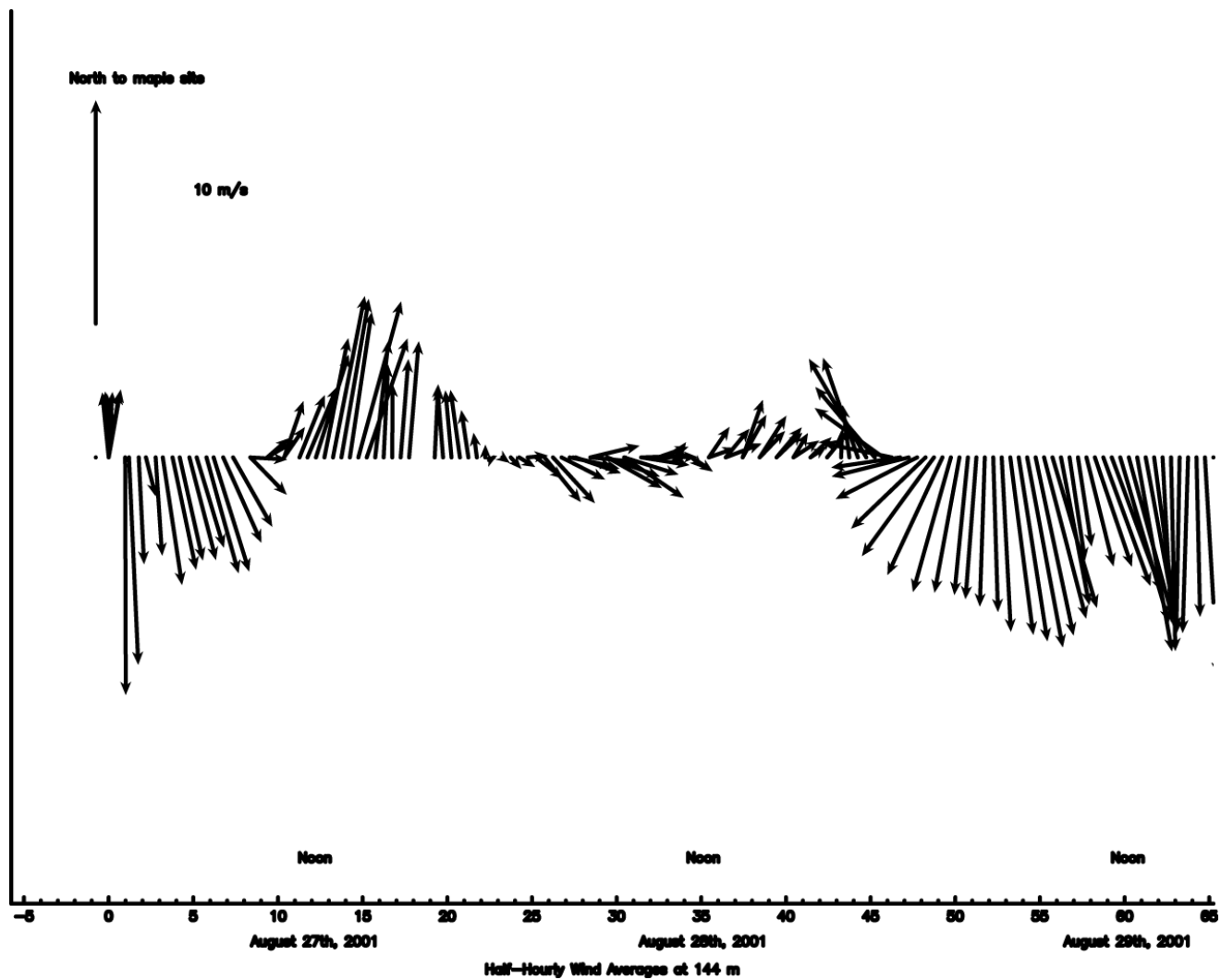


Figure 30. Winds at the WLEF tall tower site during the August, 2001 field campaign.

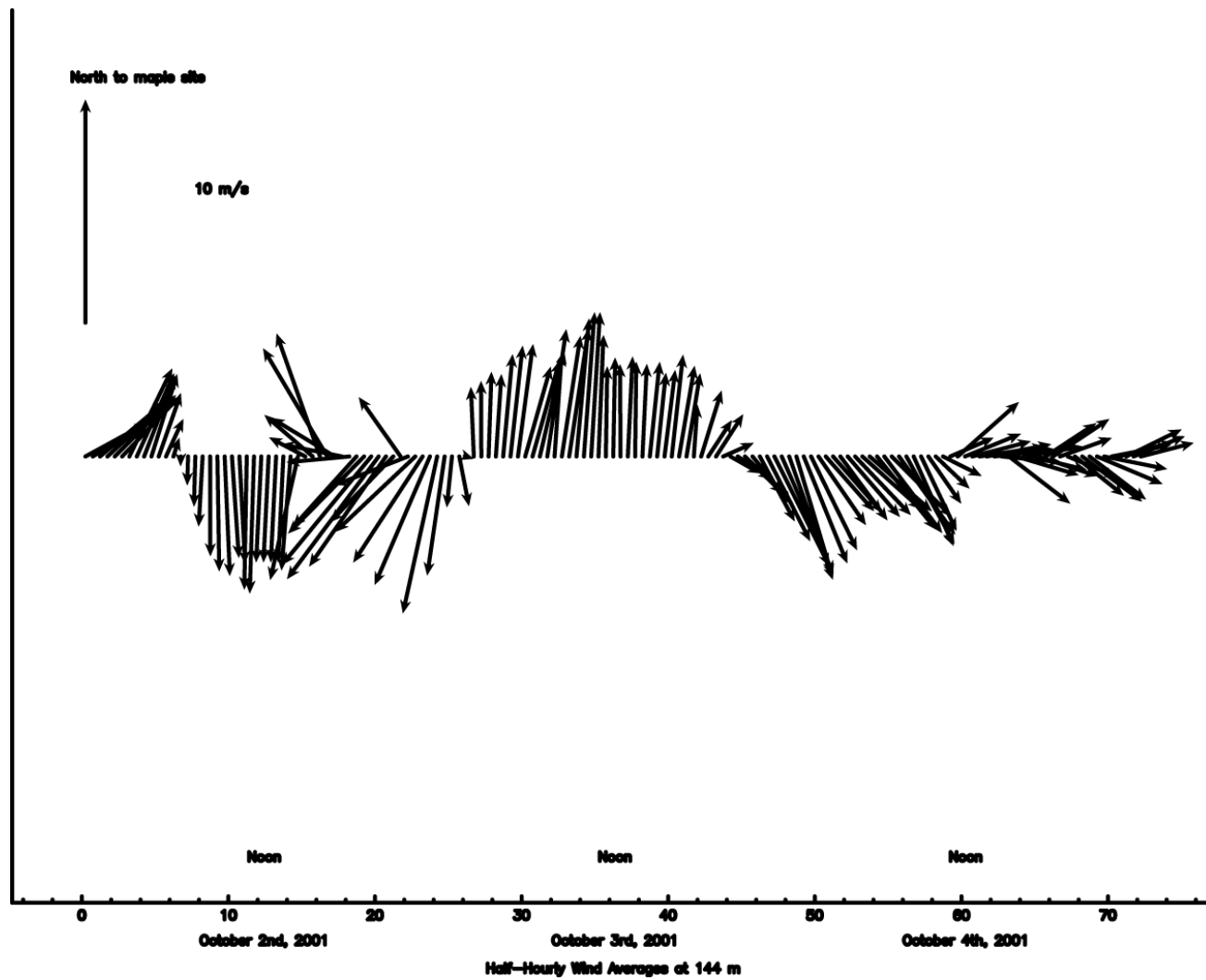


Figure 31. Winds at the WLEF tall tower site during the October, 2001 field campaign.

Measured Ensemble Profiles

Acer platanoides (maple)

June 12th, 2001

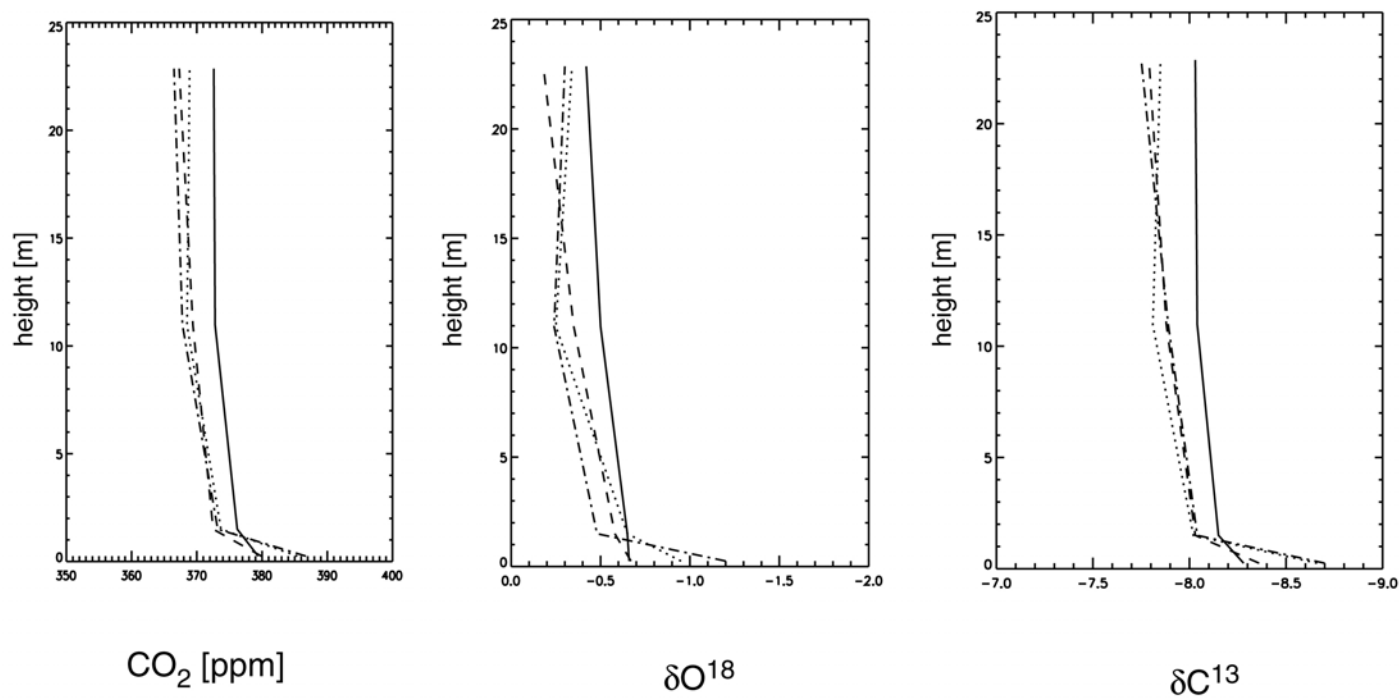


Figure 32. An ensemble view of the June, 2001 canopy profiles.

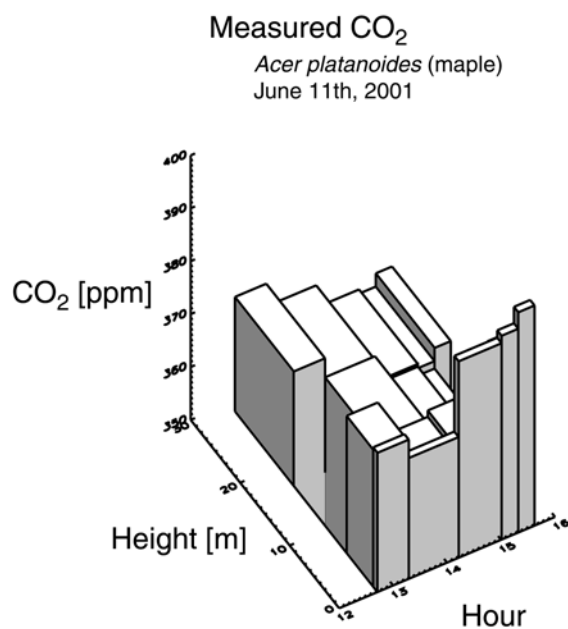


Figure 33 (a). Canopy profiles of CO₂ concentration at a maple stand on the afternoon of June 11th, 2001. The hours of 12 to 16 correspond to a single afternoon. The canopy height is approximately 21 meters.

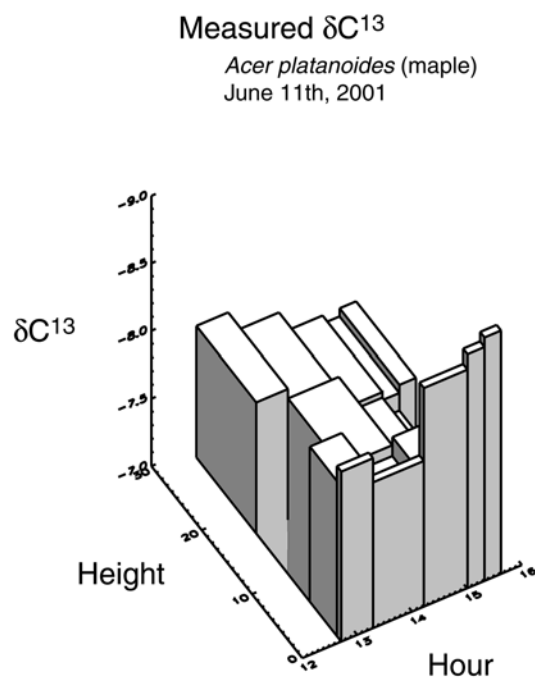


Figure 33 (b). As in (a), for $\delta^{13}\text{C}$ of canopy air CO₂.

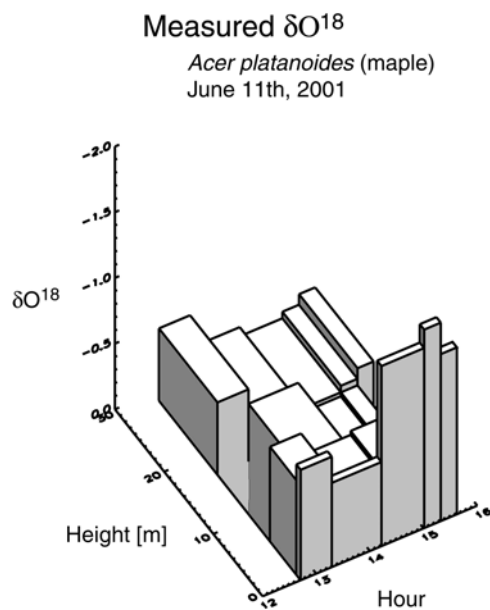


Figure 33 (c). As in (a) and (b), for $\delta^{18}\text{O}$ of canopy air CO_2 .

	Maple/June	Willow Creek/August
Peak visible beam radiation	$\sim 390 \text{ W/m}^2$	$\sim 280 \text{ W/m}^2$
Peak air temperature	$\sim 305 \text{ K}$	$\sim 300 \text{ K}$
Peak canopy temperature	$\sim 303 \text{ K}$	$\sim 301 \text{ K}$
Peak net assimilation	$1.95 \text{ moles/m}^2/\text{sec}$	$1.55 \text{ moles/m}^2/\text{sec}$
Noon vapor pressure in the canopy air space	$\sim 22 \text{ mb}$	$\sim 24 \text{ mb}$
Noon d^{13}C of the canopy air space	$\sim -7.5 \text{ per mille}$	$\sim -7.7 \text{ per mille}$
Noon d^{18}O of the canopy air space	$\sim 0.0 \text{ per mille}$	$\sim 0.5 \text{ per mille}$
Noon rate of ground respiration	$\sim 3.0 \text{ moles/m}^2/\text{sec}$	$\sim 4.1 \text{ moles/m}^2/\text{sec}$
Noon ventilation mass flux	$.09 \text{ kgm}^{-3}(\text{m/s})$	$.09 \text{ kgm}^{-3}(\text{m/s})$

Table BB. Meteorological forcing and canopy response as simulated by SiB2 for similar days in summer, 2001.

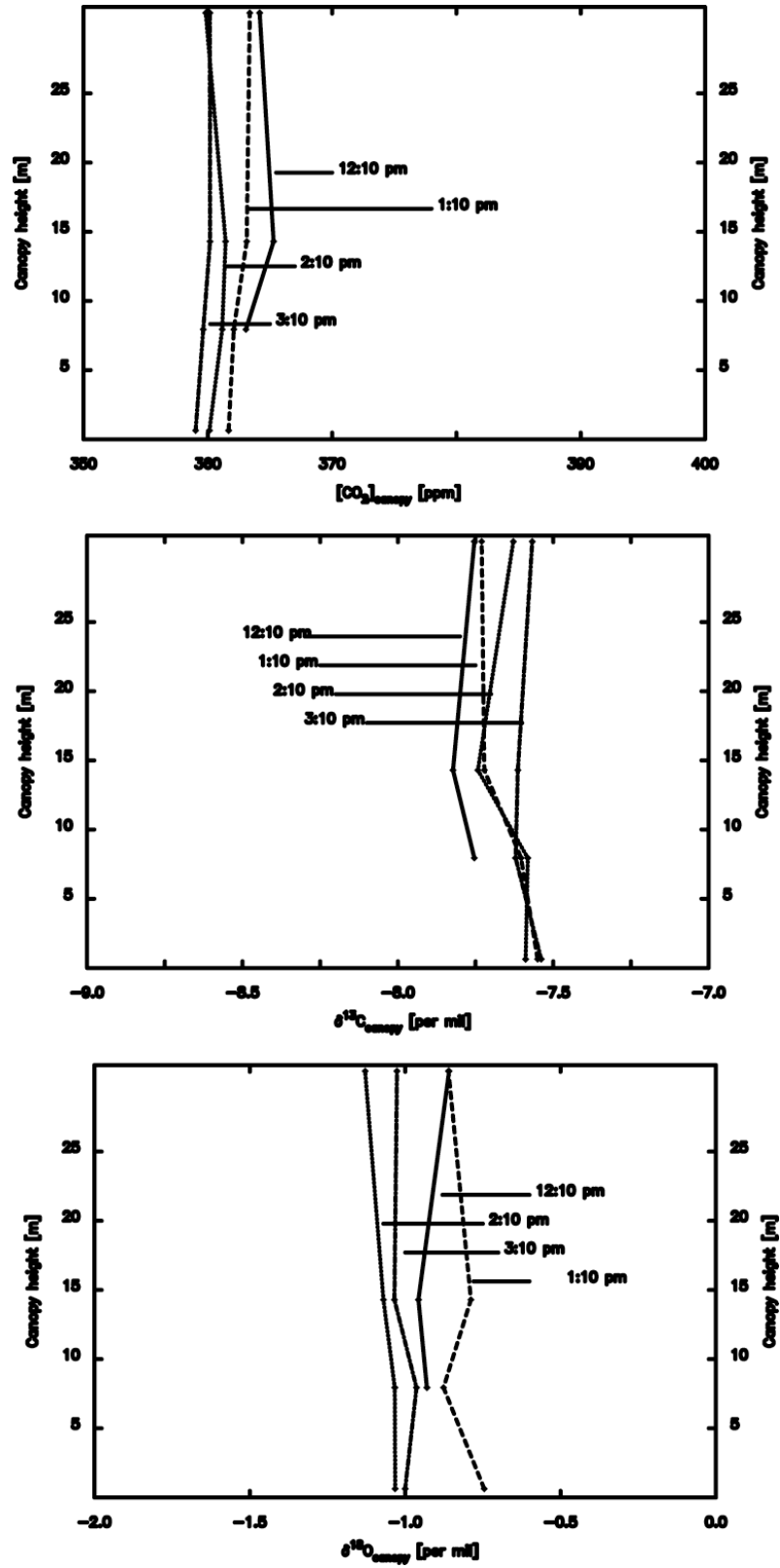


Figure 34. Ensemble profiles of the August, 2001 data at Willow Creek.

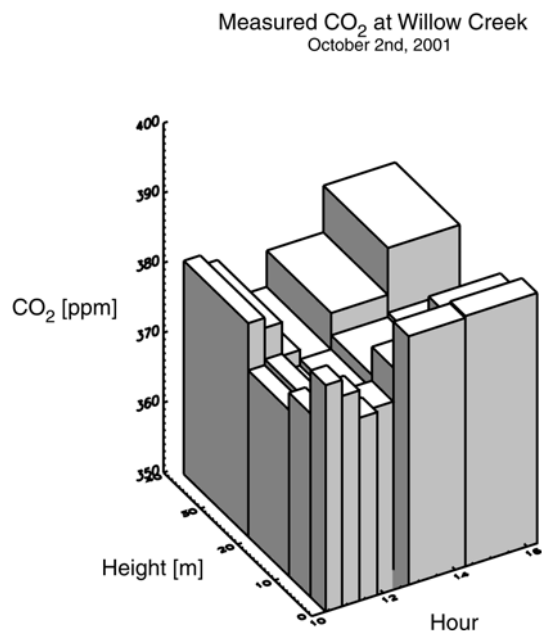


Figure 35 (a). Canopy profiles of CO₂ concentration at Willow Creek on the afternoon of October 2nd, 2001. The hours 10 to 16 pass through noon. The height of the canopy is approximately 24.3 meters.

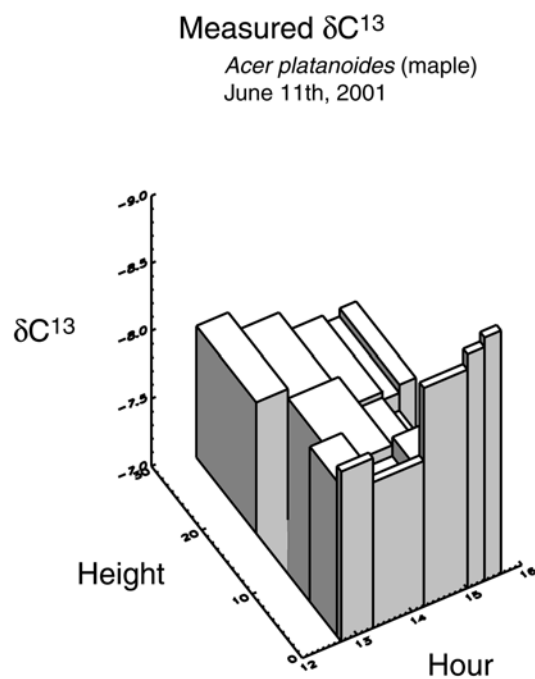


Figure 35 (b). As in (a) for $\delta^{13}\text{C}$ of canopy air.

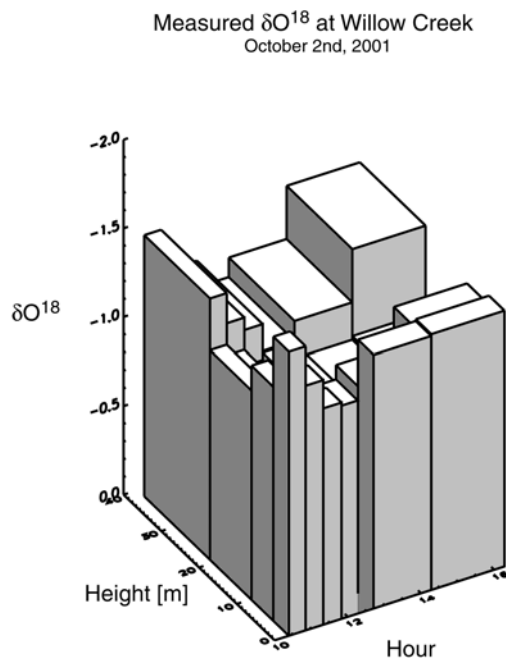


Figure 35 (c). As in (a) and (b) for $\delta^{18}\text{O}$ of canopy air.

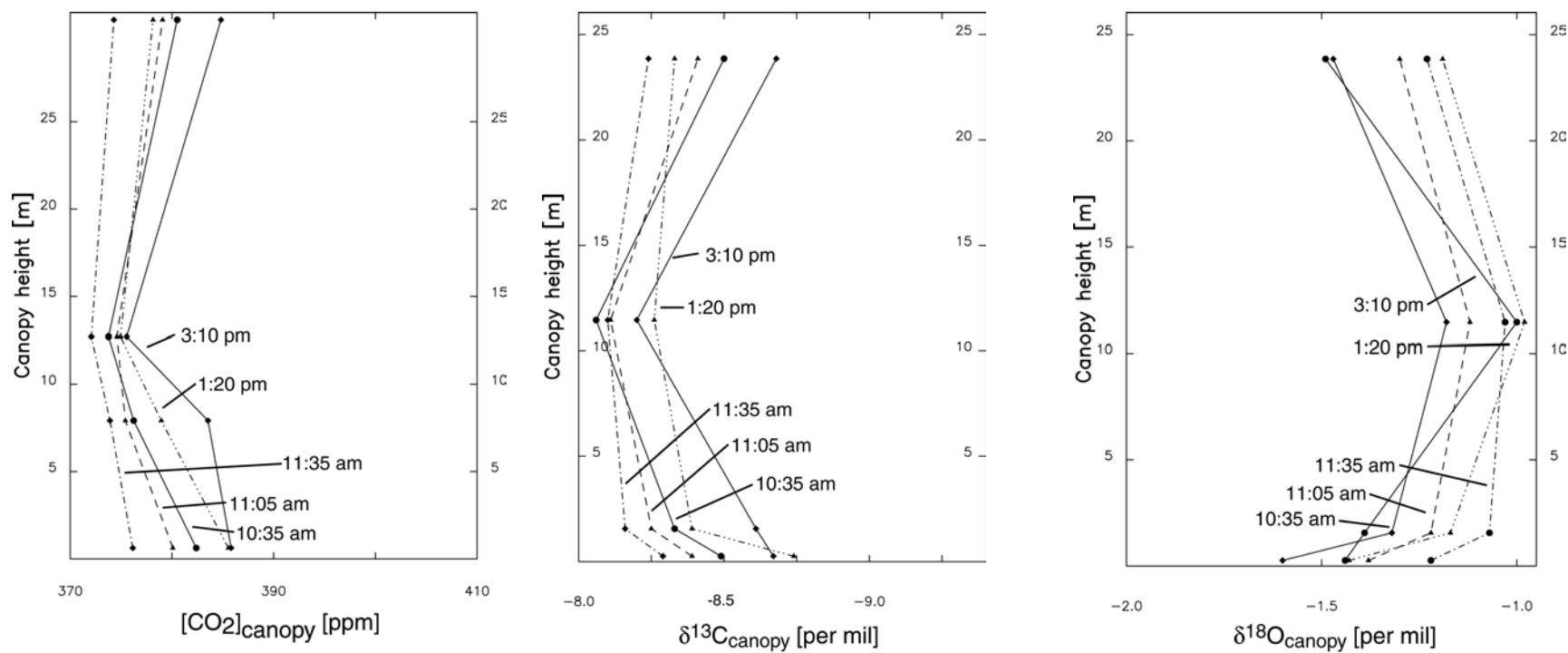


Figure 36. Ensemble profiles of the October, 2001 data at Willow Creek.

Previous studies indicated that open stands with more vigorous understory experienced more photosynthetic drawdown and enrichment and weaker gradients (Buchmann et al., 1997a); in contrast, this study found that stronger gradients at the maple site also correspond to greater drawdown and enrichment.

The maple site notwithstanding, results at the Willow Creek site revealed weak gradients on days of strong photosynthetic exchange and strong gradients on days of weak photosynthetic exchange. Results for October, 2001 show stronger gradients and significant photosynthetic gradient reversals despite the onset of senescence (Figures 35 and 36). The stronger gradients correspond to a period of static stability in the interval between rain events at Willow Creek. In August, I found a correlation of entrainment into the PBL with intense photosynthesis, via the rectifier driver. In October, I found the reverse in the form of increased storage gradients and decreased ecosystem exchange during a period of senescence. The two different results (gradients and evidence of exchange drawdown positively correlated across two sites and negatively correlated at the same site) suggest that the effects of storage vary systematically between Willow Creek and the maple site.

[Read up on Buchmann's article.] Rather than simply control for atmospheric stability, as did Buchmann et al. (1997a), one must consider the correlation through the rectifier driver, as well as the feedback effects of vapor pressure deficit. One must control for physiological forcing before drawing conclusions regarding canopy structure from a comparison of two sites.

Canopy layers show temporal “decoupling” in the vertical structure of CO₂ species (Table AA). One possible explanation for these effects is three-dimensional advection; another is the passage of pressure perturbations, for example as lines of convergence and divergence in the convective PBL. Horizontal heterogeneity in the canopy structure could easily lead to these effects. Any one of these physical effects may cause the CO₂ profile to “wobble” back and forth as it is sampled. An alternative explanation is that the

12:55 pm	1:40 pm	2:15 pm	2:45 pm	[CO ₂]
372.6	368.9	367.3	366.5	Z = 23 m
372.8	368.5	369.4	367.8	Z = 11 m
376.2	373.7	372.5	373.2	Z = 1.5 m
379.4	385.4	379.9	386.7	Z=0.25 m

Table AA (a). Temporal trends in the structure of [CO₂] on the afternoon of June 12th, 2001 at the maple stand. The canopy is about 20 m tall. Arrows point in the direction of increasing CO₂ concentration, showing two- and three-layer structure.

12:55 pm	1:40 pm	2:15 pm	2:45 pm	$\delta^{18}\text{O}$
-0.42	-0.34	-0.18	-0.3	Z = 23 m
-0.5	-0.25	-0.35	-0.24	Z = 11 m
-0.65	-0.65	-0.58	-0.48	Z = 1.5 m
-0.66	-0.95	-0.67	-1.2	Z=0.25 m

Table AA (b). Temporal trends in $\delta^{18}\text{O}$ of canopy air CO₂. Arrows point in the direction of enrichment. As in Table AA (a).

stochastic sampling error discussed in the Background section has caused the appearance of decoupling.

6.3 Model-Data Comparisons

The modeled stationary profiles compare well with those time-dependent measured profiles that are poorly mixed (Figure 37). Here, the registration of model and data is due entirely to the measured boundary condition, while the internal gradients, which agree less well, are driven by sources and sinks. Only those profiles that are poorly mixed compare well with the model; those measured profiles that are completely scoured to the soil surface, and of vanishing amplitude, are not represented by the model. Why did the model represent only those profiles with near-soil storage?

One possible nonphysical reason is that the absence of a pressure gradient leaves the model too well stratified. If this is the case, our physical explanations are moot. The dynamical evidence presented in Chapter 5 suggests that the canopy layer experiences several regimes which change with height. The existence of a pressure gradient in the lower canopy would tend to cause flux divergence in the Reynolds stress and in other second moments as well, causing the dynamical model to be less stratified. Can I still conclude that the canopy flow is regime driven? Yes, Raupach's family portraits strongly suggest that it is. Can I still conclude that length scales are coherent and regime driven? Yes. The importance of the vorticity thickness $U/du/dz$ is not to be denied.

Despite the known weakness in the model, an enticing physical possibility exists that the modeled governing length scales λ_i should be determined by a regime qualitatively different than the von Karman surface layer. In this version of the model, the length scale vanishes at the soil surface where the modeled flow becomes more "viscous" (see Figure 24). In both real canopies and in the model, the length scale governing mixing is greater than the scale of the tracer gradient, and non-local transport occurs near the soil surface. In fact, the most energetic eddies are of the scale of the canopy height and are thought to scour the lower canopy intermittently. There is no reason to believe that the length scales governing a coherent flow should diminish there. A priori, the modeled length scale only vanishes near the soil surface because the canopy is thought to be a perturbed surface layer, with perturbed von Karman scaling.

If the layer is regime-driven, then an entirely different length scale relation is called for, one which relates the vorticity thickness $U/(dU/dz)$ to the properties of the canopy. In practice, early experiments with this model length scale did not lead to plausible results, and the development of new length scales is an area of future work. I can only approximate the average effects of intermittent coherent motions by making the flow less “viscous.” A better solution is the development of a prognostic dissipation equation for canopies.

Measured profiles displayed an intermittency on time scales of ~ 20 minutes that was not captured by the model. The road to intermittency is of course the development of a prognostic model. In order to understand recycling, flow over topography, and three dimensional advection in canopies, one must consider time dependence. The issue of recycling in particular requires an understanding of vertical communication in tracer transport. The irony here is that while the model appears to be too well stratified, vertical communication is mathematically “perfect.” Let me show you.

Consider the fluxes of two tracers, one that is released from the soil surface and another that is released in equal amounts just below the top of the model domain. The red tracer is upwelling and the blue tracer is downwelling. Decomposing each into an average and a perturbation yields:

$$\begin{aligned} r &= \langle \bar{r} \rangle + r' & b &= \langle \bar{b} \rangle + b' \\ f_r &= \langle \overline{w'r'} \rangle & f_b &= \langle \overline{w'b'} \rangle \end{aligned} \tag{177}$$

where r is the red tracer, b is the blue tracer, and the dispersive fluxes are ignored. The absolute efficiency of mixing can be represented as:

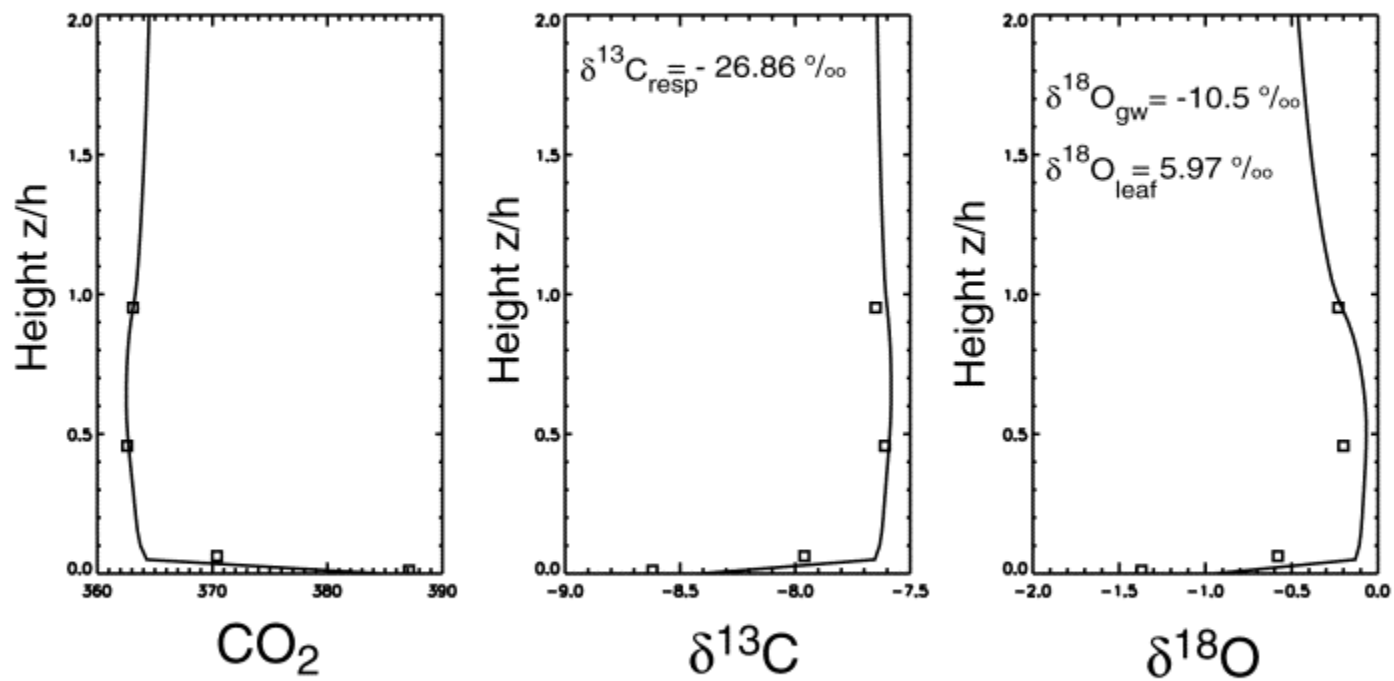


Figure 37. A direct model-data comparison during the month of June, 2001.

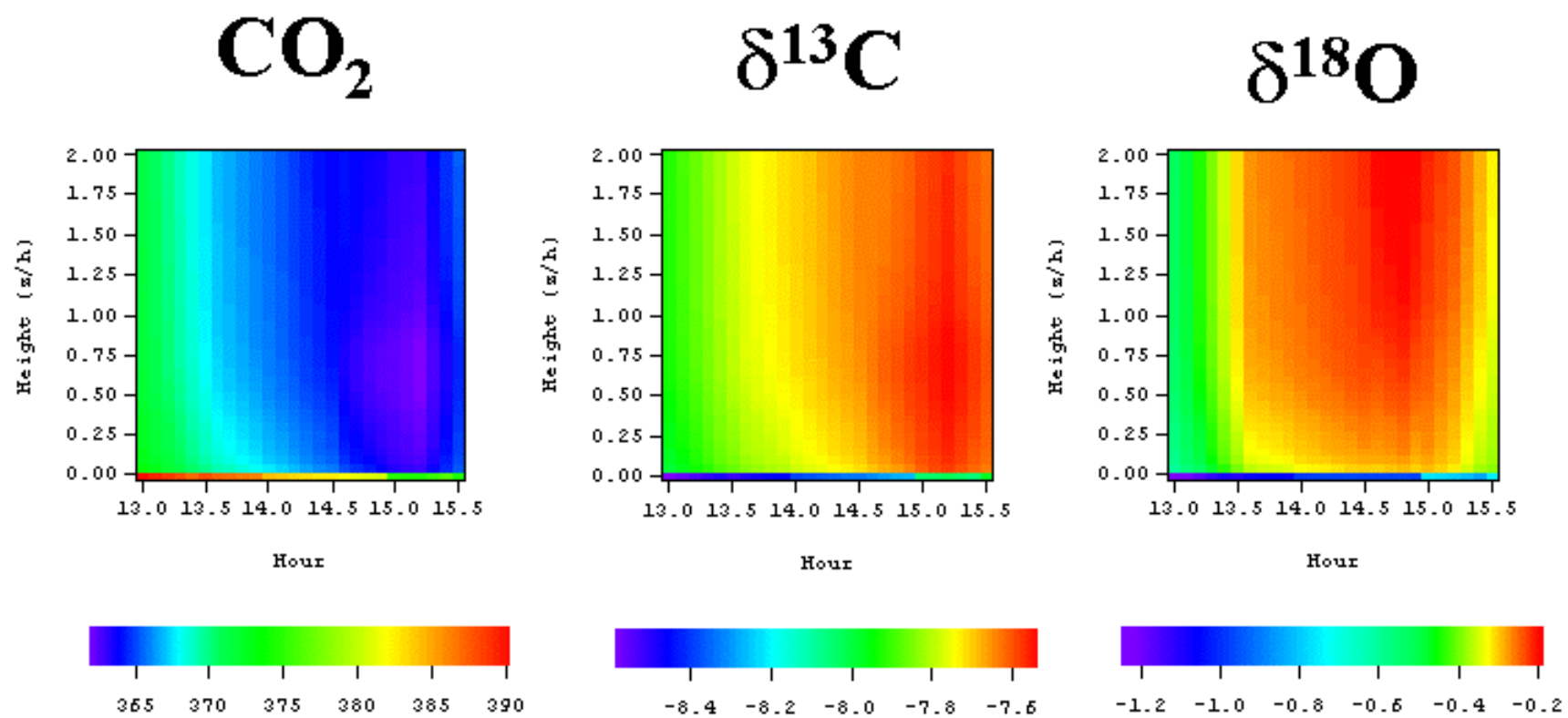


Figure 38. Continuously driven simulations of afternoon drawdown and enrichment at Willow Creek in June of 2001.

$$\frac{\langle \overline{r'b'} \rangle}{\sqrt{\langle \overline{r'^2} \rangle} \sqrt{\langle \overline{b'^2} \rangle}} \quad (178)$$

In practice, the measurement of this mixing efficiency is hard to control. If an equal amount of the blue tracer is released just below the top of the canopy, some blue dye will diffuse upward and the experiment will not be adequately controlled. Such an experiment is difficult to implement numerically. A more pragmatic measure of vertical communication is the symmetry of mixing:

$$\frac{\langle \overline{f_b' f_r'} \rangle}{\sqrt{\langle \overline{f_b'^2} \rangle} \sqrt{\langle \overline{f_r'^2} \rangle}} \quad (179)$$

A value of 0 reflects complete insulation, while a value of -1 reflects perfect communication. The model weakness that is exposed here is that in a steady state, this ratio is always -1 . This precludes the discovery of any natural bias in information contained in real flux footprints due to inefficiencies in vertical mixing. The implications of this are immediately obvious in a suite of continuous modeled profiles shown in Figure 39. Unlike the measured time series shown in Table AA, the modeled time series show a lockstep depletion in CO_2 and enrichment in $\delta^{13}\text{C}$ and $\delta^{18}\text{O}$ during the afternoon.

6.4 Spatial and Temporal Ecosystem Comparisons

Ecosystem inferences into the scale-dependent age of respiring carbon and seasonal trends in ecosystem discrimination arise from the physiological boundary constraints. These inferences in turn inform the forward model. In these data, telling spatial-temporal patterns are at work. Seasonal comparisons of nighttime Keeling plots from the *Acer platanoides* site (June) and Willow Creek (August and October) are shown in Figure 39. The Keeling plot intercepts in $\delta^{13}\text{C}$ are -26.70 per mille (June), -26.86 per mille (August), and -25.91 per mille (October). The August and October intercepts are

significantly different ($t = 2.13$, $t_{\text{crit}} = 1.96$, using a common regression). The supposed decrease in ecosystem discrimination from August to October is inconsistent with the decrease in temperature and vapor pressure deficit and the decrease in stomatal limitation. Both stomatal limitation and photosynthetic capacity independently influence C_i/C_a : here, photosynthetic capacity has decreased from August to October, increasing C_i/C_a and increasing discrimination. However, the increased ecosystem discrimination is not reflected in the heavier October source. Instead, the enrichment in $\delta^{13}\text{C}$ from August to October is a comparison in temperature and scale. High soil temperatures should make the respiratory source heavier (older), while the effects of senescence should scale respiration from the ecosystem to the soil and make the source heavier (older) as well.

The contrast in the $\delta^{18}\text{O}$ source between June (maple), August (Willow Creek), and October (Willow Creek) is more ambiguous. Rather than directly infer ecosystem discrimination from $\delta^{18}\text{O}$ signals, we consider the resetting of soil water by meteoric input, the variation in the meteoric source over time, and temperature dependent evaporative enrichment of the soil and leaf sources. The $\delta^{18}\text{O}$ nighttime sources were -14.63 per mille in June, -11.09 per mille in August, and -14.36 per mille in October, respectively. The contrast between August and October was obviously significant ($t=19.0$, $t_{\text{crit}}=1.96$, using a common regression). The depletion of the $\delta^{18}\text{O}$ source from August to October is consistent with temperature-dependent evaporative enrichment.

Daytime regressions of $\delta^{13}\text{C}$ and $\delta^{18}\text{O}$ at four different heights in the canopy were also conducted as an exercise in up-scaling canopy footprints of photosynthesis and respiration. In general, daytime regressions of $\delta^{13}\text{C}$ against $[\text{CO}_2]$ are linear and are considered valid Keeling plots, while daytime regressions of $\delta^{18}\text{O}$ against $[\text{CO}_2]$ are often considered questionable. Daytime Keeling plot intercepts showed no statistically significant variation with height: with only a few data points, the standard deviations of each intercept were too large to allow for meaningful comparisons. One might expect, for example, that the respiratory source become younger and lighter as one moves up a hierarchy of footprints from the soil to the entire ecosystem. No such trend was found.

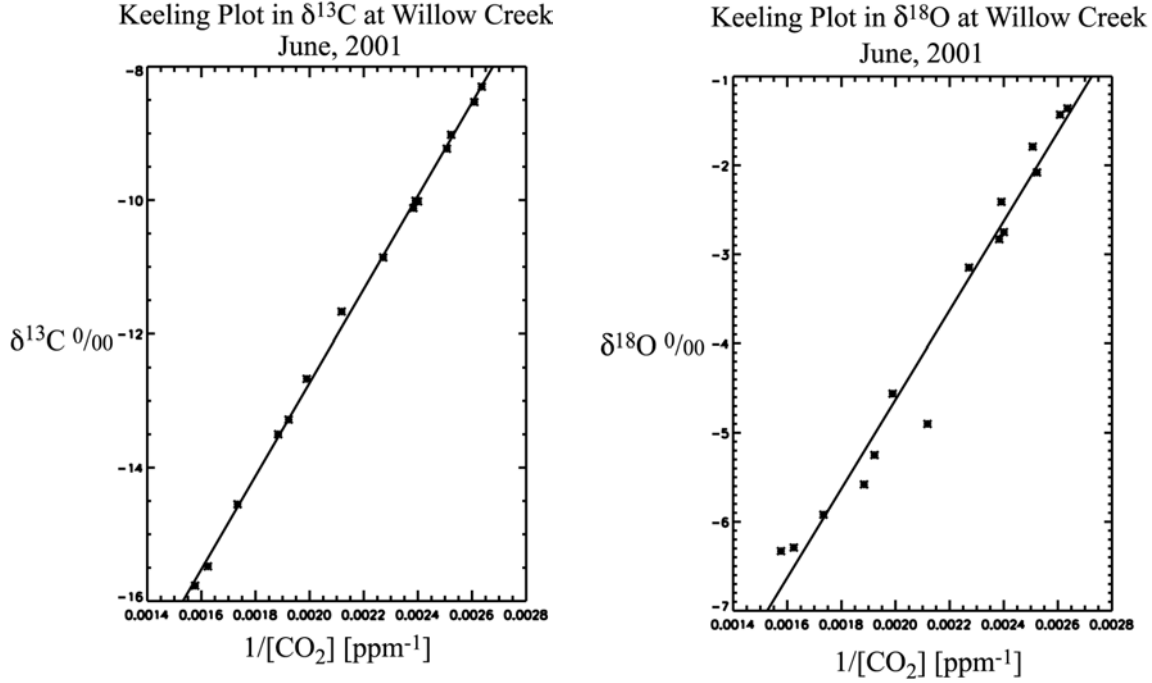


Figure 39 (a) Nighttime Keeling plots of $\delta^{13}\text{C}$ and $\delta^{18}\text{O}$ vs. $1/[\text{CO}_2]$ for June, 2001. The regression model allowed for error in both X and Y. Errors in both variables were increased by constant factors until the confidence of the Keeling plot fell within acceptable bounds. For $\delta^{13}\text{C}$: intercept -26.70 ± 0.31 , slope $6986. \pm 141.$, $r^2 > 0.99$. For $\delta^{18}\text{O}$: intercept -14.63 ± 0.8 , slope $5001. \pm 362.$, $r^2 = 0.97$.

Comparisons between daytime and nighttime Keeling plot intercepts in $\delta^{13}\text{C}$ potentially offer information on isotopic disequilibrium. The term

$$\frac{[\text{CO}_2]_p}{[\text{CO}_2]_f} (\delta_r - \delta_p) \quad (176)$$

in Equation (162) depends directly on disequilibrium, where p refers to the photosynthetic drawdown, f refers to the composition of forest air, and r refers to the composition of respired air. In practice, the photosynthetic drawdown $-\text{[CO}_2\text{]}_p$ is only a few ppm in the canopy, and the term above is ~ 2 orders of magnitude smaller than its neighbors in Equation (162). At the Willow Creek site in August, the daytime Keeling plot intercept in $\delta^{13}\text{C}$ was not significantly different from the nighttime intercept within the standard error of each elevation. Therefore, the photosynthetic term in daytime

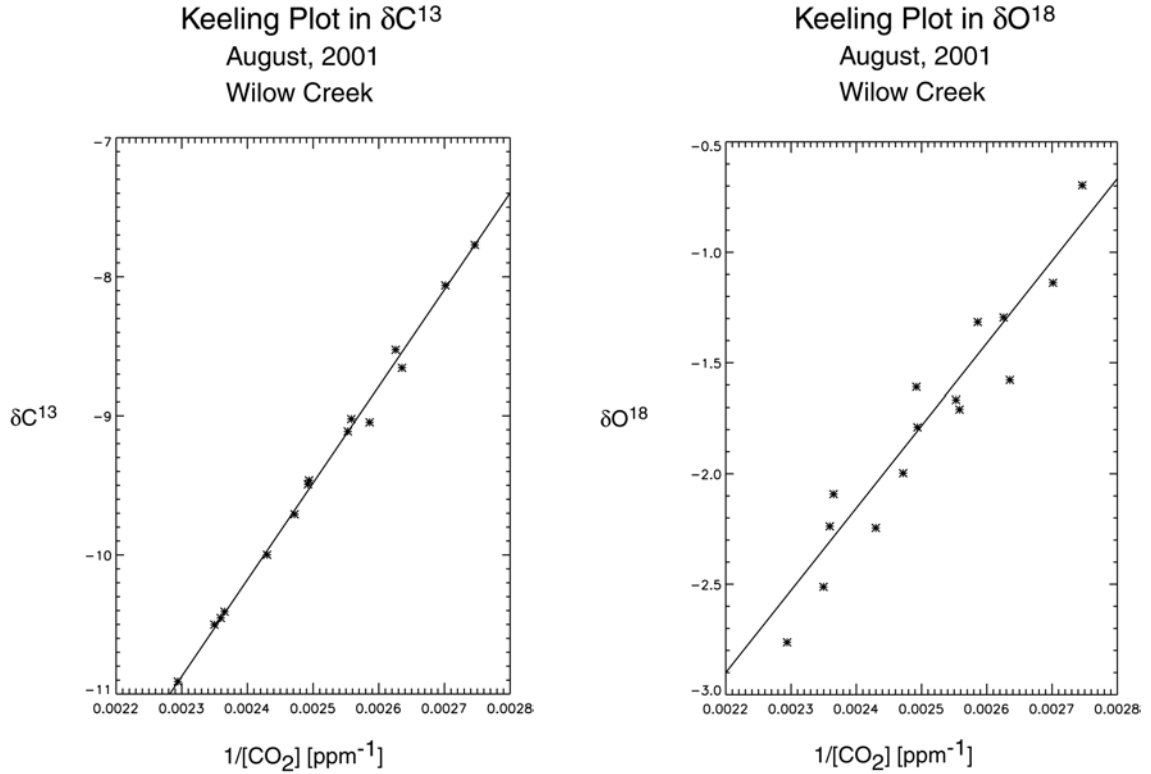


Figure 39 (b) Nighttime Keeling plots of $\delta^{13}\text{C}$ and $\delta^{18}\text{O}$ vs. $1/[\text{CO}_2]$ for August, 2001. The regression model allowed for error in both X and Y. Errors in both variables were increased by constant factors until the confidence of the Keeling plot fell within acceptable bounds. For $\delta^{13}\text{C}$: intercept -26.83 ± 0.56 , slope $6942. \pm 228.$, $r^2 > 0.99$. For $\delta^{18}\text{O}$: intercept -11.09 ± 1.6 , slope $3723. \pm 650.$, $r^2 = 0.91$.

Keeling plots may be neglected, and daytime Keeling plot intercepts may be taken as a direct indication of the composition of the respiratory source.

6.5 Source Water Composition

At the leaf level, $\text{H}_2^{18}\text{O}^{16}\text{O}$ both evaporates and diffuses more rapidly than $\text{H}_2^{16}\text{O}^{16}\text{O}$, leaving water vapor depleted and the evaporative surface enriched with respect to whole leaf water. At Willow Creek in the month of July, afternoon leaf water was indeed enriched by 13.5 per mille with respect to soil water at 5 cm depth. Pre-dawn sampling at the maple site in June revealed a source of -8.7 per mille in the ^{18}O of stem water, which is thought to equilibrate with soil water. Complete equilibration of leaves with respect to

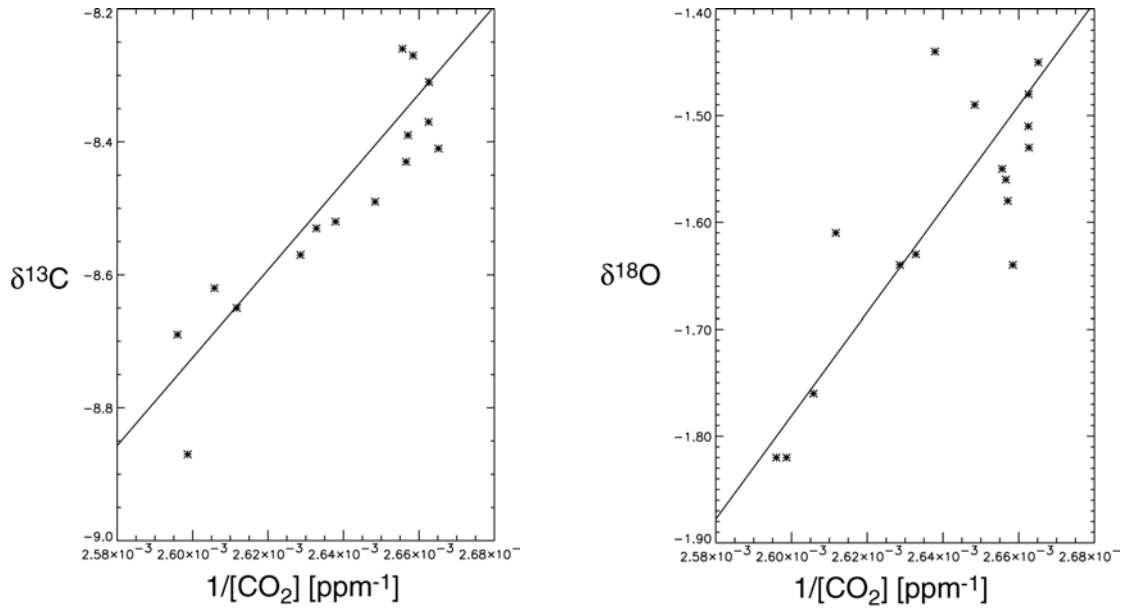


Figure 39 (c) Nighttime Keeling plots of $\delta^{13}\text{C}$ and $\delta^{18}\text{O}$ vs. $1/[\text{CO}_2]$ for October, 2001. The regression model allowed for error in both X and Y. Errors in both variables were increased by constant factors until the confidence of the Keeling plot fell within acceptable bounds. For $\delta^{13}\text{C}$: intercept -25.88 ± 3.5 , slope $6599. \pm 1324.$, $r^2 > 0.84$. For $\delta^{18}\text{O}$: intercept -14.36 ± 3.6 , slope $4830. \pm 1371.$, $r^2 = 0.68$.

source water is normally assumed overnight, yet pre-dawn sampling yielded whole leaf water values that were enriched (average -5.8 ± 0.7 per mille) with respect to stem water. The favored cause for this enrichment is evaporation and not a physiological or external change in the soil water source. Another surprise came with the contrast in stem water composition between pre-dawn and afternoon samples on the same day in June (pre-dawn stem water: -8.7 ± 0.7 per mille; early afternoon stem water: -10.5 ± 0.3 per mille). The composition of stem water *should* not change over the course of a day. Unless one is extremely unlucky, differences in sampling do not explain this apparent change in stem water composition.

One possible cause for the unexpected differences in source water composition are lag times in the equilibration of water with its source. Equilibration between leaf and stem water should occur quickly, while slow changes in the composition of the groundwater source would be followed by slow whole-plant equilibration. In the absence of evaporation, the time to equilibration of the whole plant would depend linearly upon

volume and exponentially upon the rate of renewal. While we can easily estimate the volume, the nighttime rate of exchange is a major source of uncertainty that needs to be constrained.

6

Conclusion

This thesis began with global motivations and local intentions, in both time and space. What have I learned about mechanisms of isotopic exchange at small scales and how they inform signals at larger scales? The greatest lesson of this study is that the same correlation between ecosystem exchange and vertical mixing that drives the global rectifier beats at the canopy scale. I found strong gradients on days of weak ecosystem exchange and vice versa. The stronger this correlation, the weaker the potential for recycling of respired CO₂. If this relationship between PBL bottom entrainment and ecosystem exchange can be parameterized and extended to the early morning hours, an estimate of recycling would result, with global ramifications. In order to understand this result, only thermodynamically active models can tell us whether canopy mixing is driven by vertically distributing canopy heat sources or convective PBL entrainment. Is the mechanism of coupling to the PBL, rather than the mechanism of mixing within the canopy, most important to understanding recycling? An adaptation of a “jump” model for PBL bottom entrainment, or a coupled mass budget of the canopy and the PBL, would be a useful tool in understanding recycling.

In the stable isotope case study, the tracer transport model was largely transparent to eco-physiology. In the forward sense, the structure and amplitude of canopy signals were robust and depended more upon the presence of vertical physiological structure in the source distribution than upon the order of turbulence closure *per se*. A simple disaggregation of bulk physics and physiology adequately predicted the structure and

amplitude of canopy profiles. The tracer transport model would be well represented by two reservoirs. One, a shallow resistive reservoir near the soil surface, would mix with another, deeper, well-mixed reservoir aloft in the canopy. A simple closure in eddy diffusivity is still elusive near the soil surface, where community knowledge of turbulent dynamics is ambiguous.

The importance of meteorological and ecological contexts was an unexpected byproduct of this research. Temporal and spatial comparisons of the ecological boundary measurements reveal that the respiratory source in ^{13}C was isotopically heavier in October than in August, reflecting a carbon source that is older, less labile, and partially scaled from the ecosystem to the soil. This result is consistent with warmer soil temperatures in fall and inconsistent with the assumption that respired carbon is labile, recently fixed and immediately reflective of discrimination. It contradicts the finding of Flanagan et al. (1996) that respiratory composition in an aspen grove was lighter in ^{13}C in the fall than in the summer, due to decreasing photosynthetic capacity. These results also call into question our conceptual model of nighttime equilibration of groundwater, soil, stem, and leaf water.

Meteorological context was equally important. I discovered that the rectified signal of the PBL was an important context in which canopy profiles are imbedded. While internal canopy gradients are driven by source distributions, these gradients are small. The larger drawdown and enrichment of simulated profiles was driven not by flux convergence in the distribution of the sink but by the bulk properties of the canopy and the amplification of signals by the beating of the PBL. Meteorology is important to the information content of canopy signals. Under well-mixed conditions, parcels of air take a forgetful random walk through the canopy, sampling bulk properties along the way. Thus inversions that “drill down” under well mixed conditions will sample bulk physiology and net ecosystem exchange, while inversions that “drill down” under stratified conditions will sample local physiology and gross photosynthetic and respiratory exchange. When weighted by ecosystem exchange, temporally averaged

inversions will generally sample bulk properties. When put this way, one might as well invert using bulk physiological models, since one will gain similar knowledge either way.

In the dynamical case study, two canopy regimes emerged. In the lower canopy, a low-energy regime of little flux divergence arose, while the upper canopy regime was more energetic and divergent. The presence of a pressure gradient force would result in more flux divergence both in the lower canopy and above the canopy and therefore more turbulent transport. These regimes suggest simplifications to a full physics model which may be applied to future versions of SiB. The Walker Branch case demonstrated the relationship between greater eddy viscosity and smaller turbulent length scales. This suggests a dynamical modification to the model, such as a prognostic dissipation equation in place of a prescribed length scale. The steady state model did not capture the intermittency of the Walker Branch data, particularly the reported intermittency of the turbulent intensity $\langle u'^2 \rangle / U$. Certain contrasts between second moment profiles at Walker Branch suggested that perhaps the isotropy of dissipation in the model was unrealistic. Lastly, the presence of skewness in horizontal velocity at Walker Branch indicated the presence of horizontal heterogeneity, which is not captured by the one-dimensional model.

The goals of this thesis were threefold: first, to gain insight into the future treatment of canopy aerodynamics in SiB; second, to test our bulk physiological assumptions of light absorption and isotope discrimination; and third, to test the dynamical model using stable isotopes. In the next generation of SiB, tracer transport will be represented by a simple two-box mixing model in which a smaller reservoir of resistant air near the soil surface mixes with a deeper, well-mixed box aloft. The generalized representation of thermodynamically stable and unstable conditions will carry greater weight. Simplifications to the terms in the dynamical equations are indicated if a generalized, physical model of canopy turbulence reproduces the two canopy regimes of high and low energy observed above. Although our bulk physiological assumptions were not truly tested by forward modeling, they will be truly tested by the inversions of tracer transport that are yet to come. The last goal, that of

testing the tracer transport model using stable isotopes, revealed that while the model has dynamical weaknesses, the dynamical model is also transparent to eco-physiology.

Future work entails the development of a prognostic, vertically staggered, and truly physical dynamical model with a mean pressure gradient, a Coriolis force, and a mean vertical velocity. With a prognostic model, questions of recycling, PBL entrainment, topographically altered flow, three-dimensional advection, and coupled mass budgets between the canopy and the PBL will be investigated. Alternative length scales that relate to the bulk properties and regime-like behavior of canopy dynamics will be investigated. A thermodynamically general model will be used as a testbed for the development of a two-layer scalar exchange scheme, using local gradients to determine soil fluxes. Coupling to Lagrangian models of tracer transport and dynamical models of the PBL is another future direction for the model. The Eulerian model will become a transparent tool for the investigation of ecophysiology within a hierarchy of scales. Finally, analytical inversions of tracer transport will truly test our bulk physiological assumptions and unify the motivations of this thesis.